

Stony Brook University



OFFICIAL COPY

The official electronic file of this thesis or dissertation is maintained by the University Libraries on behalf of The Graduate School at Stony Brook University.

© All Rights Reserved by Author.

Adiabatic Rapid Passage Sequences on Optically Pumped He-Atoms

A Thesis Presented

by

Benedikt Johannes Scharfenberger

to

The Graduate School

in Partial Fulfillment of the Requirements

for the Degree of

Master of Arts

in

Physics

Stony Brook University

August 2007

Stony Brook University

The Graduate School

Benedikt Johannes Scharfenberger

We, the Thesis committee for the above candidate for the Master of Arts degree, hereby recommend acceptance of the Thesis.

Harold J. Metcalf, Thesis Advisor

Professor, Department of Physics and Astronomy, Stony Brook University

Dominik Schneble

Professor, Department of Physics and Astronomy, Stony Brook University

Michael Marx

Professor, Department of Physics and Astronomy, Stony Brook University

This Thesis is accepted by the Graduate School.

Lawrence Martin

Dean of the Graduate School

Abstract of the Thesis

Adiabatic Rapid Passage Sequences on Optically Pumped He-Atoms

by

Benedikt Johannes Scharfenberger

Master of Arts

in

Physics

Stony Brook University

2007

In the last years the force related to Adiabatic Rapid Passage has been studied in the optical regime [13]. ARP is a technique that inverts the population of a two-level system by frequency chirped laser light pulses. If this is done repeatedly, a large force on the atoms is enabled, which is much larger than the radiative force.

This thesis is about the manipulation of metastable Helium atoms He^* using the Adiabatic Rapid Passage sequences. Since the theory of ARP is only suitable for two-level atoms, the main task of this work was to prepare the metastable He-atoms in a way, so that they form a two-level system in order

to obtain a bigger optical force. This is done via optical pumping. Therefore a magnetic field has to be produced, which is realized by Helmholtz-coils that have been designed, built and placed inside the vacuum system that is used in the experiment. Another task was to direct the laser light that was destined for Optical Pumping to the interaction region, using different kinds of optics.

The main result of the work is that the force related to ARP sequences could be significantly improved from previous measurements, since the optical pumping process makes the atoms more susceptible to the interaction with the modulated laser light field. Another proof of the correctness of the theory has been done with producing a force map for different chirping parameters. The results confirm the theoretical prediction and it also shows the robustness of the force.

Contents

List of Figures	xii
List of Tables	xiii
1 Introduction	1
1.1 The two-level atom	2
1.1.1 The Schrödinger equation	2
1.1.2 Rabi oscillations between two states	4
1.1.3 Dressed states	6
1.2 The Bloch Sphere	10
1.3 Radiative Force	12
1.4 Doppler-Cooling	16
1.5 Optical Pumping	20
1.6 Dipole Force	23
1.7 Bichromatic Force	26

1.7.1	The π -Pulse Model	27
1.7.2	The doubly dressed atom picture	31
2	The theoretical background of Adiabatic Rapid Passage	36
2.1	ARP - an introduction	37
2.2	The probability for nonadiabatic transition	40
2.3	Periodic ARP on a two level system	45
2.4	The ARP-Force	49
2.5	The influence of spontaneous emission	53
3	The Metastable Helium Apparatus	60
3.1	Metastable Helium	61
3.1.1	The Helium level diagram	61
3.1.2	Production of metastable He	64
3.1.3	The Helium Beamline	70
3.1.4	The MCP/PS Detector	76
3.2	Production of the magnetic field	80
4	Production of the ARP-light	84
4.1	The Diode Laser	85
4.1.1	Laser Frequency Tuning	86
4.1.2	The locking of the laser frequency	88

4.2	Modulators	91
4.2.1	The Phase Modulator	94
4.2.2	The Amplitude Modulator	97
4.2.3	Production of Chirped Pulses	101
4.3	Fabry-Perot spectrometer	104
4.4	Fiber Optic Amplifiers	107
4.5	Interaction Region	112
5	Making and probing chirped pulses	119
5.1	Spectrum of Periodically Modulated Light	119
5.2	The Phase Modulated Spectrum	123
5.2.1	Determination of V_π for the phase modulator	125
5.3	The Amplitude modulated spectrum	126
5.4	Phase and Amplitude Modulated Spectrum	131
6	Measurement of Optical Forces	136
6.1	Experimental Process	136
6.2	The ARP Force	139
6.2.1	Measurements with the laser taken off lock	147
6.3	Force Mapping	152
6.4	Conclusion	157

Bibliography 165

List of Figures

1.1	Energy levels of a two level atom	5
1.2	Energy levels for an atom in an EM-field	8
1.3	Light shifts of two coupled states	10
1.4	Bloch Sphere	12
1.5	Radiative force	14
1.6	Optical Molasses	18
1.7	Optical Pumping	22
1.8	Dipole Force	25
1.9	π -pulse model of the Bichromatic Force	28
1.10	Asymmetric light field for a net Bichromatic Force	30
1.11	Dressed state energy levels in the doubly dressed atom picture	33
2.1	The trajectory of ARP in the dressed atom picture	42
2.2	Adiabatic following of the Bloch Vector during ARP	43
2.3	Contour plot of the numerical values of ρ_{gg} vs. δ_0 and Ω_0	44

2.4	A set of trajectories of the Bloch Vector on the Bloch Sphere	47
2.5	Calculated values of $\vec{R}(nT)$ on the Bloch Sphere	48
2.6	Schematics of alternating-directional chirped pulse trains	51
2.7	Force on rest atoms caused by sinusoidal light pulses (a)	54
2.8	Force on rest atoms caused by sinusoidal light pulses (b)	58
2.9	Comparison of the velocity dependence for various force schemes	59
3.1	Energy level diagram of Helium	62
3.2	Production of He*	65
3.3	Velocity distribution	69
3.4	Vacuum System	72
3.5	MCP/PS assembly	78
3.6	Frontview of the Helmholtz-coils	81
3.7	Sideview of the Helmholtz-coils	82
3.8	The slit for the geometrical definition of the atomic beam	83
4.1	Extended cavity	87
4.2	Saturated Absorption Spectroscopy	90
4.3	Principle of an electro optical modulator	93
4.4	Phase modulator	96
4.5	Amplitude modulator	98

4.6	Operating points of the amplitude modulator	100
4.7	Periodic optical pulse of the AM and complement of the RF rive signal	103
4.8	RF-signal supply of the modulators	105
4.9	Fabry Perot spectrometer	106
4.10	Optical system for chirped pulse production	115
4.11	Optical setup	116
4.12	OP-beam production	117
4.13	Interaction region	118
5.1	The Bessel functions J_0, J_1, J_2, J_3 as functions of β [13].	124
5.2	Calibration curves of the modulation index β	127
5.3	The idealized amplitude modulation scheme	128
5.4	Modulated light pulses	132
5.5	Numerical calculations of some FP-spectra of the light pulses	134
5.6	FP spectrum of the modulated light	135
6.1	Longitudinal velocity distribution of the atoms	138
6.2	Image of the undeflected atomic beam	142
6.3	Image of the deflected atoms using ARP sequences	143
6.4	Phosphor Screen	145

6.5	Image of the deflected atoms including a magnetic field.	146
6.6	Image of the deflected atoms including a magnetic field detuned from resonance	149
6.7	Deflected atoms on the phosphor screen for different settings .	151
6.8	Subset of deflection images for the Force-Map	153
6.9	Force Map ARP	155
6.10	Force Map ARP including magnetic field	156

List of Tables

3.1 Spectroscopic Data for He* transitions	64
4.1 Settings of the PID-controller for the laser locking.	91

Chapter 1

Introduction

Laser cooling and trapping of neutral atoms is a well known field, which was first proposed about 30 years ago [1, 2]. It gives answers to fundamental questions about atoms and also the opportunity to do research with BECs, optical lattices and cold Fermions. Apart from that, it also has a wide range of practical applications, such as atomic clocks, atomic lithography (which is done in this lab as well), atomic lasers and nowadays especially quantum computing. The basic process in laser cooling is the directional transfer of momentum from an electromagnetic field to atoms. In this chapter a brief description of the theoretical principles of laser cooling will be given.

1.1 The two-level atom

1.1.1 The Schrödinger equation

The interaction of an atom with a radiation field can be described by a Hamiltonian of the form: $H(t) = H_0 + H'(t)$, where H_0 is the field free, time independent Hamiltonian and $H'(t)$ describes the coupling between the atom and the radiation field. The following holds for the time independent Hamiltonian: $H_0 \Phi_n(\vec{r}) = E_n \Phi_n(\vec{r})$ with the eigenenergies $E_n = \hbar\omega_n$ and the eigenfunctions Φ_n . These form a complete set and so the wave-functions, which are the solutions of the Schrödinger equation $H\psi(\vec{r}, t) = i\hbar\frac{\partial\psi(\vec{r}, t)}{\partial t}$ can be expanded as follows:

$$\psi(\vec{r}, t) = \sum_k c_k(t) \Phi_k(\vec{r}) e^{-i\omega_k t}$$

Therefore the Schrödinger equation can be written as

$$H(t)\psi(\vec{r}, t) = [H_0 + H'(t)] \sum_k c_k(t) \phi_k(\vec{r}) e^{-i\omega_k t} = i\hbar \left(\frac{\partial}{\partial t} \right) \sum_k c_k(t) \phi_k(\vec{r}) e^{-i\omega_k t} \quad (1.1)$$

When multiplying both sides of this equation with $\phi_j^*(\vec{r})$ from the left and integrating over the spatial coordinates \vec{r} , the general Schrödinger equation then becomes:

$$i\hbar \frac{dc_j(t)}{dt} = \sum_k c_k(t) H'_{jk}(t) e^{i\omega_{jk}t}, \quad (1.2)$$

with $\omega_{jk} = (\omega_j - \omega_k)$ and $H'_{jk}(t) = \langle \Phi_j | H'(t) | \Phi_k \rangle$.

This equation is in general not solvable. An often useful simplification is to look only at those two levels that are important for the atomic interaction with an (almost) resonant light field. Obviously there is no two-level atom in nature. However, this is a useful approximation, when the monochromatic light field couples strongly only to two of the electronic states of the atom. These two levels are called the ground ($|g\rangle$) and the excited state ($|e\rangle$) of the atom, which interacts with the light field. This is the so called Rabi problem [3, 4, 5]. It is solved by absorbing any diagonal elements of $H'(t)$ into H_0 . Doing this, only one nonzero value ($H'_{ge}(t) = H'_{eg}^*(t)$) remains in the summation. With respect to that, equation 1.2 becomes

$$i\hbar \frac{dc_g(t)}{dt} = c_e(t) H'_{ge}(t) e^{-i\omega_a t}$$

and

$$i\hbar \frac{dc_e(t)}{dt} = c_g(t) H'_{eg}(t) e^{i\omega_a t} \quad (1.3)$$

with the atomic resonance frequency ω_a .

1.1.2 Rabi oscillations between two states

The interaction Hamiltonian for an atom in an electromagnetic field in a semi-classical approach is given by [6]:

$$H'(t) = -e \vec{r} \cdot \vec{E}(\vec{r}, t), \quad (1.4)$$

where $\vec{p} = e \vec{r}$ is the dipole moment of the atom, \vec{r} the position of the electron and \vec{E} is the electric field vector.

Since only two atomic levels connected by a single, narrow-band excitation are being considered two approximations can be made at this point: One is the so called rotating wave approximation (RWA) which neglects all terms with $\frac{1}{\omega_1}$ when compared to terms of order $\frac{1}{\delta}$. The detuning $\delta \equiv \omega_1 - \omega_a$ is the difference between the laser frequency ω_1 and the frequency of atomic resonance ω_a (figure 1.1). The second useful simplification is the electric dipole approximation: The spatial variation of $\vec{E}(\vec{r}, t)$ is negligible over the region of the spatial integral of $H'_{ge}(t)$ because the wavefunctions $\Phi_n(\vec{r})$ are nearly completely contained within a sphere of a radius that is typically < 1 nm, while the optical wavelength is usually several hundred nm.

With the electric dipole approximation and with a plane wave that propagates in the z-direction, the electric field can be written as: $\vec{E}(\vec{r}, t) = E_0 \hat{e} \cos(kz -$

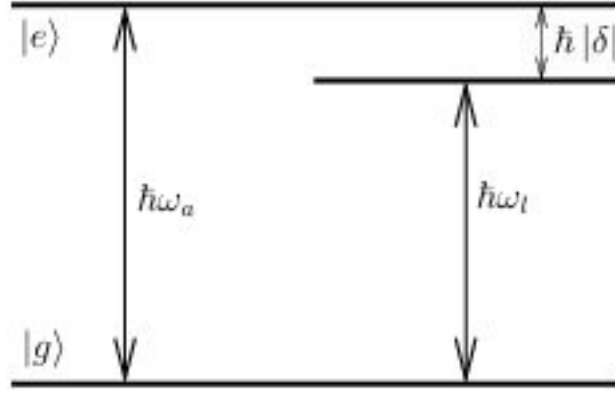


Figure 1.1 Energy levels of a two-level atom with ground state $|g\rangle$ and excited state $|e\rangle$. The separation between these two states is given by $\hbar\omega_a$. The energy of the monochromatic light field is $\hbar\omega_l$ with a detuning from atomic resonance $\delta = \omega_l - \omega_a$.

$\omega_l t$). The Hamiltonian becomes $H_{eg}(t) = \hbar\Omega \cos(kz - \omega_l t)$ with the Rabi-frequency:

$$\Omega = \frac{-e E_0}{\hbar} \hat{\epsilon} \cdot \langle e | \vec{r} | g \rangle$$

Here $\hat{\epsilon}$ is the unit polarization vector, E_0 the amplitude of the light field and \vec{r} is the space operator.

Using the RWA, the two equations 1.3 can be uncoupled, which yields:

$$\frac{d^2 c_g(t)}{dt^2} - i\delta \frac{dc_g(t)}{dt} + \frac{\Omega^2}{4} c_g(t) = 0 \quad (1.5)$$

and

$$\frac{d^2 c_e(t)}{dt^2} + i\delta \frac{dc_e(t)}{dt} + \frac{\Omega^2}{4} c_e(t) = 0. \quad (1.6)$$

For an atom that is initially in the ground state ($c_g(0) = 1$ and $c_e(0) = 0$) the solution is

$$c_g(t) = \left(\cos \frac{\Omega' t}{2} - i \frac{\delta}{\Omega'} \sin \frac{\Omega' t}{2} \right) e^{i\delta t/2} \quad (1.7)$$

and

$$c_e(t) = -i \frac{\Omega}{\Omega'} \sin \frac{\Omega' t}{2} e^{-i\delta t/2} \quad (1.8)$$

The Rabi-frequency determines the oscillation frequency of the populations in the ground and in the excited state. The probability for finding the atom in the ground or excited state oscillates at an angular frequency of

$$\boxed{\Omega' \equiv \sqrt{\Omega^2 + \delta^2}}$$

The oscillation frequency increases with increasing detuning $|\delta|$ from resonance, while the amplitude decreases, since the probability for the atom to be in the excited state scales as $\frac{\Omega}{\Omega'}$ so it becomes smaller.

1.1.3 Dressed states

An alternative description of the interaction of an atom with an electromagnetic field is the dressed atom picture. This means that a coupled system of atom and light field is being considered. This system is then treated as one

system and the eigenfunctions and eigenenergies have to be found.

The Hamiltonian that describes the combined system is given by $H = H_a + H_{\text{rad}} + H_{\text{int}}$, where H_a gives the bare atomic energy levels, $H_{\text{rad}} = \hbar\omega_1(a^\dagger a + \frac{1}{2})$ with the Eigenvalues $E_n = (n + \frac{1}{2})\hbar\omega_1$ gives the radiation part and H_{int} describes the interaction between atom and field (see equation 1.4, AC Stark shift). Here, a^\dagger (a) is the bosonic creation (annihilation) operator.

The first two terms describe the atom as in the Bohr picture, but with a vertical displacement for each energy quantum $\hbar\omega_1$ that is added from the light field. This can be viewed in figure 1.2. The nearly degenerate pairs produced in this way are indicated by a dashed line in figure 1.2.

The third term describes the atomic dipole interaction and is responsible for the coupling of the ground and the excited states, where the amount of mixture of these two states is expressed by a mixing angle θ : $\cos(2\theta) = \frac{-\delta}{\Omega}$. The dressed states are therefore given by:

$$|\phi_1\rangle = \cos\theta |g\rangle - \sin\theta |e\rangle$$

and

$$|\phi_2\rangle = \sin\theta |g\rangle + \cos\theta |e\rangle.$$

Thus, the eigenvalues of H_0 are not the eigenvalues of the combined Hamil-

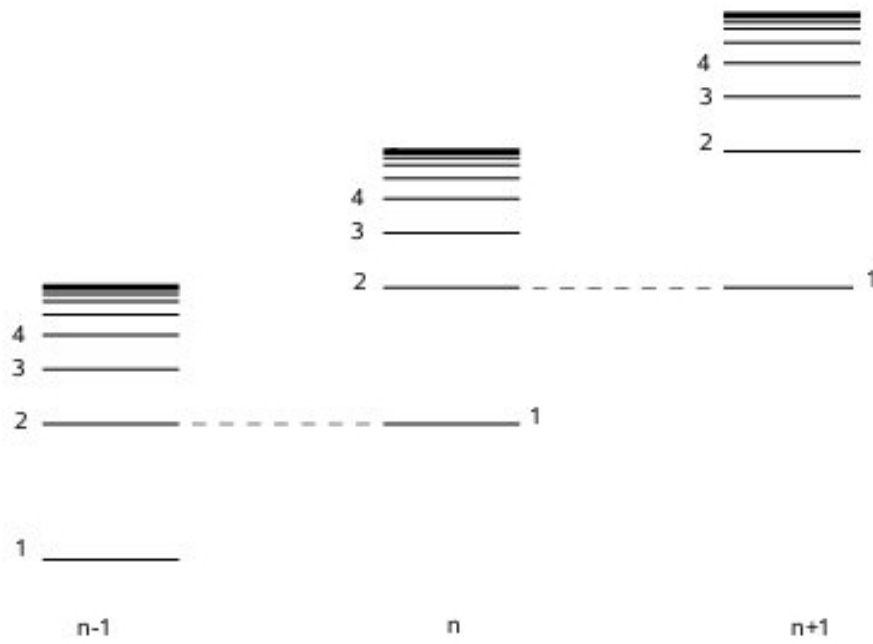


Figure 1.2 Energy level diagram of an atom in an electromagnetic field. The columns are vertically shifted for different n because an energy amount of $\hbar\omega_1$ is added per column. The nearly degenerate pairs are indicated by dashed lines.

tonian any more, since the Hamiltonian is no longer diagonal (off diagonal matrix elements are present because of the field). The result of the calculation for the shifted energy is (approximated) [7]:

$$E_{e,g} = \frac{\hbar}{2}(-\delta \mp \Omega')$$

For $\Omega \ll |\delta|$ the energy shift is

$$\Delta E_g = \frac{\hbar\Omega^2}{4\delta}$$

and

$$\Delta E_e = -\frac{\hbar\Omega^2}{4\delta}$$

In figure 1.3, the shifted energies due to the field are shown.

An interesting point is that the light shifts of these dressed states vary in a standing wave configuration (zero at nodes and maximum at antinodes) and due to this spatial variation of the internal atomic energy, a force on the atoms can be observed (dipole force). This will be described later.

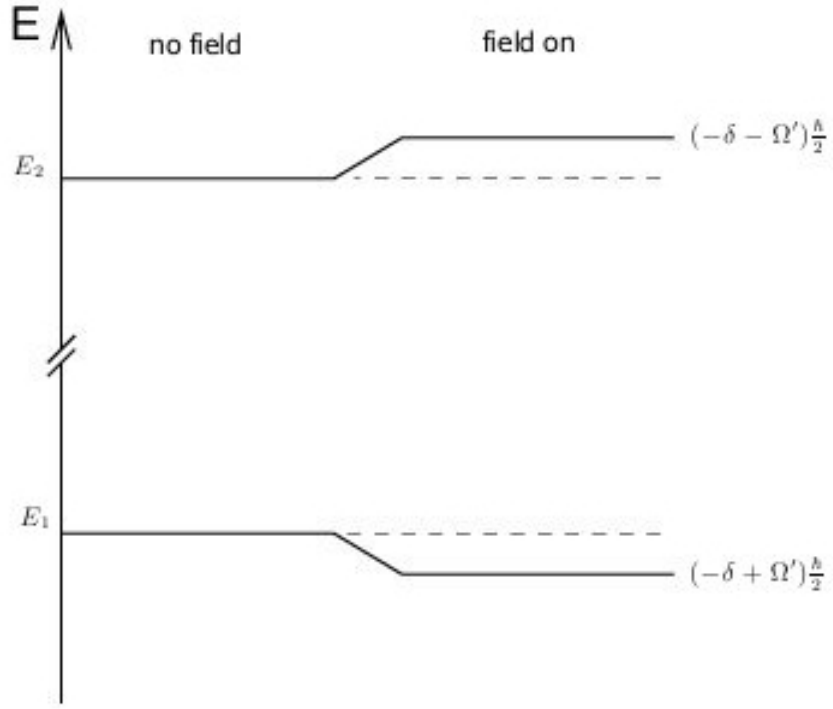


Figure 1.3 Energies of two coupled states with and without an applied light field. The shift of the level energy is called light-shift.

1.2 The Bloch Sphere

Equations 1.3 are repeated here for convenience:

$$i\hbar \frac{dc_g(t)}{dt} = c_e(t) H'_{ge}(t) e^{-i\omega_a t}$$

and

$$i\hbar \frac{dc_e(t)}{dt} = c_g(t) H'_{eg}(t) e^{i\omega_a t}.$$

Considering these equations of motion in a rotating frame and defining a vector \vec{R} , with

$$r_1 \equiv c_g c_e^* + c_g^* c_e,$$

$$r_2 \equiv i(c_g c_e^* - c_g^* c_e),$$

and

$$r_3 \equiv |c_e|^2 - |c_g|^2$$

a very simple correlation follows:

$$\boxed{\frac{d\vec{R}}{dt} = \vec{\Omega} \times \vec{R}} \quad (1.9)$$

Obviously $|\vec{R}| = |c_e|^2 + |c_g|^2 = 1$. The torque vector $\vec{\Omega}$ consists of the three components $\text{Re}(H'_{ge})$, $\text{Im}(H'_{ge})$ and $\hbar\delta$, where $\text{Im}(H'_{ge})$ vanishes when H' is taken to be real. The result can be visualized in the picture of the Bloch Sphere [9, 10], where the south pole of this sphere represents the ground state of the atom and the north pole stands for the excited state in the two level picture. Other points represent various superpositions, e.g. points in the equatorial plane represent equal superpositions. The Bloch vector precesses around the torque vector with constant length so that its motions takes place on the surface of a sphere (figure 1.4). The Bloch picture is a powerful tool of

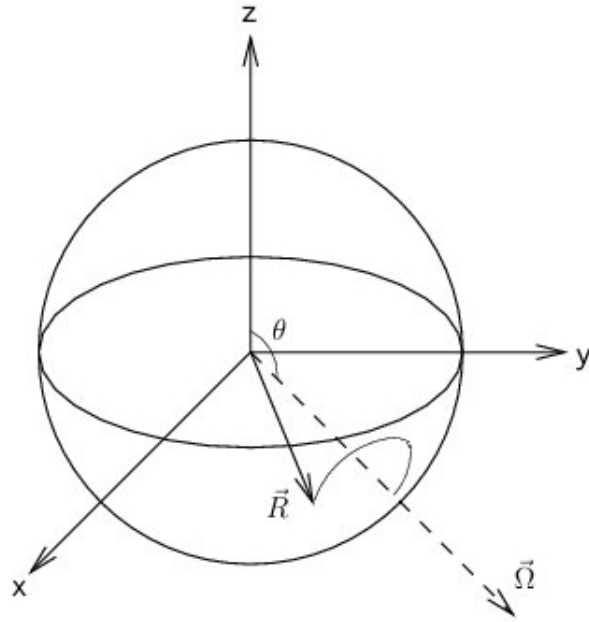


Figure 1.4 Illustration of the Bloch Sphere. The Bloch vector \vec{R} precesses around the torque vector $\vec{\Omega}$ on the surface of the sphere.

describing the interaction of an atom with a light field [7], as demonstrated in later chapters.

1.3 Radiative Force

An atom at rest interacting with a monochromatic laser light field tuned near the frequency of atomic resonance does not only gain internal energy from the field but also experiences momentum kicks of $\hbar\vec{k}$, where \vec{k} is the wave-vector of the electromagnetic wave and therefore the motional energy is $\frac{(\hbar k)^2}{2m} \cdot N$, where

N is the number of momentum kicks. This momentum kick during absorption will always be in the direction of the laser beam. The excited state can again decay to the ground state via spontaneous emission. This will give the atom another momentum kick, but this time in a random direction as spontaneous emission does not have a preferred direction. This process also increases the entropy of the system. Therefore after many of those cycles, the recoil kicks, that the atom suffers from spontaneous emission average to zero, but the momentum kicks it gets from each absorption process add up and push the atom in the direction of the laser beam (radiation pressure). This is shown in figure 1.5.

Quantitatively, the force on an atom caused by absorption of light followed by spontaneous emission can be written as

$$F = \hbar k \gamma \rho_{ee}, \quad (1.10)$$

where $\hbar k$ is the momentum kick gained from each absorption process, γ is the rate of the process and ρ_{ee} is the population of atoms in the excited state (in steady state) and is given by [7]:

$$\rho_{ee} = \frac{s}{2(1+s)} = \frac{s_0/2}{1+s_0+(2\delta/\gamma)^2}, \quad (1.11)$$

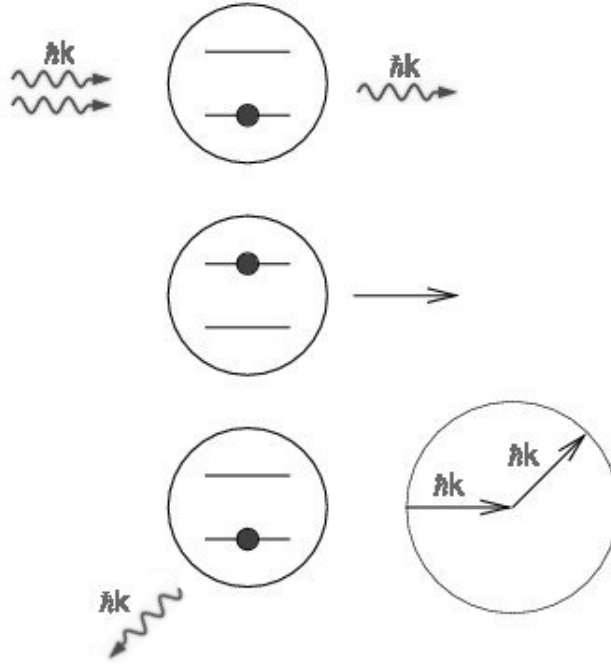


Figure 1.5 Production of the radiative force. The atom absorbs an energy amount of $\hbar\omega$ from the field, while the two-level atom is excited and a momentum of $\hbar\vec{k}$ is transferred to the atom. The atom can decay via spontaneous emission, where the momentum transfer takes place in a random direction and therefore averages to zero after many cycles. As a result, a net momentum is transferred to the atom in the laser propagation direction.

with the saturation parameter $s \equiv \frac{s_0}{1 + (\frac{2\delta}{\gamma})^2}$, the on resonance saturation parameter $s_0 \equiv \frac{2|\Omega|^2}{\gamma^2} = \frac{I}{I_s}$ and the saturation intensity $I_s = \frac{\pi \hbar c}{3\lambda^3 \tau}$. Here τ is the lifetime of the excited state.

Because of the fact that the excited state decays with a rate γ and as the excitation rate and the decay rate are equal in steady state, the total scattering

rate can be determined as

$$\gamma_p = \gamma\rho_{ee} = \frac{s_0\gamma/2}{1 + s_0 + (2\delta/\gamma)^2} \quad (1.12)$$

Combining equations 1.10 and 1.12 we finally get:

$$\boxed{F_{sp} = \frac{\hbar k s_0 \gamma / 2}{1 + s_0 + (2\delta/\gamma)^2}} \quad (1.13)$$

It is interesting to note, that this radiative force is not unlimited. Increasing the intensity does not mean that the force is always getting larger because when you take into account that this also increases stimulated emission, it is obvious that the maximum value is $F_{sat} = \frac{\hbar k \gamma}{2}$, since the maximum value for high intensities for ρ_{ee} is $1/2$ (see 1.11 for $s \gg 1$). This fact limits the applications of the radiative force enormously.

The equation for calculating the radiative force 1.13, changes when the atom is moving with a small finite velocity \vec{v} . The frequency of the light that is "seen" by the atom is actually Doppler shifted:

$$\omega' \approx \omega - \vec{k} \cdot \vec{v}.$$

If the frequency of the light from the atoms point of view is below (above) the

transition frequency it is called *red* (*blue*). The radiative force of a moving atom is then given by

$$\vec{F}_{\text{rad}} = \frac{s_0 \gamma / 2}{1 + s_0 + \left(\frac{2}{\gamma} (\delta - \vec{k} \cdot \vec{v}) \right)^2} \hbar \vec{k}. \quad (1.14)$$

1.4 Doppler-Cooling

As discussed in the previous section, atoms in a laser field tuned to resonance between two atomic levels suffer a net force in the direction of the laser beam. In 1975 Hänsch et al. proposed to use this force to slow down (cool) atoms [1]. Since then, the field of laser cooling became more and more popular and has various applications now. An atom that travels along a line and is hit by a laser beam that travels opposite to the direction of the atoms motion experiences a radiative force (see chapter 1.3) resulting in a slowing of its motion. This mechanism works best, if the laser beam is tuned slightly below atomic resonance making use of the Doppler effect. When the atom travels in the direction of the laser beam, it is much more unlikely that it absorbs energy and momentum from the beam because the light is tuned even further away from resonance under consideration of the Doppler effect.

An atom, which has a velocity of \vec{v} in the laboratory frame sees the light

with an added frequency shift of $\omega_D = -\vec{k} \cdot \vec{v}$. Therefore, the light field should be detuned with an effective detuning of $\delta_{\text{eff}} = \delta + \omega_D$. For on resonance light, the force is centered for atoms with zero velocity, but for off-resonance laser light, the center of the force is shifted to the group of atoms moving with a velocity of $\vec{v} = \frac{\delta \vec{k}}{k^2}$. The radiative push of the laser, that is moving to the right has its force maximum shifted to the atoms moving to the left and for the laser beam moving to the left it is the other way round in a red detuned ($\delta < 0$) laser field. For low intensities the forces can just be added and it holds [7]:

$$\begin{aligned}
\vec{F} &= \hbar \vec{k} \frac{\gamma s/2}{1 + s + (2(\delta - \vec{k} \cdot \vec{v})/\gamma)^2} - \hbar \vec{k} \frac{\gamma s/2}{1 + s + (2(\delta + \vec{k} \cdot \vec{v})/\gamma)^2} \\
&\approx \frac{8\hbar \vec{k} \delta s \vec{v} \cdot \vec{k}}{\gamma(1 + s + (2\delta/\gamma)^2)^2} \\
&\equiv -\beta \frac{\vec{k}(\vec{k} \cdot \vec{v})}{k^2}
\end{aligned} \tag{1.15}$$

Since this is an approximation in the limit of small velocities ($k v < \gamma, \delta$), terms of the order of $\left(\frac{k v}{\gamma}\right)^4$ or higher can be neglected. Note, that this force is only a cooling force for $\delta < 0$ ($\rightarrow \beta > 0$). The force is illustrated in figure 1.6. The velocity capture range of the force that results from this Doppler-cooling is $v = \frac{\gamma}{k}$. This corresponds to a Doppler shift, that pushes the atom out of its natural absorption linewidth.

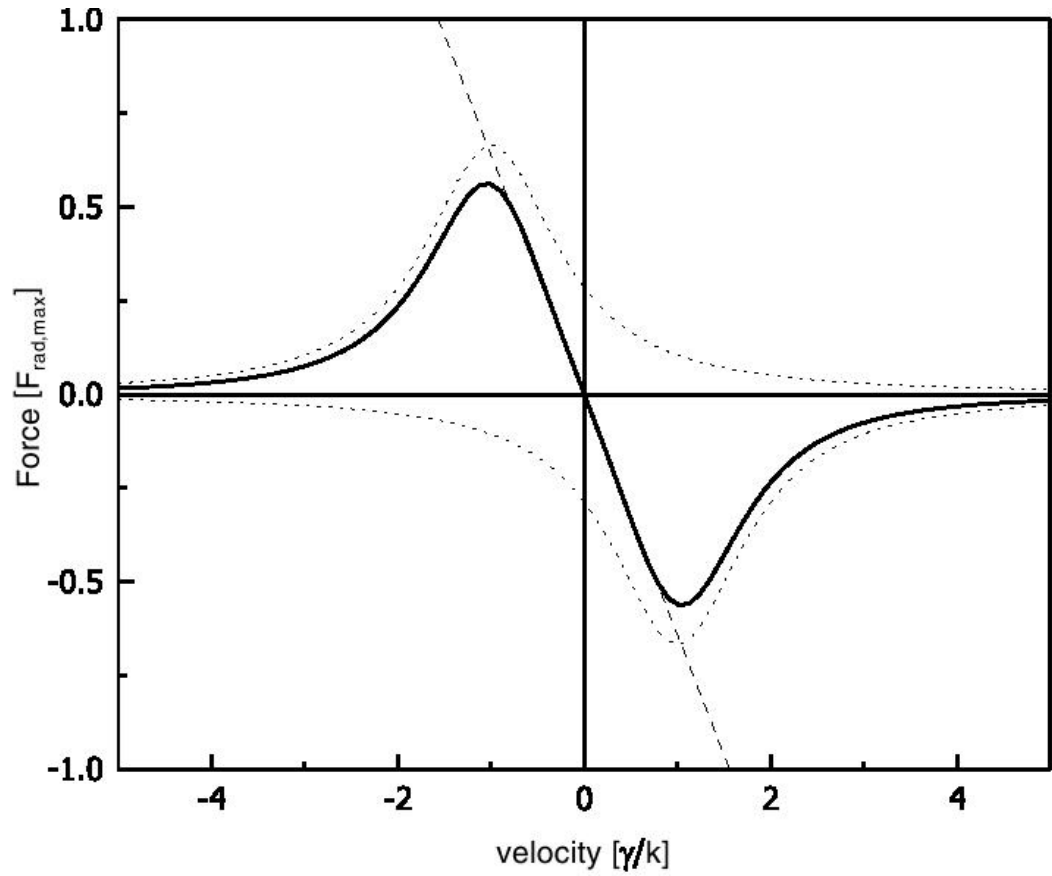


Figure 1.6 Calculated force on atoms with velocity v for two counterpropagating laser beams (optical molasses). The parameters are set to $s = 2$ and $\delta = -\gamma$. The two dotted lines represent the force for each individual beam and the solid line shows the combined force. The dashed line has a slope of $-\beta$ [13].

So the idea is to slow down atoms that travel in random directions. This is accomplished with two counterpropagating laser beams in each spatial direction. Atoms that live in such a field of crossed light fields will be slowed down in either direction. This is called optical molasses because of the properties of the atomic motion in this medium. But this type of cooling has some limitations: When the atoms become slower because of the interaction with the field, the laser light is not tuned to resonance any more with respect to the Doppler effect. So another absorption process becomes more unlikely. There are some methods to avoid this limit. One is, to let the atomic beam travel through an inhomogeneous magnetic field, where the Zeeman-shift varies and so the light is always tuned to atomic resonance (Zeeman slower). Another problem is that the atoms gain a mean kinetic energy (and therefore a mean temperature) because of the interaction with the field. It is not possible to cool below this so called "Doppler-limit" with Doppler Cooling. This limit is [11]

$$k_{\text{B}}T_{\text{D}} = \frac{\hbar\gamma}{2}. \quad (1.16)$$

and is given by the Brownian motion theory. Here k_{B} is the Boltzmann-constant. The Doppler Temperature T_{D} ranges from several hundred μK to tens of μK for the typical atoms that are used in laser cooling (Alkalis and metastable noble gas atoms). But there are some other techniques, that cir-

cumvent this difficulty and result in even lower temperatures (sub-Doppler Cooling). It is important, that this cooling mechanism confines the atoms in momentum space, but not in space itself. In order to do both, it is possible to trap the atoms in space which is often done with magnetic fields. The process of laser cooling has to be irreversible in order to get the dissipation that is needed to compress the volume in phase space. This irreversibility is realized by spontaneous emission and hence increase of entropy.

1.5 Optical Pumping

One of the main goals of the work for this thesis is to manipulate metastable He-atoms in order to produce a two-level system. This is done by optical pumping [11], which will be explained in this section. In the experiment, the He transition $2^3S_1 \longrightarrow 2^3P_2$ is used. Without an external magnetic field the Zeeman-sublevels of the atomic levels are degenerate and are expected to be equally populated. The level 2^3S_1 has three ($m_j = -1, 0, 1$) and 2^3P_2 has five sublevels ($m_j = -2, -1, 0, 1, 2$). When an external magnetic field is applied, the Zeeman-sublevels will no longer be energetically degenerate. The energy shift due to the field is given by

$$E_{m_j} = m_j g_j \mu_B B, \tag{1.17}$$

where $\mu_B = \frac{e\hbar}{2m_e}$ is the Bohr-magneton (m_e is the electron mass), B is the magnetic field and g_j is the Lande-factor, which is given by $g_j = 1 + \frac{j(j+1)+s(s+1)-l(l+1)}{2j(j+1)}$. Here, s , l and j are the quantum numbers of the electronic spin (\vec{s}), angular momentum (\vec{l}) and the total electronic momentum (\vec{j}) respectively.

As explained in section 1.1.2, coupling of atoms with external fields causes transitions between the energy levels of the atom. However, those transitions only occur (in a first approximation), when the corresponding matrix element of the external field H_{ext} does not vanish [11]. If it vanishes, this results in the so called selection rules. This means, that not all transitions are allowed. Some important selection rules for the atom are for instance $\Delta J = 0, \pm 1$ [without $(J=0) \rightarrow (J=0)$], $\Delta S = 0$, $\Delta L = 0, \pm 1$ and $\Delta m_J = 0, \pm 1$ [without $(m_J = 0 \rightarrow m_J = 0)$ when $\Delta J = 0$].

When linearly polarized π -light is shone on the atom, there will be a transition with $\Delta m = 0$ (e.g. $m_j = 1$ (2^3S_1) \rightarrow $m_j = 1$ (2^3P_2)). The excited state can decay with $\Delta m_j = 0, \pm 1$ (selection rules) and since this can happen to all the magnetic sublevels of the ground state, there will be no average change in the population. But there is an elegant method to populate specific sublevels at the cost of the others. This method is called Optical Pumping and is based on the carefully chosen properties of the light field.

If however circularly polarized light is shone on an atom (e.g. σ^+ -light)

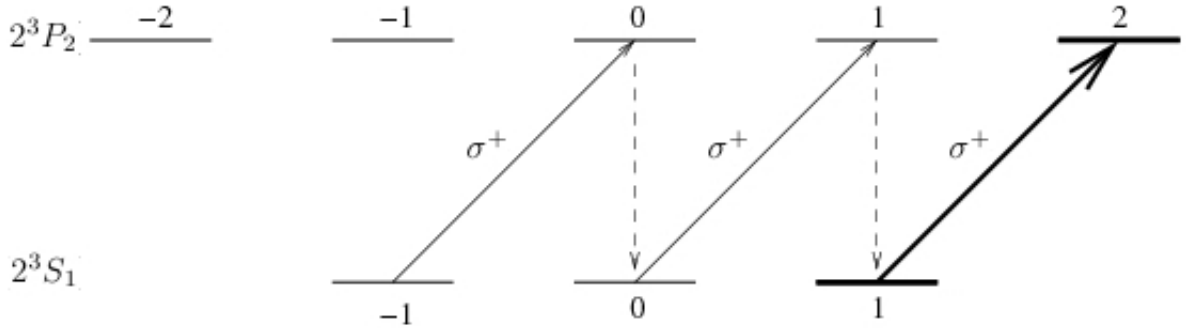


Figure 1.7 Schematic of the Optical Pumping process, using the metastable He 2^3S_1 -level as ground state and the He 2^3P_2 -level as excited state. By applying a magnetic field and σ^+ -light, the population in the $m_j = +1$ ground state is increased at the cost of the $m_j = 0, -1$ sublevels. With σ^+ -light, only the $1 \rightarrow 2$ transition is driven, which is indicated by the bold arrow. The energy shift between the sublevels due to the magnetic field is not shown.

in a magnetic field, the transition with a change in the magnetic quantum number of $\Delta m = 1$ is much more likely than any other transition because of the selection rules described above (angular momentum conservation, see also [7]). Consider an He-atom that is in the ground state with $m_j = -1$: When circularly polarized σ^+ -light interacts with the atom, the probability for a transition to the excited $m_j = 0$ sublevel is much higher than to for instance the excited $m_j = -1$ sublevel. The excited state can decay into either the $m_j = -1$ ground state or into the $m_j = 0$ ground state. In the first case, there is no change in the population, but the atom can be excited again by the circularly polarized light as described above. In the second case, the population of $m_j = 0$ in the ground state has grown at the cost of the

population in $m_j = -1$. The same process can now take place for the sublevels of the ground state with $m_j = 0$ and $m_j = 1$. On average, the Zeeman-level with the highest quantum number will be populated and the other sublevels will be emptied. Since there is σ^+ -light shining on the He-atom, the transition $m_j = 1$ (2^3S_1) \rightarrow $m_j = 2$ (2^3P_2) will be most likely because the population in the other sublevels is much lower (figure 1.7). Thus, the atom becomes a two-level atom for the transition between 2^3S_1 and 2^3P_2 . If left-circularly polarized light is used (σ^-), it is the same as described above with the difference, that the lowest sublevel will be populated.

1.6 Dipole Force

Atoms experience a force (light shift) when they are travelling in an inhomogeneous light field, which is for instance caused by two counterpropagating beams (standing wave). Another point of view is to see this dipole force as a result of absorbing light from one beam and stimulated emission into the other beam of the standing wave [13]. The net momentum exchange is $2\hbar k$ for each absorption and emission process, which is illustrated in figure 1.8. This force is not limited by spontaneous emission as is the radiative force and can therefore be arbitrarily large. However, the force vanishes when averaged over a wavelength because the light field is symmetric and thus there is no

preferred direction for absorption or stimulated emission. The requirement of irreversibility of the cooling process (see 1.4) is not fulfilled here since the force is conservative. The dipole force therefore cannot be used to cool atoms, however it can be used to trap atoms. In order to get a preferred direction for a momentum transfer it is necessary to break the symmetry in the standing wave configuration. There are different ways to implement a symmetry breaking in order to get a non vanishing force on atoms. One example for successful symmetry breaking is the use of optical pumping between different atomic levels that have been light shifted by the polarization gradient of a field (polarization gradient cooling), whereas the optical pumping is enabled by spontaneous emission.

In order to make better use of the dipole-force, a method has been proposed that involves two-frequency light fields with a non-vanishing dipole force. One way to implement this is to produce a light field that is composed of two standing waves with different frequencies. The force that is caused by this field does not vanish and is called rectified dipole force. One of the fields causes a large enough light shift, so that the detuning of the first field is spatially modulated. But the force of the first field has to be much smaller than the one of the second field. However, this force cannot be used for the cooling of atoms since it is conservative due to the absence of spontaneous emission. Another

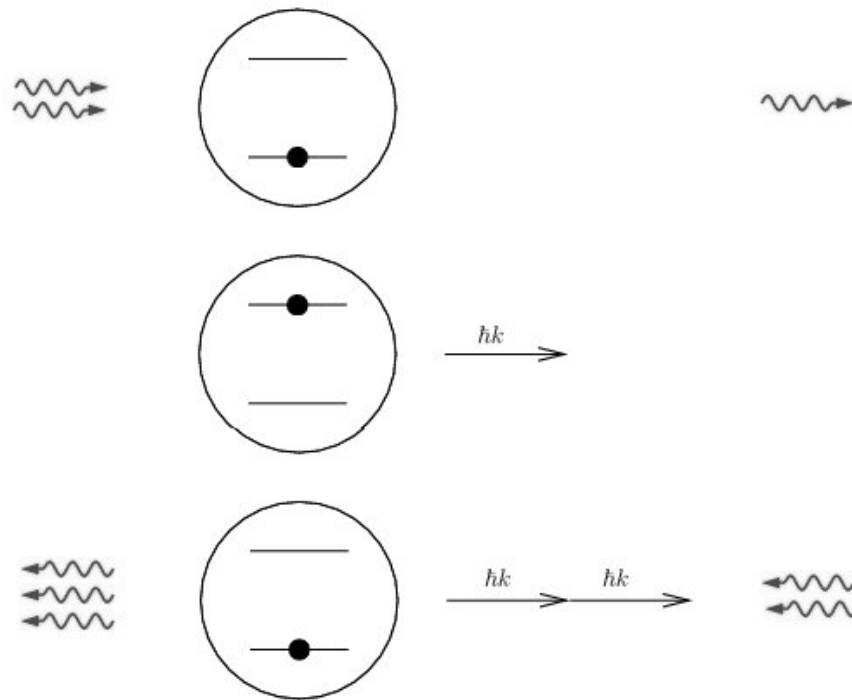


Figure 1.8 Production of the dipole force. The atom is subject to a standing wave light field that is made by two counterpropagating monochromatic light beams. Momentum is transferred from the field to the atom, when an amount of energy $\hbar k$ from one beam is absorbed by the atom. This process is followed by stimulated emission into the other beam, which results in a net momentum transfer of $2\hbar k$ to the atom for each cycle.

disadvantage is, that this mechanism depends very much on the detuning of the two beams and therefore can only handle small Doppler shifts. Thus, it does not work for an ensemble of atoms with different speeds.

1.7 Bichromatic Force

The interest in the dipole force originates from the fact that it can be several times larger than the radiative force. When the frequencies of the light fields that cause the dipole force are changed in a certain way, it is possible to produce a non-vanishing dissipative force that can be used to cool atoms. When there is spontaneous emission among the dressed states of the atom, the process is no longer reversible. However, recently doubts came up if spontaneous emission is indeed necessary for the irreversibility of the process since the bichromatic force can be explained without making use of this mechanism. New ways of solving the problem have been proposed [15]. In the bichromatic case, two light beams are used, which are detuned in opposite directions from atomic resonance by $\pm\delta$. So the picture given in the previous chapter does not apply any more as the detuning from resonance is not large. The bichromatic force is very efficient in slowing and cooling atoms and is described below.

1.7.1 The π -Pulse Model

One way of describing the bichromatic force is the π -pulse model [17, 18, 19]. The two counterpropagating beams are both detuned from atomic resonance and have a frequency of $\omega_a \pm \delta$, where δ is the detuning. The field that results from those beams has an oscillation frequency ω_a and a much lower modulation frequency δ which encloses the fast oscillations (figure 1.9). The resulting electric field is given by

$$\begin{aligned} E(z, t) &= E_0 \cos((k + \Delta k)z - (\omega_a + \delta)t) + E_0 \cos((k - \Delta k)z - (\omega_a - \delta)t) \\ &= 2E_0 \cos(kz - \omega_a t) \cos(\delta t - \Delta kz). \end{aligned} \quad (1.18)$$

When a two-level atom is in the ground state, it can be driven to the excited state by one of these pulses, if the amplitude of the pulse drives exactly one half-cycle of a Rabi-oscillation (π -pulse). In the Bloch-sphere picture a π -pulse drives the Bloch vector from the south pole of the sphere to its north pole. This flip is accompanied by an energy exchange of $\hbar\omega_a$ and a momentum exchange of $\hbar k$. The π -pulse condition reads

$$\int_{-\frac{\pi}{2\delta}}^{\frac{\pi}{2\delta}} 2\Omega_0 \cos(\delta t) dt = \pi, \quad (1.19)$$

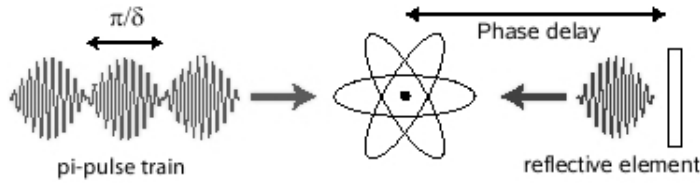


Figure 1.9 Coherent momentum transfer, making use of bichromatic pulse trains. The delay time between the arrival of the two pulses of the counter-propagating pulse trains can be set by positioning the mirror.

with $\Omega_0 = \frac{\pi\delta}{4}$.

Another pulse, that comes from the opposite direction can now cause stimulated emission and drive the atom back to the ground state with another recoil momentum kick of $\hbar k$ in the same direction as the first momentum kick so that the overall gain of momentum for the atom is $2\hbar k$. If this cycle is repeated many times a huge force can be produced. The momentum transfer using bichromatic pulse trains is illustrated in figure 1.9. Without spontaneous emission, the magnitude of the force is $F = \frac{\Delta p}{\Delta t} = \frac{2\hbar k\delta}{\pi}$, where $t = \frac{\pi}{\delta}$ is the duration of one pulse. Since there is no limitation by spontaneous emission, the bichromatic force can be much larger than the ordinary radiative force ($F_{sp} = \frac{\hbar k\gamma}{2}$), when $\delta \gg \gamma$. In the case of spontaneous emission, the atom can return to the ground state before the next pulse arrives, so that this pulse excites the atom rather than causing stimulated emission. In this case, the direction of the force is switched. In a symmetric field, no direction is preferred and so the net force vanishes. But in an asymmetric field, a preferred

direction of the force is produced. This can be (for instance) achieved by using an uneven arrival time spacing among the pulses in the two directions. When the time delay between two pulses therefore is chosen to be $t/4$ instead of $t/2$ in an even arrival time spacing, the probability of spontaneous emission between the pulses ($\frac{3t}{4}$) is three times larger than the probability within the pulses ($\frac{t}{4}$). Thus, it is more likely to find an atom in the ground state before the arrival of a pulse pair than between them before the second pulse arrives (figure 1.10). Since this $\Phi = \frac{\pi}{2}$ phase delay reduces the average magnitude of the force by a factor of 2, it yields for the bichromatic force in this special case: $F_b = (\frac{3}{4} - \frac{1}{4}) 2\hbar k \frac{\delta}{\pi} = \frac{\hbar k \delta}{\pi}$.

The π -pulse approach provides an intuitive insight into the bichromatic force and with some simple assumptions a good estimation of the force is obtained. Apart from these advantages, this picture lacks on other points. The temporal overlap between the pulses is left out for instance and also the velocity dependence of the force is not considered here. A better analysis is therefore the doubly-dressed atom picture which will be illustrated in the following section.

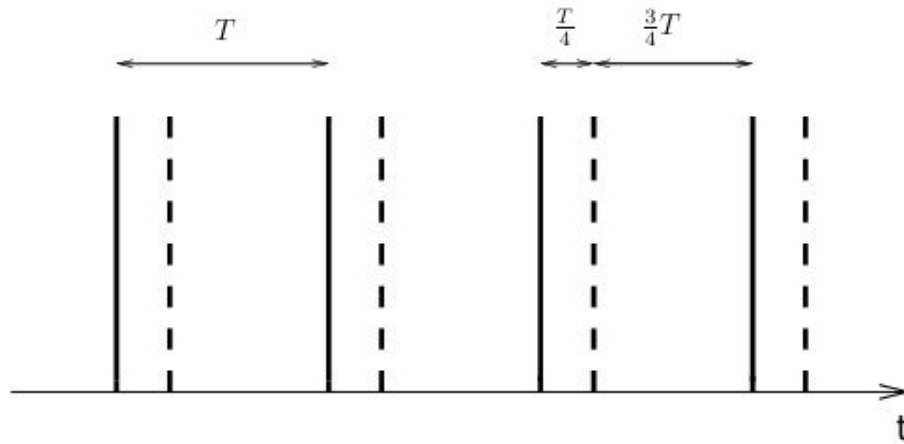


Figure 1.10 Production of an unidirectional force using bichromatic π -pulses. The solid lines mark the center of the right propagating π -pulses, while the dashed lines mark the left propagating π -pulses. The separation between the pulses is $\frac{T}{4}$ within each pair and $\frac{3T}{4}$ between neighboring pairs. A net force is produced because the longer time for spontaneous emission between the pulse pairs make it more likely to find the atom in the ground state before the arrival of the pulse pair than to find it in the excited state.

1.7.2 The doubly dressed atom picture

As it was described in chapter 1.1.3, the electromagnetic field causes light shifts of the atomic levels (\rightarrow dressed states). In the bichromatic force picture, there are two frequency components that are oppositely detuned from resonance. So in the doubly dressed atom picture, the atom is dressed by the blue detuned standing wave light field ($\omega_a + \delta$) and by the red detuned standing wave light field ($\omega_a - \delta$). The overall electric field can be written as

$$E = 2E_0 \cos(kz + \frac{\chi}{2}) \cos[(\omega_a + \delta)t] + 2E_0 \cos(kz - \frac{\chi}{2}) \cos[(\omega_a - \delta)t], \quad (1.20)$$

where $\chi = 2\Delta kz = 2\delta \frac{z}{c}$ is the spatially phase shift between the two standing waves.

The diabatic states of the doubly dressed atom are the product states of the atom and the light field (see dressed states, section 1.1.3). The resulting states can be written as $|g, b, r\rangle$ and $|e, b, r\rangle$, where $|g\rangle$ represents the ground state and $|e\rangle$ the excited state of the bare atom, while b and r stand for the quantum numbers in the blue and red detuned field respectively. This means that each pair of diabatic states in the dressed atom picture now becomes an infinite set of equally spaced states with a spacing of $\hbar\delta$.

The Hamiltonian of the atom-field system can be written in a set of the di-

abatic eigenstates bases as an infinite tridioagonal matrix. Here, the truncated 7×7 matrix over \hbar is given [14, 16]:

$$\begin{pmatrix} 3\delta & \Omega_2 & 0 & 0 & 0 & 0 & 0 \\ \Omega_2 & 2\delta & \Omega_1 & 0 & 0 & 0 & 0 \\ 0 & \Omega_1 & \delta & \Omega_2 & 0 & 0 & 0 \\ 0 & 0 & \Omega_2 & 0 & \Omega_1 & 0 & 0 \\ 0 & 0 & 0 & \Omega_1 & -\delta & \Omega_2 & 0 \\ 0 & 0 & 0 & 0 & \Omega_2 & -2\delta & \Omega_1 \\ 0 & 0 & 0 & 0 & 0 & \Omega_1 & -3\delta \end{pmatrix}$$

The off diagonal elements in this matrix are the spatially dependent Rabi frequencies of the standing wave of each frequency component divided by two:

$$\Omega_{1,2} = \Omega_0 \cos(kz \pm \frac{\chi}{2}). \quad (1.21)$$

By diagonalizing the Hamiltonian that is given above, the approximate values for the position dependent eigenenergies of the doubly dressed atom can be calculated. Those are plotted in figure 1.11 for $\delta = 10\gamma$ and $\chi = \frac{\pi}{4}$ with a 11×11 Hamiltonian.

At the nodes of one of the two components of the light field, the Rabi frequency of this component vanishes, e.g. $\Omega_2 = 0$. So the uncoupled states

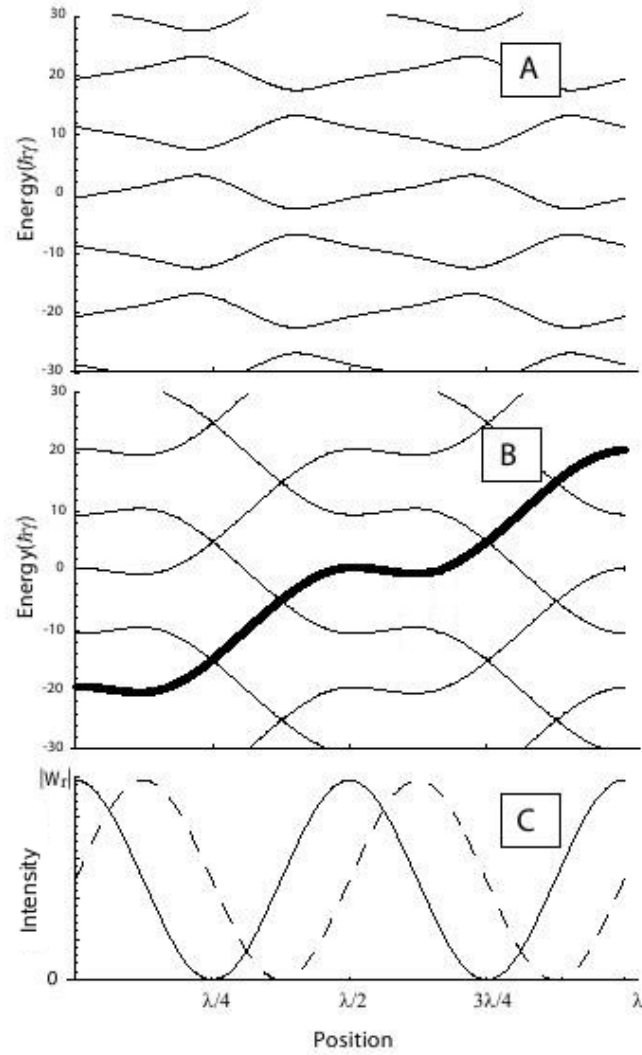


Figure 1.11 Spatial dependence of the dressed state energy levels for $\delta = 10\gamma$ and $\chi = \frac{\pi}{4}$. (A) $\Omega_0/\delta = \pi/4$, which is the π -pulse condition. (B) $\Omega_0/\delta = \sqrt{6}/2$. (C) Plot of the standing wave intensities. The levels are equally spaced where the intensities of the two standing waves are equal. At the node of one standing wave energy level crossing occurs when the Rabi-frequency of the other standing wave satisfies special conditions. Here it holds: $\Omega/\delta = \sqrt{6}/2$. The bold line in (B) shows a possible path of an atom moving through the real crossings which give rise to the large bichromatic force.

can cross the frequency of the second standing wave at some critical value of Ω_1 . It is therefore possible for atoms to climb this so called Landau-Zener ladder [13], which produces the large bichromatic force. The conditions for the level crossing are [16]:

$$\Omega_0 \cos(\cos(kz - \frac{\chi}{2})) = 0$$

and

$$\Omega_0 \cos(\cos(kz + \frac{\chi}{2})) = \delta \sqrt{n^2 - \frac{1}{2}}, \quad (1.22)$$

with $n = 1, 2, 3, \dots$. Solving equation 1.22 gives us the relationship between Ω_0 and χ . For $\chi = \frac{\pi}{4}$ it holds that $\Omega_0 = \sqrt{\frac{3}{2}}\delta$. In the π -pulse model this means $\Phi = \frac{\pi}{2}$, but the π -pulse condition requires $\Omega_0 = \frac{\pi}{4}\delta$.

It is clear that the reverse process, which means that an atom climbs down the Landau Zener ladder, is possible too, but again asymmetric pulse timing provides a directional force.

The optimal force condition that is obtained by solving equations (1.22) agrees well with the numerically calculated force, using the Bloch equation 1.9 with spontaneous emission included and applying the Ehrenfest theorem. The magnitude of the force can be calculated by the slope of the eigenenergy levels of the doubly dressed atom in the crossing condition. Spontaneous emission

is included by weighting the excited state component in the eigenstates of the atom. The same result as in the π -pulse model is confirmed.

Chapter 2

The theoretical background of Adiabatic Rapid Passage

This thesis is about the optical force on atoms that is resulting from Adiabatic Rapid Passage (ARP). In this chapter the basics of this effect will be explained. ARP is used to invert the population of a two level system and was originally used in magnetic resonance [20]. The application in optics has been studied in recent years and also in the context of this thesis. In order to make use of ARP in the optical regime it is necessary to sweep the frequency of the light through the resonance of the two level system [21, 22], which has to be done repeatedly for a large force. Therefore, two counterpropagating beams are produced to exchange momentum as described in chapter 1. Each cycle results in a momentum exchange of $2\hbar k$ and with a high repetition rate ($\frac{1}{T} \gg \gamma$) the force $F_{\text{ARP}} = \frac{2\hbar k}{T}$ [23] is much larger than the traditional radiative force

$F_{\text{rad}} = \frac{\hbar k \gamma}{2}$ [24]. Most of this chapter is taken from the PhD-thesis of Dr. Xiyue Miao [13].

2.1 ARP - an introduction

In this section a closer look on the effect of Adiabatic Rapid Passage of a two level atom will be taken. In order to observe this process, a chirped pulse can be used, which means that the carrier frequency of the light is chirped and the amplitude is pulsed. It will first be looked at the ARP-process from the dressed atom view of the two-level system [24, 26]. In the frame that is spanned by instantaneous dressed atom states (adiabatic frame [27]), the Hamiltonian of the system is

$$H(t) = \frac{\hbar}{2} \begin{pmatrix} \delta(t) & \Omega(t) \\ \Omega(t) & -\delta(t) \end{pmatrix}. \quad (2.1)$$

The Eigenenergies are given by $E(t)_{\pm} = \pm(\frac{\hbar}{2})\sqrt{\delta(t)^2 + \Omega(t)^2}$, with the Rabi frequency $\Omega(t)$ and the detuning from resonance $\delta(t)$. When the low-intensity domain where $\Omega < \delta$ in the diabatic frame for $\delta > 0$ is considered, the upper eigenstate approaches the ground state $|g\rangle$ and conversely for the lower one. In the case of $\delta < 0$ the identification is reversed. This is illustrated in figure 2.1 showing these limits near the $\Omega = 0$ plane. Away from the low intensity limit, $|g\rangle$ and $|e\rangle$ are mixed on two eigenenergy sheets.

If the amplitude and frequency sweep is slow enough, the state of the two level system follows one of the dressed atom eigenstates adiabatically and the population will therefore be inverted. So the dressed atom eigenstate of the system follows a trajectory similar to that of the bold line in figure 2.1, where δ_0 is the amplitude of the frequency sweep. Note, that only the trajectory on the upper energy sheet is shown. The trajectory on the lower energy sheet behaves similarly. If spontaneous emission is considered, it is obvious that the sweep rate ω_m has to be rapid enough to satisfy the condition $\omega_m \gg \gamma$, where γ is the spontaneous scatter. So the name **A**diabatic **R**apid Passage is justified.

Another useful point of view is to look at the system in the Bloch picture (see section 1.2). The vertical axis z of the Bloch-sphere is the population difference term and the horizontal axes are related to the relative phase of the atomic superposition. The equation of motion of the Bloch vector is given by equation 1.9. Since the ARP-process involves a synchronized frequency- and amplitude-sweep, the torque vector sweeps across the Bloch Sphere from one pole to the other along a meridian. Assuming that the initial state is an eigenstate, then the Bloch-vector \vec{R} will perform a precession around the torque vector from one pole to the other. In case of a slow sweep, the Bloch-vector is always close to the torque-vector (adiabatic) and an inversion of the

population is accomplished. The trace of the Bloch vector in the adiabatic frame [13], where the projection of the torque vector on the Bloch Sphere is fixed at the origin, is shown in figure 2.2. The adiabatic frame itself rotates with the torque vector. The deviation of the Bloch vector from point 0 is always small for adiabatic following. It starts from point 0 and ends there too over the duration of the pulse, which indicates a complete conversion.

Slow enough in this case means, that

$$|\vec{\Omega}(t)| \gg \frac{d\theta}{dt}, \quad (2.2)$$

with the mixing angle θ , that is given by $\theta(t) = \arctan\left(\frac{\delta(t)}{\Omega(t)}\right)$. In the Bloch-picture, θ is the angle between $\vec{\Omega}$ and the vector that points to the north pole. Equation 2.2 indicates, that the angular frequency of the torque vector is much smaller than the angular frequency of the Bloch vector, which means that the Bloch-vector follows adiabatically. If the adiabatic condition of Equation 2.2 is not satisfied, there is no adiabatic following of the Bloch vector and there will be a small fraction of the population that will not be inverted after the sweep (non-adiabatic transition). For a high efficiency of momentum transfer the probability for non-adiabatic transition (P_{nad}) must be kept small. A more quantitative look at this probability will be taken in the following section.

2.2 The probability for nonadiabatic transition

The ARP problem is in general a level crossing problem. This has been extensively studied for the infinite case [28, 29, 30]. But the pulse length must be finite in order to apply multiple repetitive ARP-sweeps for optical force production and therefore the nonadiabatic transition probability has different properties. The first step of calculating P_{nad} is the numerical integration of 1.9 for various finite time chirped pulses [13]. The time dependence of the intensity and frequency of for instance a cosinusoidally-chirped sinusoidal pulse is given by:

$$\begin{aligned}\Omega(t) &= \Omega_0 \cos(\omega_m t) \\ \delta(t) &= \delta_0 \sin(\omega_m t),\end{aligned}\tag{2.3}$$

with $t \in [-\frac{T}{2}, \frac{T}{2}]$ and $\omega_m = \frac{\pi}{T}$. In the special case of $\Omega_0 = \delta_0$, which has been studied in some detail [31], $|\vec{\Omega}|$ is constant and $\vec{\Omega}$ satisfies:

$$\frac{d\vec{\Omega}}{dt} = \vec{\omega}_m \times \vec{\Omega},\tag{2.4}$$

with an artificial constant vector $\vec{\omega}_m$. For this case, the nonadiabatic transition probability is:

$$P_{\text{nad}} = \frac{x^2}{1+x^2} \sin^2 \left(\frac{\pi}{2} \sqrt{\frac{1+x^2}{x^2}} \right),\tag{2.5}$$

with the non-dimensional parameter $x = \frac{\omega_m}{\Omega_0}$. However, there is no analytical solution for the general case of $\Omega_0 \neq \delta_0$, but nevertheless numerical calculations can be done. Now an integration for a single sweep (half cycle of Eq. 2.3) is done and the excited state component of the population is calculated. In the ideal case, \vec{R} ends close to the north pole of the Bloch Sphere and the population is nearly inverted which means that the atom absorbs a momentum of $\hbar k$ from the light field. The remaining ground state population (ρ_{gg}) at the end of the sweep gives the non-adiabatic transition rate of the process. Therefore:

$$P_{\text{nad}} = \rho_{gg} = \frac{1 - r_3}{2}, \quad (2.6)$$

with r_3 taken from chapter 1.2. In figure 2.3, ρ_{gg} is plotted for various values of Ω_0 and δ_0 both in units of ω_m . Obviously the result of [31] is reproduced for the case of a constant $\Omega_0 = \delta_0$ (see equation 2.4). This corresponds to the diagonal of figure 2.3. Other points in figure 2.3 belong to various elliptical trajectories. The numerical calculation can of course be used for other finite time chirped pulses than the case given above. A more detailed discussion of the nonadiabatic transition probability can be found in [13].

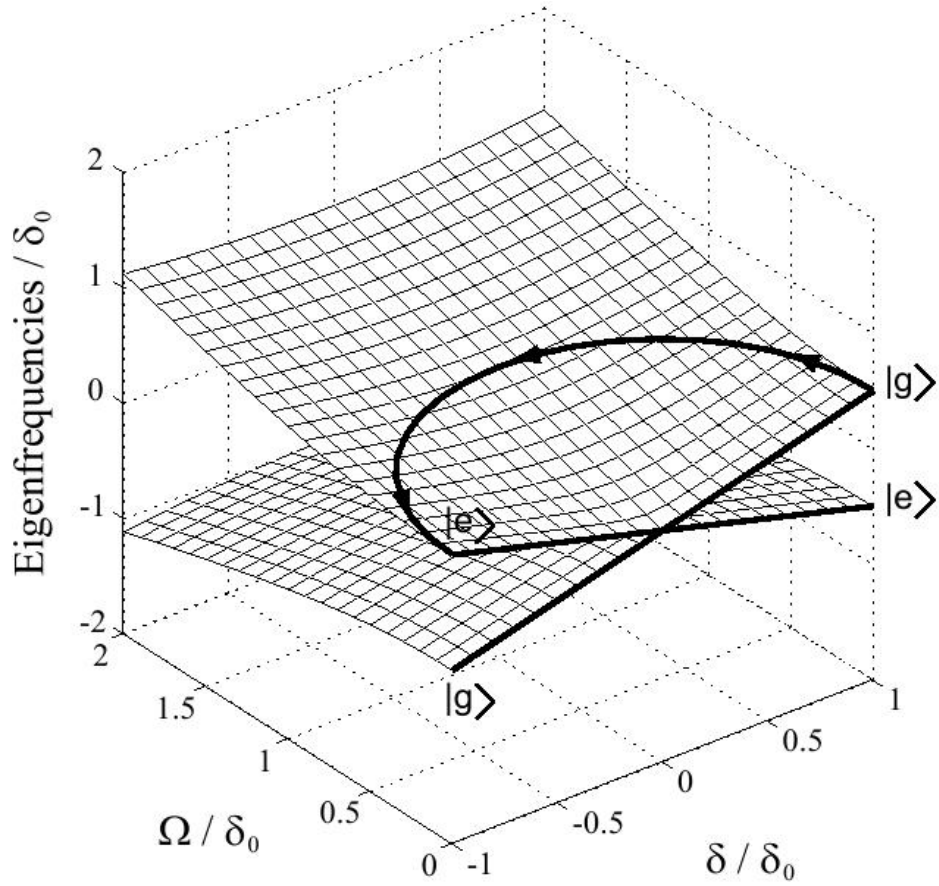


Figure 2.1 The energy of the dressed states comprise two separate sheets except at the conical intersection at the origin. The upper (lower) state is ground at $\Omega = 0$ for $\delta > 0$ ($\delta < 0$). The indicated path is the trajectory for ARP [13].

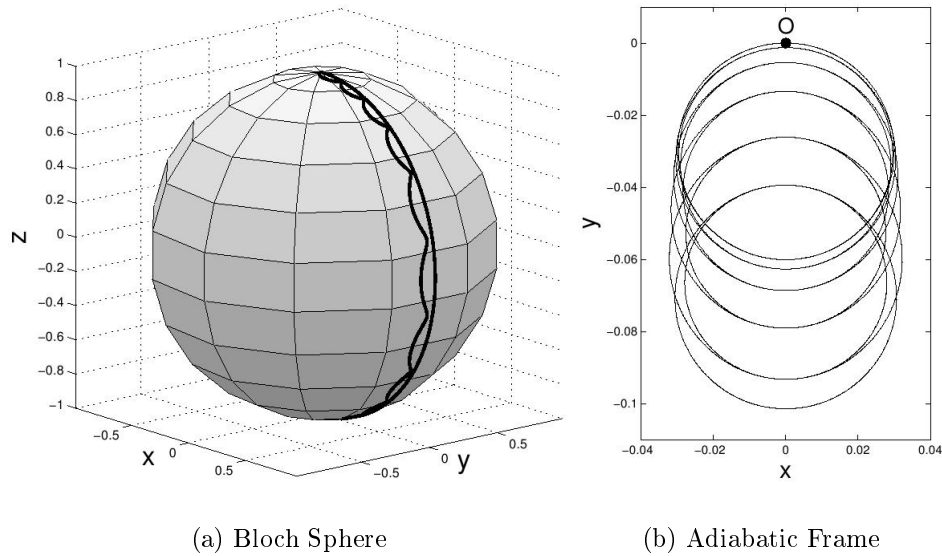


Figure 2.2 Schematic of the adiabatic following of the Bloch vector along the torque vector of a modulated light field. In (a), the wavy curve connecting the two poles is a typical trace of the Bloch vector on the Bloch Sphere. The meridian close to it is the trace of the torque vector across the Bloch Sphere. The light field is a cosinusoidally-chirped sinusoidal pulse with parameters $(\frac{\delta_0}{\omega_m}, \frac{\Omega_0}{\omega_m}) = (25.0, 18.724)$. In (b), the relative position of the Bloch vector and the torque vector is shown more clearly in the adiabatic frame. Note, that the scale of the plot is very small, so the deviation of the Bloch vector from the torque vector is actually small all the time, i.e. the adiabatic following [13].

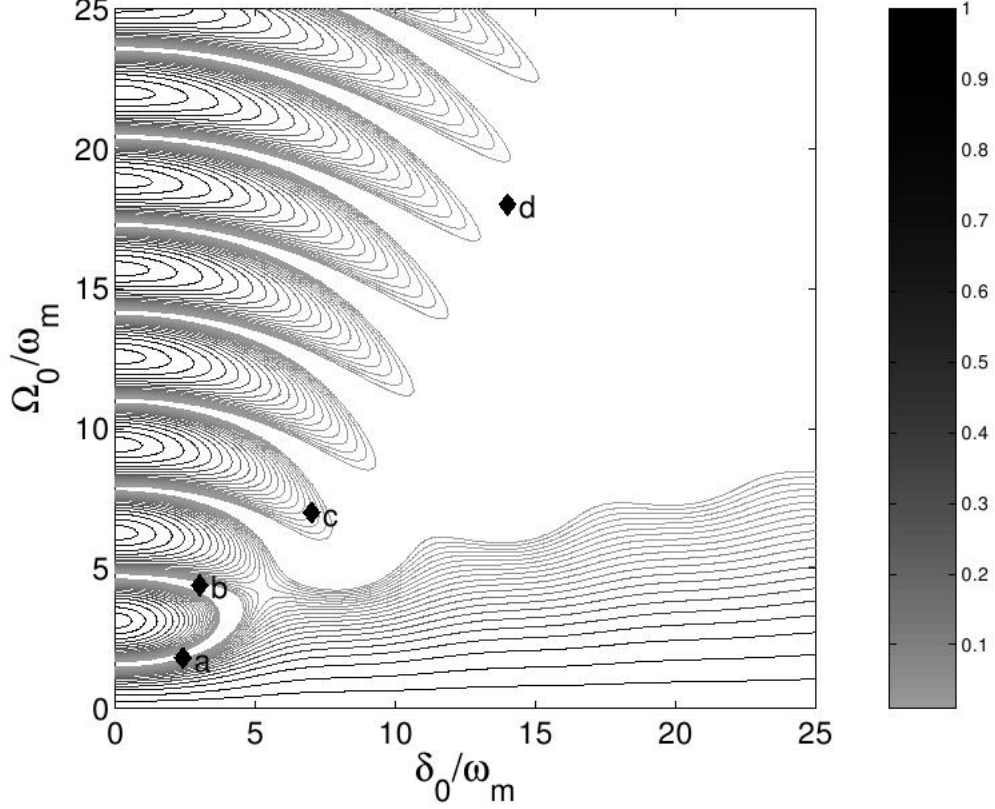


Figure 2.3 A contour plot of the numerical values of ρ_{gg} vs. δ_0 and Ω_0 after one sweep. The diagonal of this plot reproduces the results of reference [31]. Note that the z-coordinate is the reciprocal of the "rapidity" parameter in [31]. The large open areas towards the upper right corner represent regions where $\rho_{gg} < 0.01$, so the probability of non-adiabatic transitions is negligibly small. Each contour line is a step of 0.01 so the point (c) is at $\rho_{gg} = 0.02$. Interest lies in those special areas that are close to the origin where ρ_{gg} is still small, since those are the values of Ω_0 and δ_0 that can be accomplished easily with the equipment in this experiment. The pathway along the vertical axis, $\delta_0 = 0$, that is punctuated by narrow white regions represents pulses of area $n\pi$ that also produce inversion ($n = \text{odd integer}$). The indicated points represent $\left(\frac{\delta_0}{\omega_m}, \frac{\Omega_0}{\omega_m}\right) =$ (a) - (2.4, 1.8), (b) - (3.0, 4.4), (c) - (7.0, 7.0) and (d) - (14.0, 18.0) and will be referred to later (figure 2.5) [13].

2.3 Periodic ARP on a two level system

In this section, the case of a two-level atom that is influenced by multiple ARP-sweeps will be discussed (see also [24]). The equation for the motion of the Bloch vector is given by 1.9:

$$\frac{d\vec{R}}{dt} = \vec{\Omega} \times \vec{R}. \quad (2.7)$$

In the ideal case, the atomic population will be inverted by an ARP pulse, which is for instance described by $\Omega(t) = \Omega_0 \sin(\omega_m t)$, $\delta(t) = \delta_0 \cos(\omega_m t)$ for $t = 0 \rightarrow \frac{\pi}{\omega_m}$. This means that the Bloch vector \vec{R} starts from the south pole of the sphere at $t = 0$ and ends at its north pole at $t = \frac{\pi}{\omega_m}$. For $t = \frac{\pi}{\omega_m} \rightarrow \frac{2\pi}{\omega_m}$ (second half circle of the signal) \vec{R} will return back to the south pole. Population inversion after one sweep means that \vec{R} is lying near the south pole after two sweeps, but this is not necessarily true for the reverse.

To gain such a high force it is necessary that the two pulses have different \vec{k} -vectors in addition to the requirement of population inversion. Due to the fact that the development of \vec{R} on the Bloch Sphere is independent on the propagation direction of the light-pulses, two sweeps form a complete cycle. This can be written as

$$\vec{R}(T) = U(T) \vec{R}(0), \quad (2.8)$$

where the cycle starts with $t = 0$ and ends at $T = \frac{2\pi}{\omega_m}$. $U(T)$ is an operator that is determined by the whole history of the torque vector $\vec{\Omega}$ from $t = 0$ to T . Another point of view is to see $U(T)$ as a rotation of the sphere. Note, that $U(t)$ also is a rotation when t is chosen to be arbitrary and \vec{R} remains on the surface of the sphere [24]. This perspective has the advantage that since the rotation of the sphere does not depend on the Bloch vector, all cycles can be treated equally (figure 2.4). In addition, only the situation at the end of each cycle is interesting, so it is only looked closer at $\vec{R}(n T)$, with $n = 1, 2, 3, \dots$, which makes the situation a lot easier.

Starting with the situation that the Bloch vector is in the ground state, so $\vec{R}(0) = (0, 0, -1)$, while the first cycle brings it to a point displaced from the south pole: $\vec{R}(T) = U(T) \vec{R}(0)$. For a description of the rotation in spherical coordinates, the polar angle (θ_a) and the azimuthal angle (Φ_a) are required for the definition of the rotation axis and another angle α is needed to define the rotation. These three angles are determined by the parameters of the laser sweep $\vec{\Omega}(t)$ with t from $t = 0$ to T . Note, that the axis and the rotation angle are the same for each cycle. It is therefore obvious, that the n points that mark the values of $\vec{R}(n T)$ are lying on a circle on the Bloch Sphere. For the chosen initial condition, this circle passes through the south pole of the sphere, while the center of it lies on the axis of rotation, which is described by

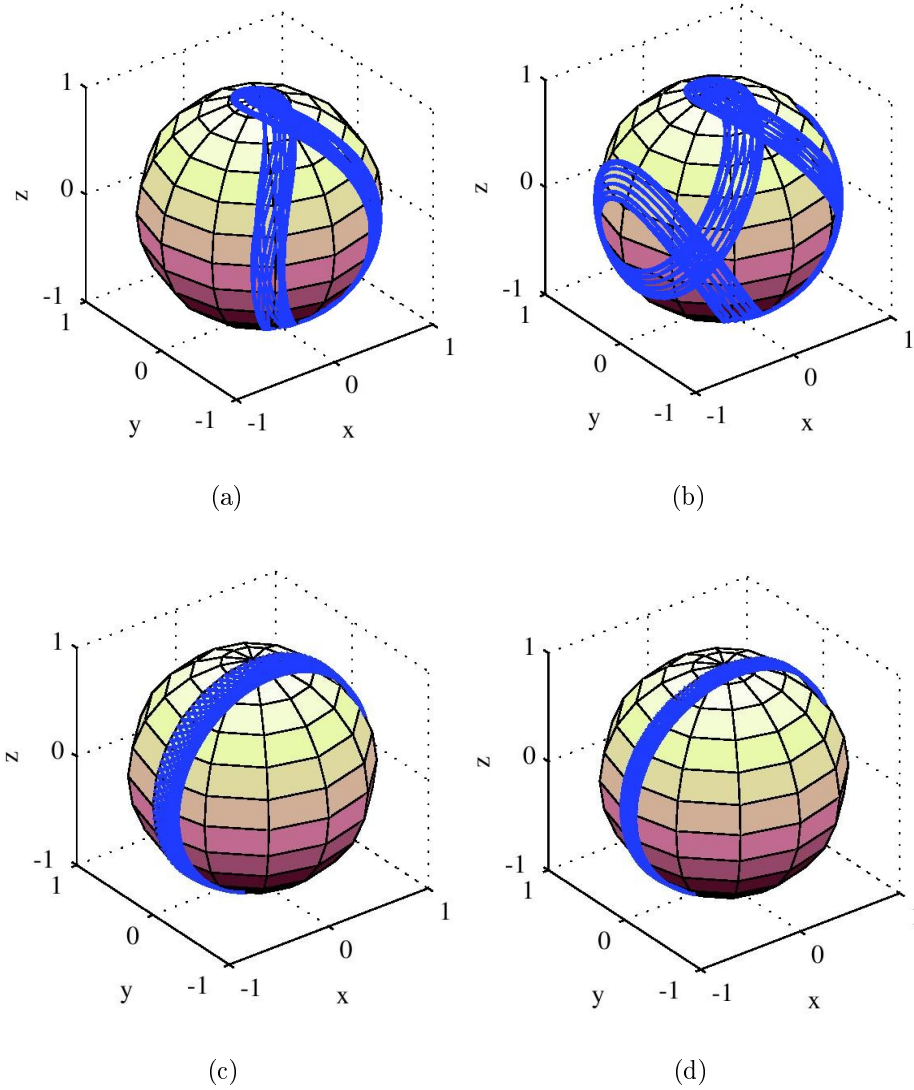


Figure 2.4 A set of trajectories of \vec{R} on the Bloch Sphere using the same laser parameters as in Figure 2.3 and 2.5. The trajectories are confined to bands whose nearly constant width is essentially the same as the diameter of the circles in figure 2.5 [13].

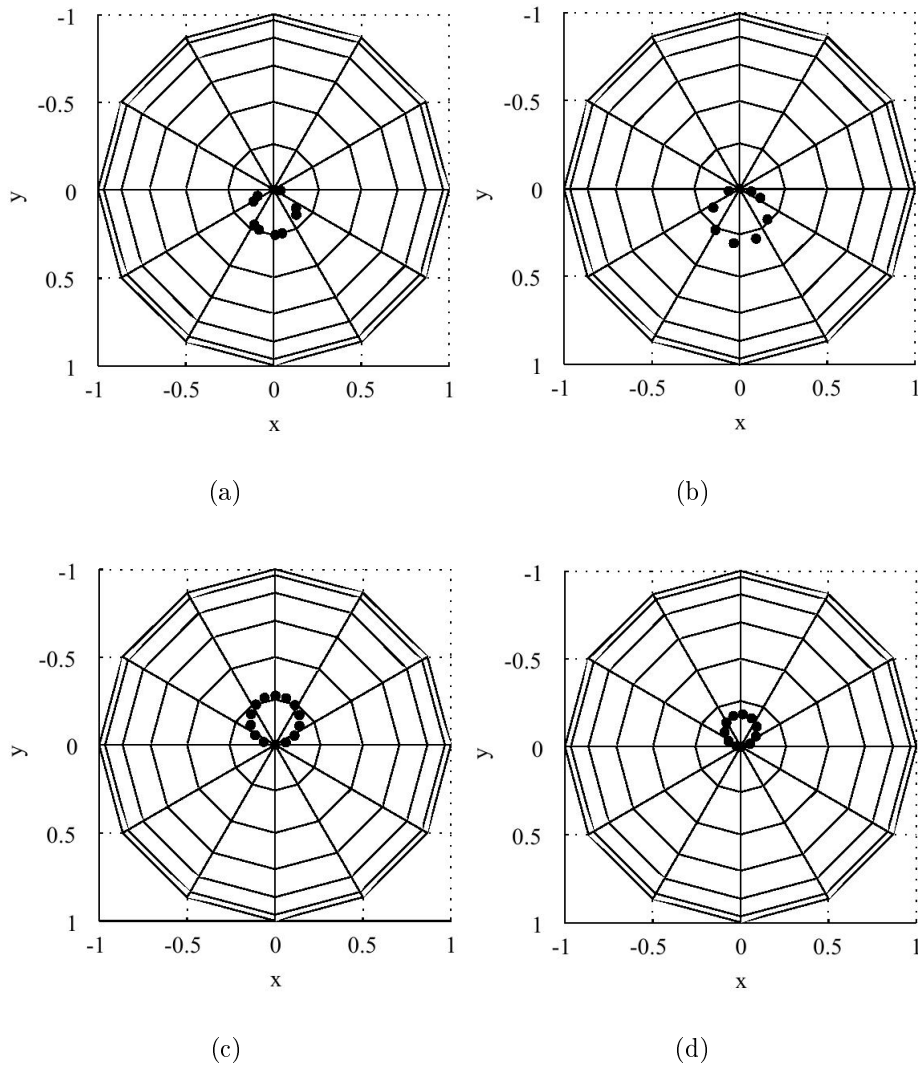


Figure 2.5 Plots showing calculated values of $\vec{R}(nT)$ on the Bloch Sphere as viewed from the south pole. Each set of points lies on a circle whose radius and center depend on the sweep parameters. These parameters are the same as those for parts (a) through (d) in figure 2.3. The points appear to be not evenly spaced (e.g. part (a)) because the rotation angle is large and more than one full rotation is shown [13].

θ_a and Φ_a as defined above. Here $\vec{R}(nT)$ has points separated by αr_0 with the radius of the circle r_0 . In case of α being a rational multiple of 2π , the points cyclically overlap. When this requirement is not satisfied, the points form a discontinuous circle. For (nearly) ideal laser parameters, which means that all $\vec{R}(nT)$ are close to the south pole, the radius is $r_0 \ll 1$ since $|\vec{R}| = 1$ (figure 2.5). However, it is important to know that $\vec{R}(T)$ being close to the south pole (αr_0 is small) does not necessarily mean that $r_0 \ll 1$. The circle, that is formed by the $\vec{R}(nT)$'s can even be as large as a meridian circle in that case. As can be seen in figure 2.5, \vec{R} is found somewhere on a circle after a pair of pulses (one cycle). This circle is preserved throughout the cycle because the trajectory $\vec{R}(t)$ of all the $\vec{R}(nT)$'s during the pulse can also be represented by the rotation of the Bloch Sphere itself. Note, that all the $\vec{R}((n + \frac{1}{2})T)$ lie on a circle through the north pole. The paths swept out by the tip of all Bloch vectors are thus confined within a band swept by the circle on the Bloch Sphere (a few trajectories can be viewed in figure 2.4).

2.4 The ARP-Force

After a few explanations about the nature of Periodic Adiabatic Rapid Passage, the force on a two level atom that results from this process will now be described quantitatively. The Ehrenfest-theorem can be used for this purpose

[7].

$$\vec{F} = \langle -\nabla H \rangle = \frac{\hbar}{2}(\mathbf{r}_1 \nabla \Omega_1 + \mathbf{r}_2 \nabla \Omega_2). \quad (2.9)$$

Here, r_i is the i -th component of the Bloch-vector \vec{R} as described in chapter 1.2 and Ω_i represents the i -th component of the torque vector $\vec{\Omega}$. In this experiment it is dealt with counterpropagating light fields in one dimension, with the torque vectors $\vec{\Omega}_+$ (right propagating field) and $\vec{\Omega}_-$ for the left propagating light field. The resulting force for this case is

$$F = \frac{\hbar k}{2}((\vec{\Omega}_+ - \vec{\Omega}_-) \times \vec{R})_3, \quad (2.10)$$

where k is the wave number of the fields. Now two cases have to be distinguished. In the case of temporally coexisting light fields, inter-beam multi photon processes can take place, which makes the calculation of the force quite complicated because it then is a function of the overlapping light fields. But if the two fields do not overlap in time $\vec{\Omega}$ is either $\vec{\Omega}_+$ or $\vec{\Omega}_-$ at a certain time. Under consideration of the equation of motion of the Bloch vector (equation 2.7), the force can then be expressed as

$$F = \pm \frac{\hbar k}{2}(\vec{\Omega}_{\pm} \times \vec{R})_3 = \pm \frac{\hbar k}{2} \dot{r}_3. \quad (2.11)$$

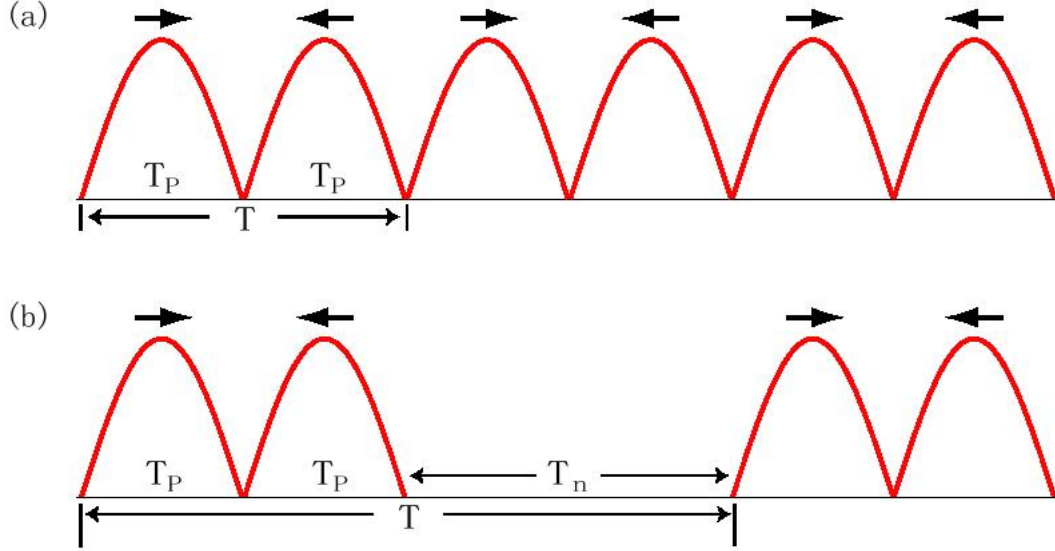


Figure 2.6 Schematics of alternating-directional chirped pulse trains. (a) Continuous chirped pulse pairs from counterpropagating light beams. Spontaneous emission is neglected here. (b) Chirped pulse pairs with half-period syncopation time to accommodate spontaneous emission. The directional force originates from the unsymmetric timing of the counterpropagating pulses [13].

The average force of the unidirectional light pulse can then be written as

$$\bar{F} = \pm \frac{\hbar k}{T_p} \frac{\Delta r_3}{2}. \quad (2.12)$$

If the process is started in the ground state the average force of the pulse is

$$\bar{F} = \pm \frac{\hbar k}{T_p} (1 - P_{\text{nad}}), \quad (2.13)$$

with the nonadiabatic transition probability P_{nad} . The force is $\bar{F} = \pm \frac{\hbar k}{T_p}$ for the

ideal case that the entire momentum $\hbar\mathbf{k}$ is transferred to the atom ($P_{\text{nad}} = 0$). For the ideal ARP-pulse, which means that the counterpropagating chirped pulses do not overlap in time, the atom is lifted to the excited state by the first pulse and brought back to the ground state by the second one via stimulated emission (figure 2.6). During this process, a momentum exchange of $2\hbar\vec{k}$ from the light field to the atom occurs. Thus, the average force on the atom is: $\bar{F} = \frac{2\hbar k}{T}$, where $T = 2T_p$ for an ideal ARP pulse train.

In the case of $P_{\text{nad}} \neq 0$, the force does not reach this maximum. The reduction of the force also depends on the relative phase of the counterpropagating light pulses. The Hamiltonian of an atom in such a field is

$$H_0(t, \mathbf{x}) = \frac{\hbar}{2} \begin{pmatrix} 0 & \Omega_{\pm} \exp [i(\pm kx - \Phi_{\pm})] \\ \Omega_{\pm}^* \exp [-i(\pm kx - \Phi_{\pm})] & 0 \end{pmatrix}. \quad (2.14)$$

The instantaneous phases of the pulses are Φ_{\pm} (for a left and right propagating pulse) and the instantaneous Rabi frequencies are Ω_{\pm} . The position of the atom is x and kx is therefore the phase variation in space. It can easily be seen, that the relative phase of the two pulses varies by 4π in a wavelength, which is 1083 nm in this experiment. Usually the measurements are not made with single atoms, but with an ensemble of atoms, since an atomic ensemble can be produced much simpler and is much easier to deal with. The observed

force is thus the average over all atoms in the atomic beam. If the atomic beam is much wider than the wavelength of the light (in this experiment, the width of the slit is $250 \mu\text{m}$ and $\lambda = 1083\text{nm}$), the average can be taken over all possible relative phases between the two pulses. This is a complicated function of P_{nad} and the relative phase, but assuming symmetric pulses, the mean force on an atom at rest can be written as

$$\boxed{\bar{F} = \frac{2\hbar k}{T}(1 - \sqrt{P_{\text{nad}}})}. \quad (2.15)$$

This is shown in [13]. If the atom is moving at a velocity v , the pulses are Doppler-shifted by $\pm kv$ from the atoms' point of view. Here, the Doppler-shifted fields are in general no longer periodic, unless kv is an integer multiple of $\omega_{\text{m}} = \frac{2\pi}{T}$. In this case, $kvT = 2n\pi$ holds, so that the phases are shifted by $\pm 2n\pi$ after each period. This is equivalent to no shift at all. For a more detailed discussion see Appendix B in [13].

2.5 The influence of spontaneous emission

In the previous sections, the average ARP-force on a two-level atom was calculated, but in all those considerations the effect of spontaneous emission has been neglected. The complete picture, including spontaneous emission is given

by the Optical Bloch Equation (OBE) [7]. In order to determine the force, the OBE has to be solved and equation 2.10 applied, which is preferably done numerically [13]. The effect of spontaneous emission can be included for ARP in a simple form, because of the fact that $\omega_m \gg \gamma$ (rapid) and the resulting force can be calculated.

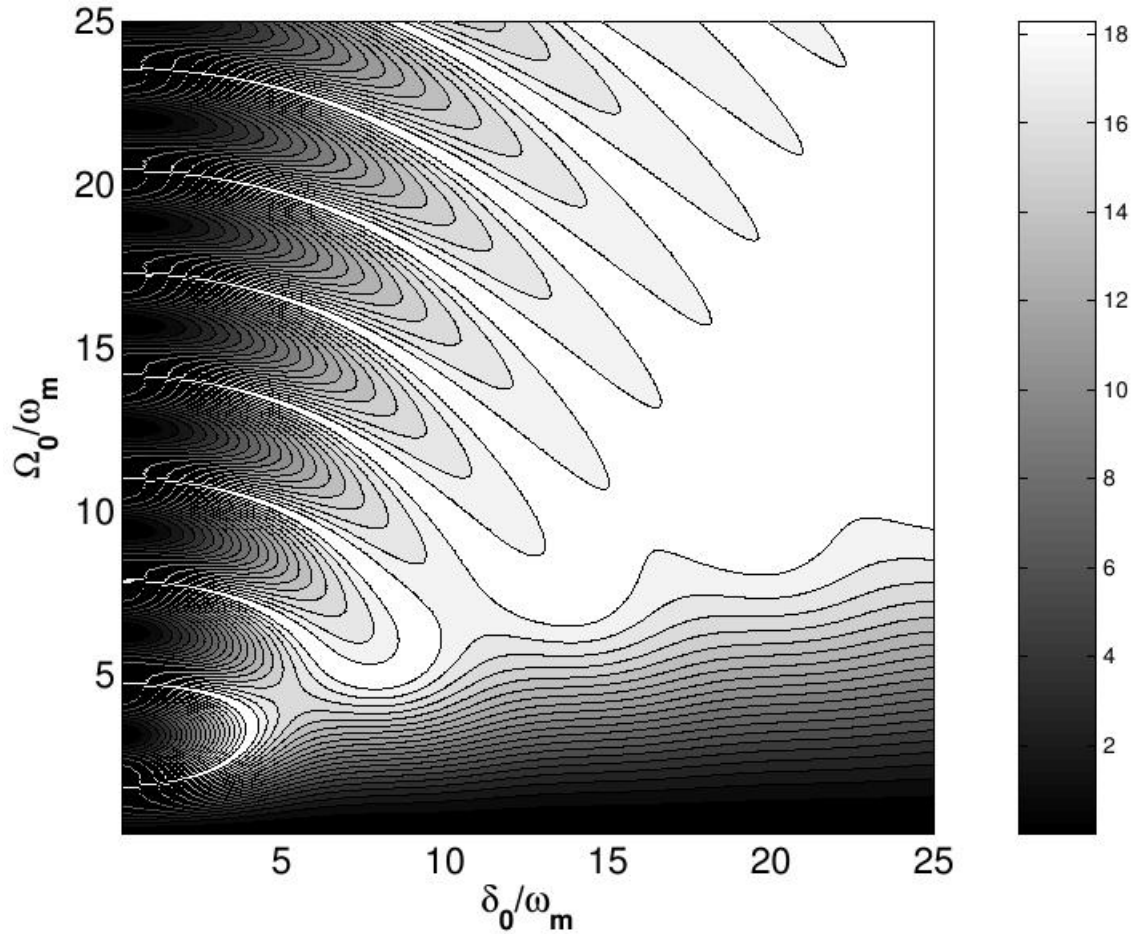


Figure 2.7 Force on rest atoms caused by sinusoidal light pulses. Spontaneous emission is included. $\omega_m = 100\gamma$. This force map is obtained from equation 2.17 with $\kappa = 0.6$. The force is plotted in units of F_{rad} [13].

The force including spontaneous emission can be written as

$$F_{\text{sp}} = \kappa \bar{F}. \quad (2.16)$$

Here $\kappa \approx \frac{1}{2}$, with the same argument as in section 1.7. But if calculations are done more carefully, it can be shown that κ is a more complicated function of the nonadiabatic transition probability P_{nad} . For small P_{nad} , κ is a little larger than $\frac{1}{2}$ and for large P_{nad} it is slightly smaller than $\frac{1}{2}$. Using equations 2.15 and 2.16 it yields

$$\boxed{F_{\text{sp}} = \kappa \frac{2\hbar k}{T} (1 - \sqrt{P_{\text{nad}}})} \quad (2.17)$$

where $T = 4T_p$.

There must be found a way now to compensate for spontaneous emission: As can be seen in figure 2.6, first continuous chirped pulse pairs from counterpropagating light beams are produced (a) and then a syncopation time between the cycles is introduced (b) in order to get a preferred direction of the optical force. Including spontaneous emission has the same consequence as in the picture of the bichromatic force when the counterpropagating π -pulses have been timed in an asymmetric way (see chapter 1.7). The optimal syncopation time is $T_n = 2T_p$. So the pulsing period $T = T_n + 2T_p = 4T_p$ is twice

the phase modulating period $2T_p$. Therefore the phase modulation frequency $\omega_{pm} = \omega_m$, whereas the amplitude modulation frequency $\omega_{am} = \frac{\omega_m}{2}$. The frequency corresponding to their common period $\omega_c = \frac{\omega_m}{2}$. In this experiment, the optimal syncopation time is used.

The optical forces on atoms at rest are calculated and plotted in figures 2.7 and 2.8 for sinusoidal light pulses sweeping at $\omega_m = 100\gamma$. Figure 2.7 is from equation 2.17 with $\kappa = 0.6$, while figure 2.8 is from the numerical integration of the OBE and the average of the force from equation 2.10 over time. They agree qualitatively.

Comparison of equation 2.17 with the result from the numerical integration of the OBE yields that the actual force on moving atoms is smaller than predicted in equation 2.17 for the case that P_{nad} is large. The reason for this is that an atom initially prepared in the ground state is more likely to be in the excited state during the syncopation time for large P_{nad} and therefore more susceptible to spontaneous emission. However, equation 2.17 can be used for the estimation of the velocity capture range of the optical force. For atoms at rest ($P_{nad} = 0$), the velocity capture range can be estimated as the velocity that shifts $P_{nad} = \frac{1}{4}$. The force therefore drops to half of the maximum value (see equation 2.15). It is known that for ARP $\Omega' = \sqrt{\Omega^2 + \delta^2} \gg \omega_m$ which is still true for the Doppler shifted torque vectors of moving atoms as long as

$\delta_0 - kv \gg \omega_m$. So, the velocity capture range (VCR) can roughly be estimated to be $\sim \frac{\delta_0}{16k}$, which is much larger than the ordinary VCR of the radiative force ($\frac{\gamma}{k}$). For other types of pulses the VCR can be estimated via the formula given in [13]. For π -pulses it is for instance about $\frac{\omega_m}{k}$, which is also narrower than the one for ARP.

The force and its VCR has been compared for different force schemes with the same period, which has been done by Dr. Xiyue Miao using a Fortran code that numerically integrates the OBE. The force profile for π -pulse, ARP and bichromatic schemes are plotted in figure 2.9 with the common sweeping frequency $\omega_m = 100\gamma$. The period of the field is $T = \frac{2\pi}{\omega_m/2} = \frac{4\pi}{\omega_m}$. Thus, the force of π -pulse and ARP sequences are about half of the value of the bichromatic force for atoms at rest. But the velocity capture range of π -pulse sequences is about double of that for bichromatic beams, whereas the capture range of ARP sequences is even wider than that. The capture range of the π -pulse is $\sim \omega_m$ and the one for ARP pulses $\sim \delta_0$. This means, that the wide capture range of ARP pulses enables large deflection of the atomic beam.

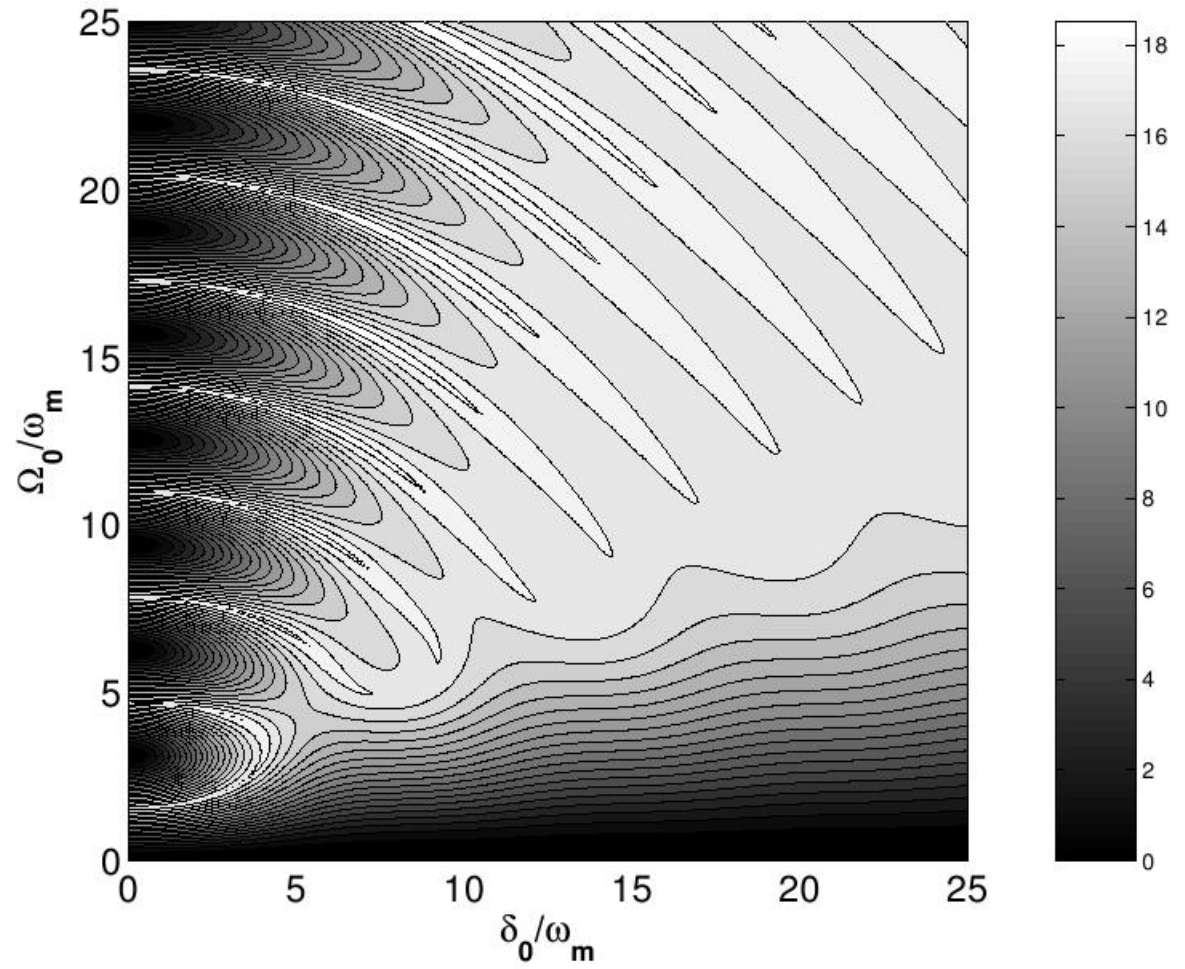


Figure 2.8 Force on rest atoms caused by sinusoidal light pulses. Spontaneous emission is included. $\omega_m = 100\gamma$. This force map is obtained from the solution of the OBE. The force is plotted in units of F_{rad} [13].

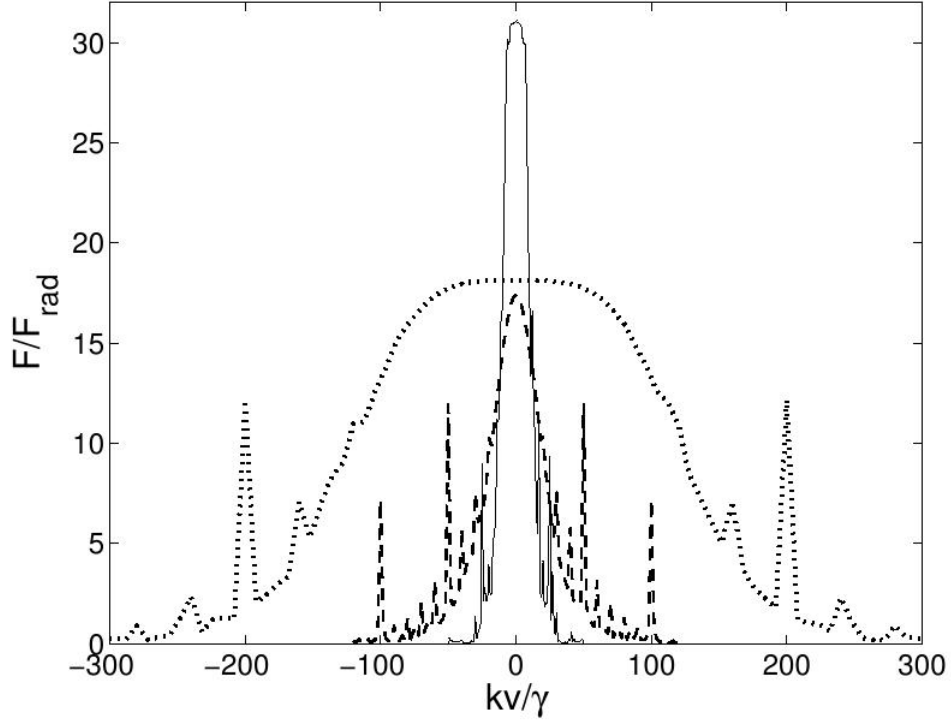


Figure 2.9 Comparison of the velocity dependence for various force schemes. Dashed curve: sinusoidal π -pulse beams with $\Omega_0 = \frac{\pi}{2} \omega_m$; dotted curve: sinusoidal ARP-pulses with $\delta_0 = 4.1 \omega_m$ and $\Omega_0 = 3.39 \omega_m$. The chirping frequency is $\omega_m = 100\gamma$. Syncopation time $T_n = 2T_p$ has been introduced in both schemes to produce the directional force so that $T = 4T_p = \frac{4\pi}{\omega_m}$. Solid curve: bichromatic laser beams of $\frac{\pi}{4}$ phase delay with detuning $\pm \frac{\omega_m}{2}$ and $\Omega = \frac{\sqrt{6}}{2} \omega_m$ for two frequencies [13].

Chapter 3

The Metastable Helium Apparatus

In this chapter the production of metastable Helium (He^*) using a glow discharge as well as the vacuum system where the experiments take place will be described. The vacuum system consists of a source chamber where the metastable Helium is produced and the beamchamber, which includes the interaction chamber, the detection chamber and the lithography chamber (figure 3.4). Apart from that, the production of the magnetic field with Helmholtz-coils as well as the detection using a Multi-channel-plate and Phosphor screen arrangement will be illustrated.

3.1 Metastable Helium

3.1.1 The Helium level diagram

In the experiment, metastable He^* atoms are used which are excited to the atomic energy level 2^3S_1 . The advantage of choosing Helium-atoms to work with is, that the He-scheme can be divided in two sub-schemes: Ortho- and Para-Helium. The Para-Helium contains all the singlet states of the system, while the Ortho-Helium scheme contains all the triplet states. Transitions between those two systems are forbidden in a nonrelativistic description because the selection rules say that $\Delta S = 0$ (total spin has to be preserved) and $\Delta L = \pm 1$, which is not satisfied here. Those effects result in a very long lifetime of the triplett-state 2^3S_1 ($t \sim 7900\text{s}$ [38]), which is much longer than the time scale that is relevant in the ARP-experiment ($\sim \text{few } \mu\text{s}$). This state is the metastable He-state (He^*) that is used as a ground state in this experiment. The lifetime is not infinite because of relativistic effects [37]. The level diagram is shown in figure 3.1.

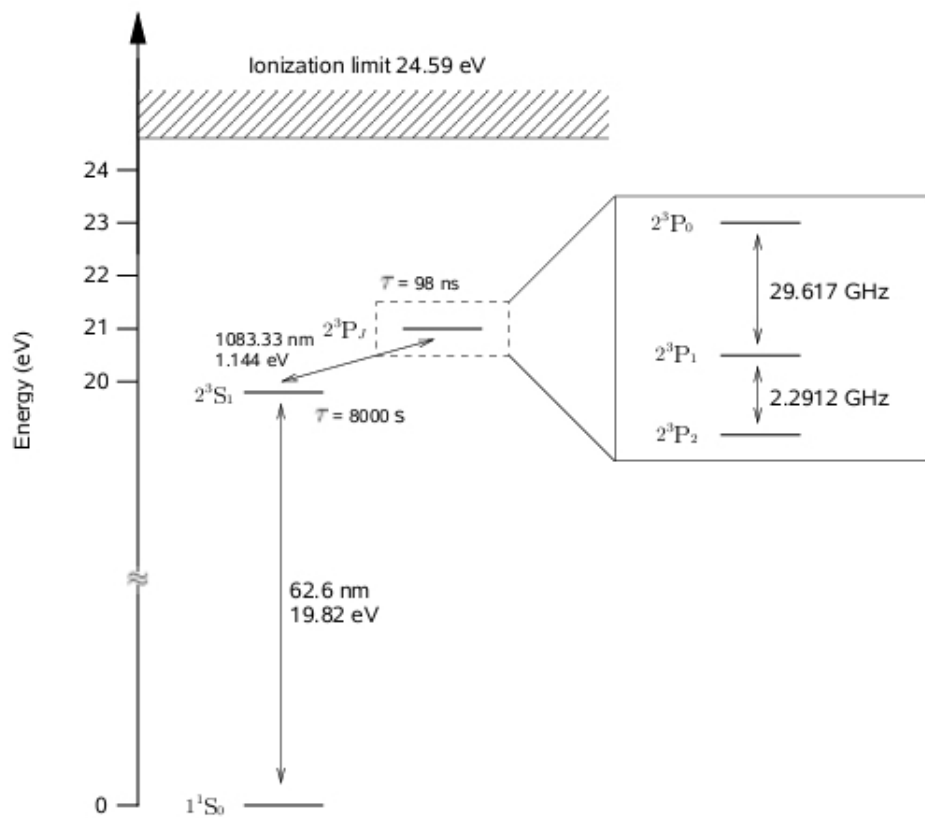


Figure 3.1 Selected energy levels of Helium. The effective ground state in this experiment is represented by the 2^3S_1 state due to its long life time. The state 2^3P_2 forms the excited state.

The energy level 2^3S_1 is used as the ground state of the two-level system ($|g\rangle$) because of the advantage of its very long lifetime. The state 2^3P_2 serves as the excited state ($|e\rangle$), whose lifetime is about 98 ns. It is obvious that this is not a real two level atom because of the magnetic Zeeman sublevels and therefore optical pumping is applied to make sure that indeed only two atomic energy levels are used (see section 1.5). The wavelength of the transition $2^3S_1 \rightarrow 2^3P_2$ is $\lambda = 1083.33$ nm. Therefore the diode lasers that are used in this experiment operate in the infrared regime. The two-level approximation can be used, since the spin of the nucleus for ^4He is 0 (magic number) and therefore no hyperfine structure exists. Another support for the use of the approximation is that the next closest energy level (which is 2^1P_1) is more than 2.29 GHz apart which is far more than any detuning from resonance that is used during the ARP-experiment.

Another characteristic of Helium is, that the metastable state of this noble gas has the highest internal energy known for atoms, which is 19.82 eV. This high energy corresponds to a wavelength of 62.6 nm. This wavelength is not yet accessible with lasers today, so the metastable state has to be produced in a DC discharge, which will be described in the following section. in table 3.1 some characteristic spectroscopic values for He are given.

Parameter	$2^3S_1 \rightarrow 2^3P_2$
Wavelength	1083.33 nm
Excited State Lifetime	98.04 ns
Transition Linewidth ($\frac{\gamma}{2\pi}$)	1.62 MHz
Saturation Intensity ($I_s = \pi\hbar c/3\lambda^3\tau$)	$0.167 \frac{\text{mW}}{\text{cm}^2}$
Capture Velocity ($v_c = \frac{\gamma}{k}$)	$1.76 \frac{\text{m}}{\text{s}}$
Recoil Frequency ($\omega_r/2\pi$)	42.46 kHz
Doppler Velocity ($v_D = \sqrt{\hbar\gamma/2M}$)	$28.44 \frac{\text{cm}}{\text{s}}$
Recoil Velocity ($v_r = \hbar k/M$)	$9.2 \frac{\text{cm}}{\text{s}}$

Table 3.1 Spectroscopic Data for He* transitions [38].

3.1.2 Production of metastable He

The He*-source that is used here is based on the "reverse flow" design that was invented by Kawanaka et al [36]. In order to produce cooler Helium beams, modification has been made by a group at the University of Utrecht in the Netherlands, where the source was originally built. As said in the previous section, it is not possible to produce metastable He-atoms via optical excitation. Instead, the atoms are excited by a DC glow discharge (figure 3.2). The source basically consists of a 1cm diameter pyrex glass tube with a constricted end. In the interior there is a tungsten needle with a diameter of 1mm that is surrounded by a metal rod and attached to its end, while the tip

of the needle points to the tapered end of the glass tube. It is kept centered by ceramic spacers. Around the tube there is a chamber for liquid nitrogen LN₂, that can be filled from the outside through a stainless steel coaxial jacket. The glass tube is held in place using some teflon spacers.

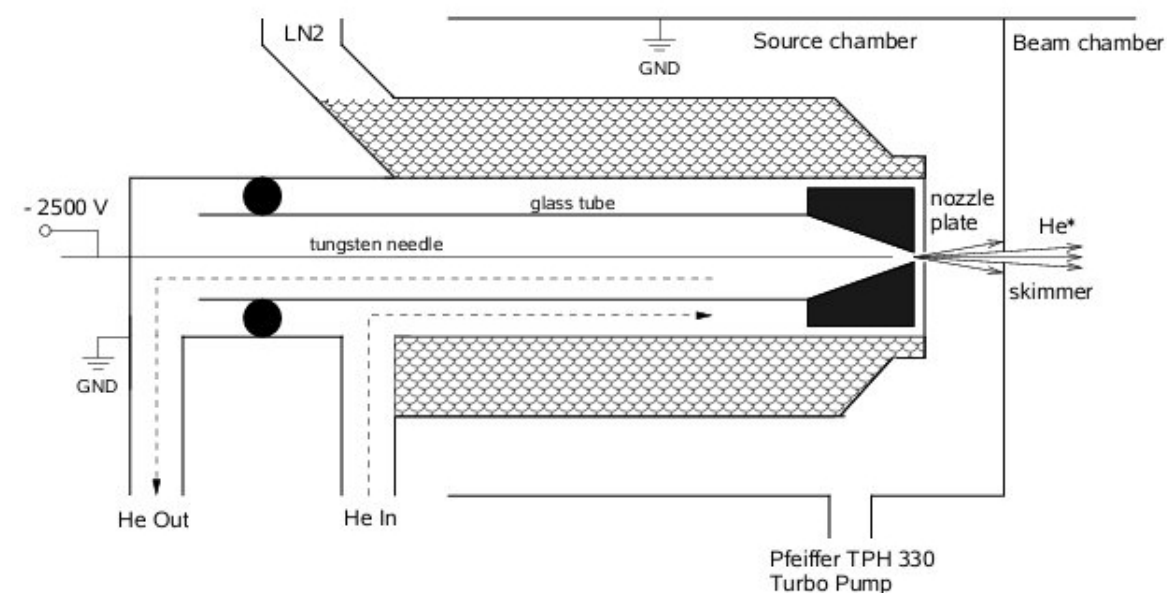


Figure 3.2 Cross section of the DC discharge source for the production of metastable Helium. Note that the ceramic spacer on the tungsten needle is not shown.

There is Helium flowing from the outside of the glass tube towards its narrowed end through the gap between the glass tube and the jacket that is filled with liquid nitrogen ($T = 77\text{ K}$), so that it is cooled before it goes into the tapered end of the glass tube. The cooling of the Helium gas helps to reduce the velocity of the atoms that are leaving the source. Gas flow is allowed

though some channels that are cut into the spacers that are used for keeping the needle centered inside the glass tube. The anode for the discharge source is the so called nozzle plate, which is a grounded aluminum plate with 0.5 mm aperture that is located at the front end of the cooling jacket. The needle can be extended and retracted by means of a vacuum motion feedthrough. Most of the gas is pumped backwards through the inside of the glass tube by a mechanical pump (Welch Duo Seal, Model 1402). The He-atoms which are not pumped back sustain a glow discharge between the sharpened tip of the tungsten needle and the nozzle plate, when a negative high voltage is applied to the needle (2000V – 2500V) through a 170 k Ω high power resistor (2 W). There is He* produced with this discharge via electron impact or ion-electron recombination, but most of the He* is almost immediately quenched by collision. The only atoms that survive are basically the He*-atoms that are produced outside the plasma in the dilute afterglow of the discharge directly behind and past the nozzle plate [36, 39]. Since the particle density in the beamline is lower, it is most likely that those atoms fly to the interaction region and can be detected later. This means that the He*-production is quite low ($\approx 10^{-5} - 10^{-4}$ [7]). Other kinds of short lived excited states are also produced in the glow discharge, e.g 2^1P_1 , which decay quickly to the ground state, emitting light with an energy of about 20 eV (similar to the energy

of He^{*}). Apart from that, there are other components in the beam as well, such as free electrons, ions, visible light and mainly ground state He-atoms. The charged particles in this assembly can be removed by using deflections plates that have actually been built for use in the lithography experiment. However, since these charged particles have no significant influence on the ARP-experiment because a slit geometrically defines a narrow He^{*}-beam, the deflection plates were not used. Directly after the nozzle plate is another plate (called skimmer) that geometrically defines the He^{*} beam and that also allows differential pumping between the source chamber (in front of the skimmer) and the He^{*} beam chamber (behind the skimmer) (figure 3.4).

The reliable production of a discharge and a subsequent metastable beam is very sensitive to many conditions. This includes the shape and the cleanliness of the glass tube, the sharpness of the tungsten needle and the quality of the anode surface. When the source does not work properly, it is really important to check if there is some dirt inside the glass tube. Other important parameters are the pressure in the discharge region and the voltage on the discharge needle. Stable running of the discharge is accomplished starting at a current of 2 mA. When the current is turned up the discharge becomes "hotter" and therefore the average velocity of the He-atoms increases. A trade-off between beam velocity and He-production is needed, since fast atoms have

less interaction time with the laser beams (see description of the experiment). The pressure in the discharge region relies on the pressure of gas entering the source and the speed at which it is pumped out, but it can not be measured properly. The inlet pressure can be adjusted with a fine needle valve and is measured by a Granville-Phillips Convectron Gauge placed in the Helium gas inlet. The reading of the gauge is done by a Terranova Model 926 Scientific Gauge Controller, which is typically calibrated for nitrogen (air), but a conversion chart for other gases had been acquired from Duniway Stockroom. The inlet He-pressure has a typical value of 5-10 Torr. Another Granville-Phillips Convectron Gauge is used at the outlet and indicates a pressure of about 1.2 Torr. When the system is run at lower pressure, the metastable He production rate is higher, but also the discharge is caused to become unstable. However, with optimal operation conditions, the source runs stable for long periods of time (several hours) without significant change in the properties of the He* beam. The output flux is about 10^{14} atoms/s-sr [40, 41]. The values used in this experiment were typically 2500 V for the discharge voltage and 6 mA for the discharge current. Monitoring the current and watching the color, intensity and shape of the discharge glow, which can be easily done through a small viewport, ensures that metastable He* is produced in a reliable fashion.

The He-beam after the skimmer in the He*-beam chamber has been charac-

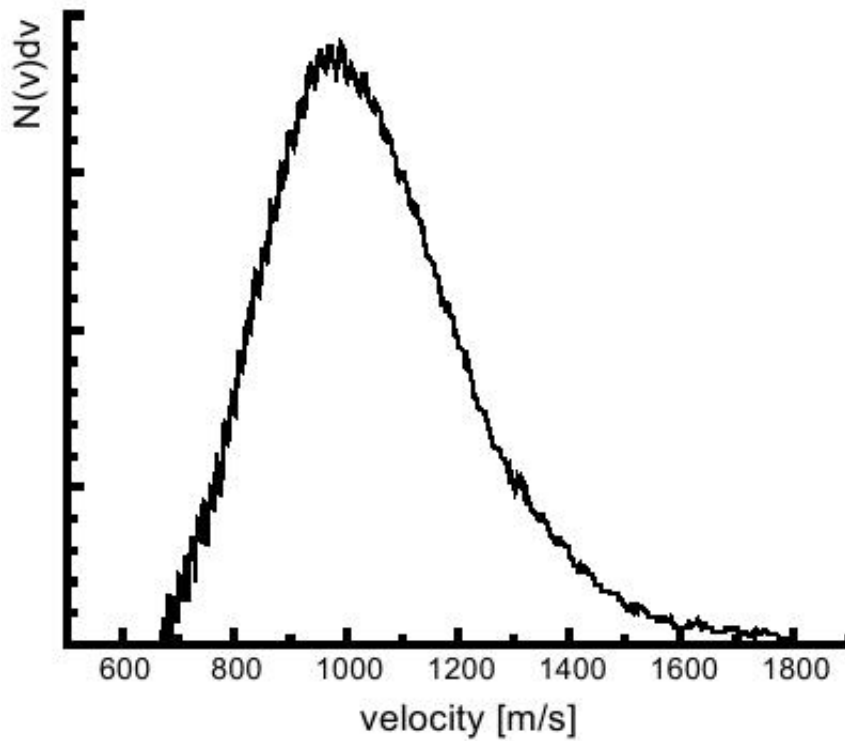


Figure 3.3 Longitudinal velocity distribution of metastable He-atoms with a discharge current of 6 mA as measured in [41].

terized by Matt Cashen [41], where the longitudinal velocity was characterized by a time of flight measurement (TOF). For this purpose the beam had been pulsed with a mechanical chopper. For atoms moving with a given velocity, the signal intensity versus the arrival time was detected and amplified with a MCP (Multi Channel Plate). This is a good technique to separate the atomic signal from the UV signal, which provides a zero point for time. The results of those measurements turned out to be highly repeatable. The results show, that the He*-atom velocity is peaked at about $1000 \frac{\text{m}}{\text{s}}$ with a FWHM of about

$400 \frac{\text{m}}{\text{s}}$ (figure 3.3).

3.1.3 The Helium Beamline

The beamline of metastable He* consists of four sections: The source chamber, the interaction chamber, the detection chamber and the lithography chamber, where the last three all together are called the beam chamber. The main beamline is built of stainless steel with copper sealed ConFlat™ flanges with a diameter of 10.16 cm. Only the seals that connect the gas flow and the vibration isolators (for attaching the turbo pumps to the system) are not ConFlat. The roughing pumps and the Helium inlet and outlet of the source are connected using Kwik-Flange™ components. It would actually be possible to provide an ultra high vacuum (UHV) in the beamline. But since there are some components inside the system that are not especially designed for use in vacuum (\rightarrow outgasing), only high vacuum (HV) is achievable. Apart from that, the system is opened quite frequently to change or modify the arrangements inside, so practically there is just HV. The total length of the beamline is about 80 cm. A drawing of the system can be seen in figure 3.4.

Both chambers, the source chamber and the beam chamber, are each individually pumped by a reliably working Pfeiffer model TPH 330 turbomolecular pump, which is backed by a mechanical pump. Since the two chambers are sep-

arated by the skimmer plate with a 0.5 mm aperture, they can be maintained at different pressure while the source is running. The advantage of that is, that the pressure can be higher in the source chamber, because a higher pressure assures a stable running of the discharge source. The pressure in the beam chamber has to be low, so that collisions between atoms of the metastable beam and background gas are reduced in order to minimize collision induced decay of the He*-atoms (Penning ionization [42]). Between the nozzle plate and the skimmer, the pressure has a value of about 10^{-4} Torr, while it is at a few $\times 10^{-6}$ Torr behind the skimmer. The pressures are measured by two Kurt J. Lesker model G100F ion gauges. The nozzle plate and the skimmer are typically separated by about 0.5 to 1.0 cm. This distance and their mutual alignment can be adjusted via a bellows which connects the source to the source chamber.

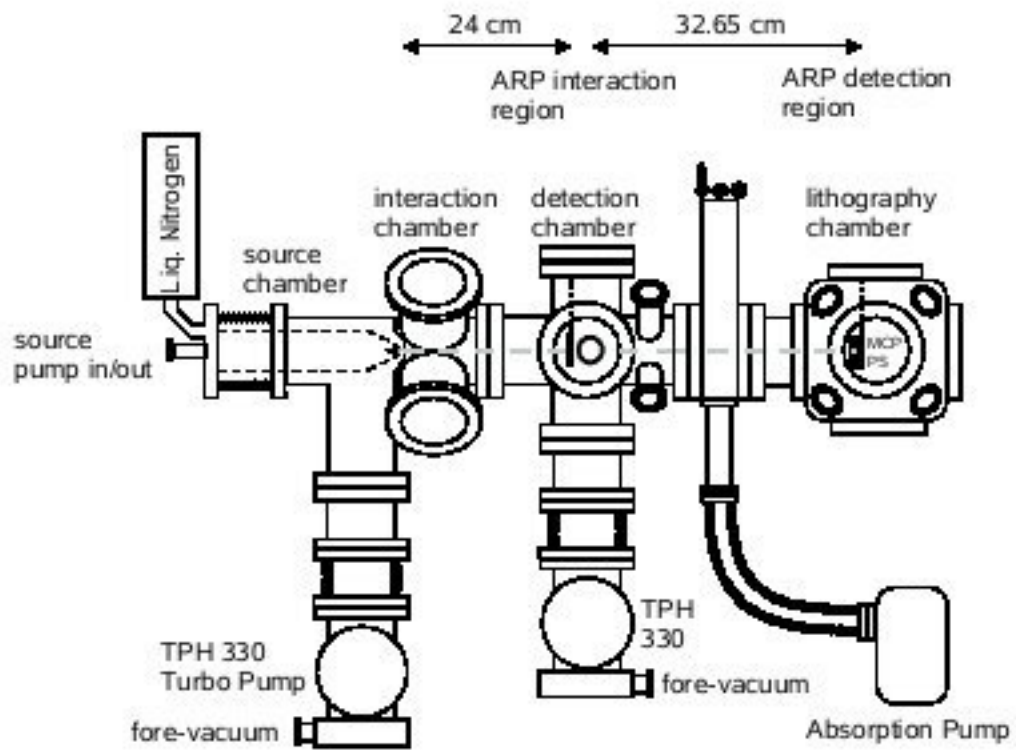


Figure 3.4 Schematic of the vacuum system viewed from the side. The names of the chambers correspond to the lithography experiment.

The interaction chamber is a six-way-across that is directly welded onto the Tee of the source chamber so that the source and skimmer protruded into an area with considerable optical access. The Tee and the six-way-across have an outer diameter of 10.16 cm. The source chamber turbomolecular pump is connected to that port of the Tee, that faces downwards. Flanged glass viewports are mounted on the four ports for the optical access of the bichromatic laser beam for the lithography experiment. The advantage of this setup is, that the bichromatic collimation beam can be applied very close to the skimmer plate and therefore enables efficient collimation of the atomic beam before it expands too far. The diameter of the glass windows is again 10.16 cm. They are anti-reflected coated for 1083 nm and for 389 nm ($3^3P_J \rightarrow 2^3S_1$, which can also be produced in the lab). On the top of the vacuum chamber, up against the six-way-across on the source side, there is a tube with a small window to allow viewing the afterglow of the discharge between nozzle plate and skimmer. This is an easy way to check if the source is working or not.

The next section in the metastable He*-beamline is the detection chamber for bichromatic collimation [38]. It consists of another six-way-across, but its arms are rotated 45° relative to the interaction chamber, so that the other two axes of the six-way-across are at the horizontal and the vertical plane. A Multichannel Plate/Phosphor Screen (MCP/PS) detector assembly is mounted on

the top port with a linear motion feedthrough for the detection of the collimated beam. The bottom port is connected to the other turbomolecular pump (the one for the beam chamber). The turbo pumps are attached to the system through vibration isolators. Each side port also has a glass viewport for optical access, which are anti-reflected coated for 1083 nm light. Behind the detection chamber, there is a ThermionicsTM PFG-TLG-4000H/R gate valve. At the very end of the beamline there is a Kimball physicsTM 11.43 cm Multi-CF spherical cube (MCF450-SC60008-A). This last section is designed for doing atomic lithography. There used to be a Thermionics VLS-600/N shutter between the detection chamber and the Thermionics PFG-TLG-4000H/R gate valve, but the shutter has been removed since it was used in previous experiments and had no use any more. Now the beamline is ~ 17.4 cm shorter than before which results in a brighter signal on the phosphor screen. The gate valve can be used to separate the spherical cube from the rest of the vacuum system. Since a roughing line was connected from the bottom of the gate valve to an absorption pump, it is possible to pump down the lithography chamber before opening the gate valve. So changes in the Lithography chamber (which is the ARP detection region) do not take as much time as when the whole system had to be pumped down every time.

Since the experimental setup, especially the vacuum system, is used for the

ARP-Experiment as well as for the lithography experiment, it was necessary to be careful that those two experiments do not interfere. The collimation procedure in the bichromatic collimation experiment is quite complicated and can be very time consuming. Therefore one motivation to study the ARP-force is to make use of it for He* beam collimation, since it is more robust than the bichromatic force.

Helmholtz-coils are used in order to produce the magnetic field that is necessary to optically pump the He*-atoms (see chapter 1.5). In addition to that a vertical slit is required to geometrically define the atomic beam (see chapter 3.2 for further information about the setup). The final idea was to mount the slit on the same rod as the Helmholtz-coils and mount it to a linear motion feedthrough in the detection chamber. The MCP/PS assembly for the lithography experiment was mounted to another feedthrough so that both systems can be moved up or down independently, depending on what experiment is running. The vertical slit has a diameter of about 250 μm and a length of 1 cm. The distance between the skimmer plate and the slit is about 24 cm. The interaction region for the ARP-experiment is about 3 cm behind the slit. The ARP beam and the Optical Pumping beam are accessed via the big windows of the detection chamber. Note that the *ARP-interaction* takes place in the (lithography) *detection* chamber. This has to be done, since

the force is so large that the atoms would most probably be pushed off the detector, if the ARP-interaction also took place in the lithography interaction chamber. A shorter distance from interaction to detection region makes sure that all deflected atoms are detected. In order to detect the ARP force, another MCP/PS detector assembly is inserted through the flange of the spherical cube with a 5 cm linear motion feedthrough (Huntington L-2211-2). The MCP/PS detector is about 32.65 cm downstream of the interaction region of the ARP beam. It can be moved in and out of the way of the He* beam by using the motion feedthrough.

3.1.4 The MCP/PS Detector

It is known that a He* atom carries an energy of 19.82 eV which can be released via collision, for instance when the atom hits a metallic surface where the ejection of an electron results. This effect can be used for the detection of the He* atoms. In the experiment that is described in this thesis, the atoms get deflected by the ARP-force. An MCP/PS detector was used to map the distribution of the He* 32.65 cm behind the interaction region. This kind of detector is a useful tool for analyzing the atomic beam since it can produce a real time cross sectional imaging of an atomic distribution.

The MCP is basically a thin disc of lead glass comprising of many channels

that are parallel to each other and perpendicular to the surface of the disc (figure 3.5). These channels (diameter $\sim 10\ \mu\text{m}$) form a hexagonal lattice with lattice spacings of $12\ \mu\text{m}$. Each He^* -atom that hits the surface of a channel produces an electron. Electron multiplication occurs due to a negative bias voltage across the two surfaces of the MCP that accelerates the electron into the channel. The MCP's in this experiment are purchased from BURLETM. These MCP's have an active area of 25 mm diameter and the multiplication factor is up to $\sim 10^3$ for $-1000\ \text{V}$ bias voltage. The MCP is usually used at a voltage of -500V to -800V . For the detection of the electrons, a phosphor screen was placed directly behind the MCP. It consists of a glass plate that is 3.81 cm in diameter. On this glass plate there is a thin layer of gold coating evaporated which serves for conductivity. On top of the gold coating, a layer of P20 phosphor particles is deposited. The diameter of the phosphor-layer is about 3.18 cm. When a high voltage is applied on the gold layer, the electrons are accelerated from the MCP to the PS. The high voltage has a value of $+2000\ \text{V}$. Electrons that impact on the PS, cause the phosphor to fluoresce with visible light, where the brightness on a certain spot depends on the electron density and therefore on the number of He^* atoms hitting the MCP at that spot.

In this way, an image on the phosphor screen was produced and could be

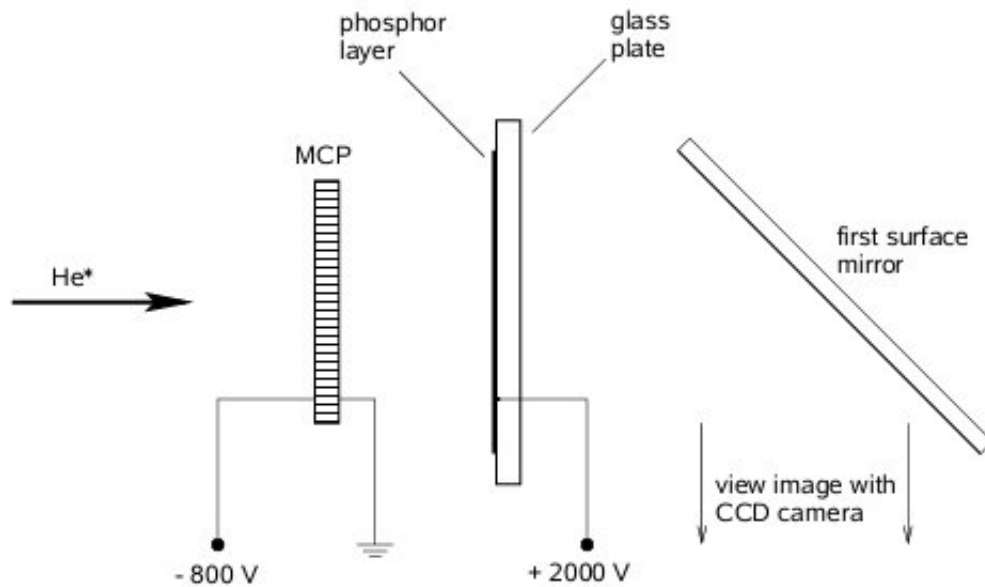


Figure 3.5 Picture of the MCP/PS detector system for the detection of the original and the deflected He^+ -beam. The mirror that is mounted in a 45 angle to the beamline is used to reflect the image through the side window of the vacuum chamber, so that it can be viewed with a CCD camera without interfering with atomic lithography at the end of the beam.

viewed from a side window of the lithography chamber by a CCD camera. In order to actually view the image through the side window, a 35 mm \times 50 mm front surface mirror mounted at 45° to the MCP/PS arrangement was used. This mirror, which is glued on a piece of sheet metal, is mounted together with the MCP/PS detector with Kimball PhysicsTM standard eV parts. The whole assembly is mounted to a linear motion feedthrough which fits through the top flange of the spherical cube. So it can be moved out of the way for atomic lithography. The images of the camera are caught and saved on a

computer (bmp-files) using a TV tuner card (AVerMedia TV98). The analysis of the images is done with ImageJ, a freeware Java application developed at the National Institutes of Health and the data analysis is done using a self written C++ Code.

Even though, the MCP/PS has a lot of advantages, it is necessary to mention that it also has some limitations. A calibration of the correlation between atom flux and image pixel value is missing. In addition to that, the electron ejection efficiency of a He* atom from the surface of the MCP is not exactly known. Also the sensitivity of the combination of the MCP and the PS to atomic flux is highly non-linear and non-uniform. The latter is mainly due to the aging of the PS under high flux impact, which makes quantitative measurements with the MCP/PS detector really difficult.

Another problem was the fact that the phosphor screen got burnt at the spot, where the slit was imaged (figure 6.4). This caused a lot of difficulties, because this phosphor screen was also used in the lithography experiment. Therefore, the screen has been changed and a block has been built, which can be moved before the MCP/PS arrangement to block the main He*-beam during the measurements. This prevents the screen from being burned too hard.

3.2 Production of the magnetic field

As discussed in chapter 1, it is necessary to have a magnetic field in order to be able to optically pump the He*-atoms. So the first part of the work for this thesis was to develop different designs and perform simulations with a Mathematica code whose main part was taken from [25] and which was modified for the purposes of the ARP-experiment. The result of the simulations was, that the most practicable way of producing a proper magnetic field, was the use of small Helmholtz coils inside the vacuum system. The advantage of those small Helmholtz-coils is, that big ones outside the vacuum system would have caused a lot of practical trouble since everything is full of different kinds of optics there and also the access to the vacuum system would have been made a lot more difficult. So the small coils are a good choice and have been built. The sides of the coil holder, which is build out of MACORTM have been made flat because otherwise the assembly would not fit inside the vacuum system since space is extremely limited there. Calculations show, that a field of a few Gauss ($1\text{G} = 10^{-4}\text{ T}$) is sufficient, so the Helmholtz-coils were designed as shown in figures 3.6, 3.7 and 3.8. The average coil radius turned out to be $R \approx 2.29\text{ cm}$, with $n = 18$ turns on each side. In order to get the field finally working, many things had to be taken into account, e.g. that the current is not too high for the wires and the vacuum compatibility of all the materials

that are used for the coils. It turned out that the best choice are copper wires with a CAPTON™ insulation.

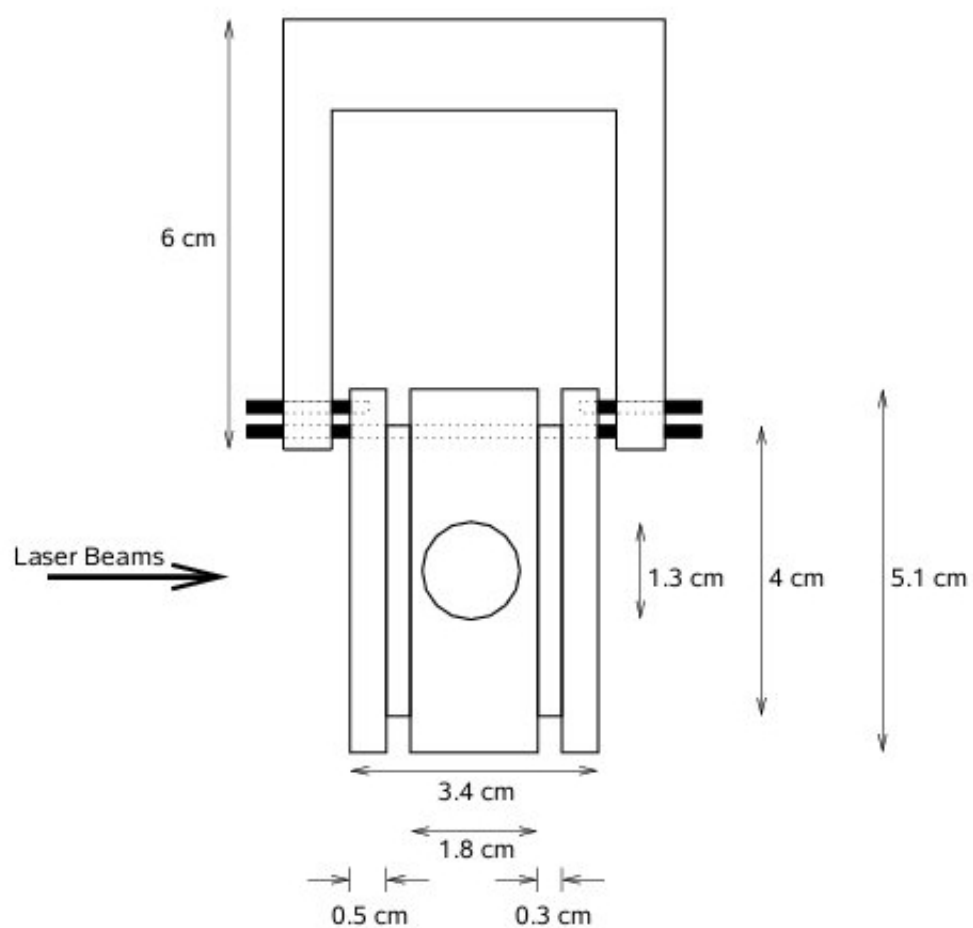


Figure 3.6 Frontview of the Helmholtz-coils with mount (perspective of the atomic beam). The hole in the middle is for the atomic beam and the laser beams (ARP and OP) are perpendicular to it. The slit for the atomic beam is not shown here. Sizes are given in cm.

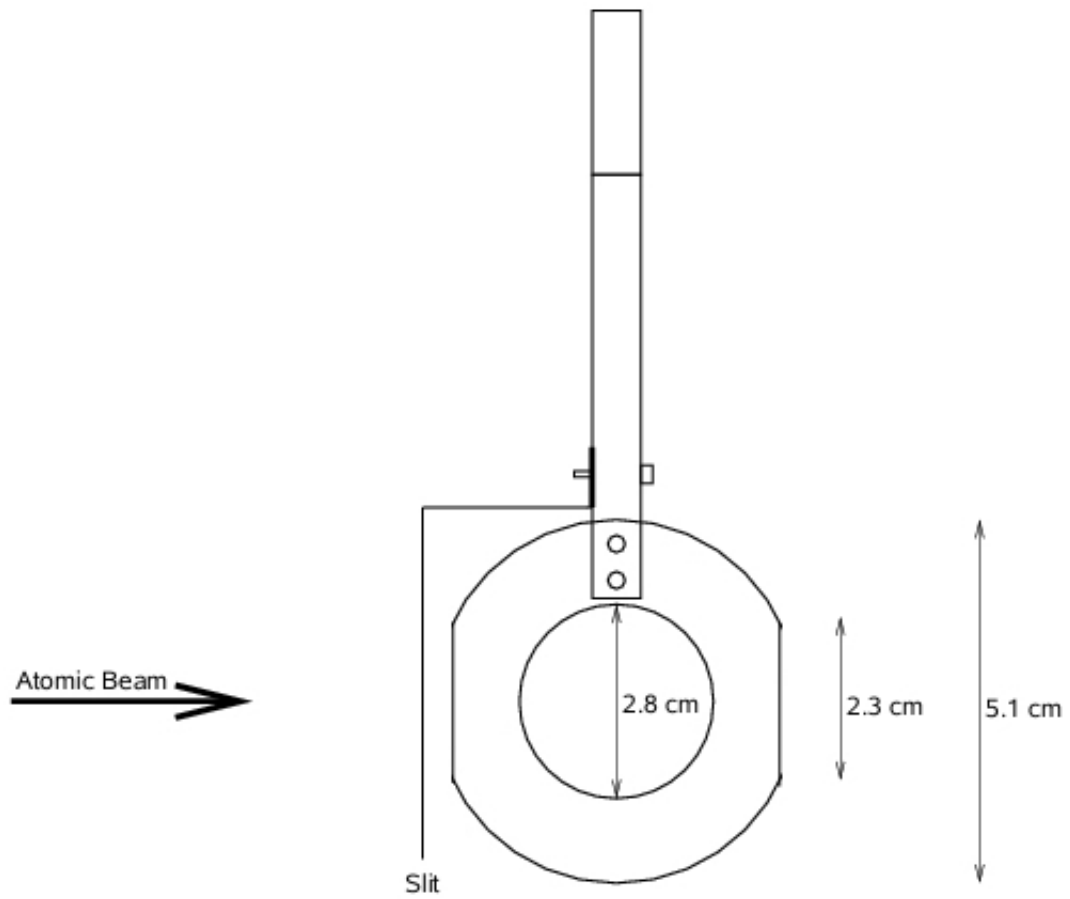


Figure 3.7 Sideview of the Helmholtz-coils including mount and slit for the atomic beam (perspective of the laser beams). All measures are given in cm.

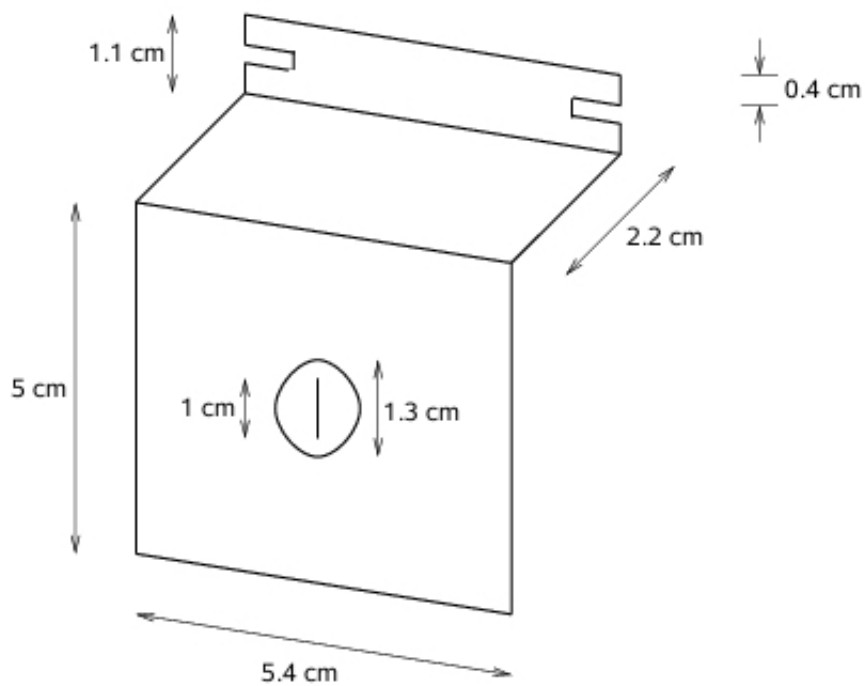


Figure 3.8 Schematic of the slit for the atomic beam. A thin metal foil is glued on an aluminum piece and a slit is cut into the foil. The length of the slit is 1 cm and its width is $250 \mu\text{m}$.

Chapter 4

Production of the ARP-light

In this chapter the heart of the experiment will be described: The production of the ARP-pulse sequence. First of all, the laser light with a wavelength of 1083 nm (wavelength of the transition $2^3S_1 \rightarrow 2^3P_2$ in metastable Helium) is provided by a Spectra Diode Labs diode laser. The production of the chirped pulse is done by first modulating the frequency and then modulating the amplitude of the light with two LiNbO₃-based integrated optical modulators. The analysis of the spectrum is done with two homemade Fabry-Perot spectrometers and for the measurement of the pulse profile of the chirped pulse, a InGaAs photo detector is used. Since a high optical power is needed in order to do the ARP-experiment, the light is sent through two Ytterbium-doped fiber optical amplifiers. Also the laser light for the optical pumping beam is sent through one of these fiber amplifiers in order to get enough power for the

pumping process. At the end of this chapter, the optics that are used to direct the beams to the interaction region will be described.

4.1 The Diode Laser

The diode laser that is used for this experiment is a Spectra Diode Labs SDL-6702-H1 Distributed Bragg reflector laser. The advantages of that kind of laser are its high performance and low costs and therefore it is widely used in atomic and molecular physics. In addition to that, a DBR laser involves a Bragg grating fabricated into the active region of the laser diode, which serves as an *internal* wavelength selective element of the laser and also improves the frequency tunability and the long-term frequency stability which is important (not only) for the ARP-experiment. In this lab, two laser systems of the type SDL-6702-H1 are used, one for the bichromatic collimation of the He* beam in the lithography experiment and the other one in the ARP-experiment and for optical pumping. The frequency control and stabilization were investigated by C. Avila [43] and they were put to use by M. Cashen [41].

The SDL-6702-H1 laser comes in a standard 8-pin TO-3 window package with a thermistor and a thermoelectric cooler included. For operating the laser, a Newport model 325 temperature controller is used for temperature stabilization and for the injection current supply a Newport 505 current con-

troller was bought. By applying a low-level signal to the controller, the current can be modulated up to 500 kHz, which has been done for a better lock of the laser frequency.

4.1.1 Laser Frequency Tuning

For experiments in atomic or molecular physics it is an essential task to control and stabilize the laser frequency properly. There are three possibilities to control the laser frequency of diode lasers. The coarse control can be done via adjusting the temperature and the fine control by adjusting its injection current. An even finer control and also frequency narrowing can be achieved by offering optical feedback to the laser [44]. The frequency tuning coefficients of the DBR laser via temperature and injection current have been measured to be $-22 \text{ GHz}/^\circ\text{C}$ and $-300 \text{ MHz}/\text{mA}$ [43]. Here, the thermistor was set to $9.75 \text{ k}\Omega$, which corresponds to a temperature that is a bit lower than room temperature ($\sim 25^\circ\text{C}$). The injection current was set to roughly 140 mA. This was done, so that the laser frequency is satisfactory put to the He^* atomic transition at $\lambda = 1083\text{nm}$ with a power output level of $\sim 25 \text{ mW}$. In order to realize the optical feedback, an "extended cavity" (EC) is used for the laser system [45]. The EC is formed between the back Bragg reflector of the DBR diode and an external high reflectivity mirror with $> 99\%$ reflectivity in an

angled configuration. A 30/70 beamsplitter was used to complete the EC and also served as the output coupler. A piezo electric transducer (PZT) driven by a home made, high voltage controller is attached to the external mirror for adjusting the EC length and therefore ramping the laser frequency. For a schematic of the extended cavity system, see figure 4.1.

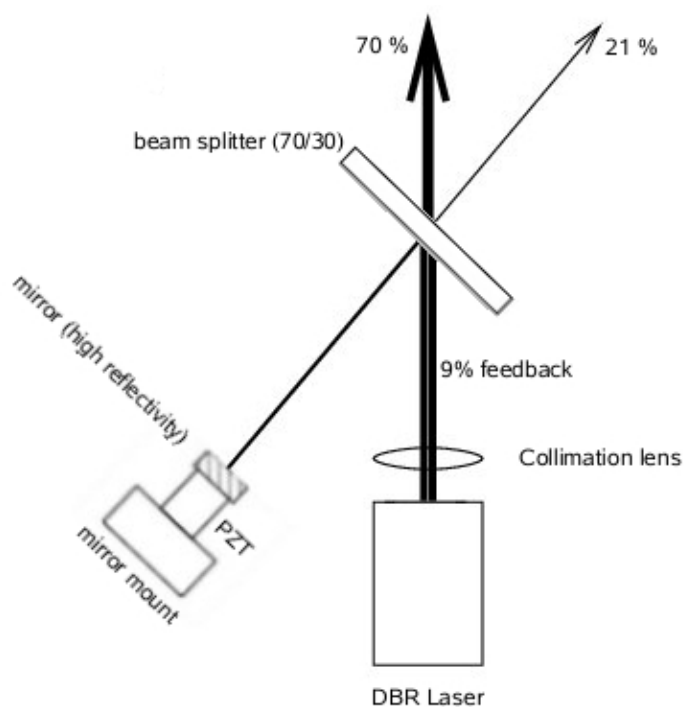


Figure 4.1 The light that leaves a diode laser is first collimated by a collimation lens and then split by a 70/30 beamsplitter. The 70% of the beam are sent to the modulators and are finally used for the experiment. The 30% light is retroreflected by a high reflectivity mirror ($>99\%$) and split again at the beam splitter, where 9% of the light is used as an optical feedback for the laser and the remaining 21% is used for optical pumping, wavelength analysis and SAS (after amplification).

Unfortunately, the EC laser is disturbed by environmental conditions, such as mechanical vibrations, air flows and temperature drifts. Therefore, the laser and EC components are rigidly mounted on a solid 305 mm \times 710 mm \times 76 mm slab of aluminum. The whole assembly is arranged in a box that is made of 51 mm thick Owens-Corning polystyrene foam. All of this is done to help to stabilize the laser frequency to the order of a few MHz. In addition to providing fine tuning of the laser frequency, the EC configuration helps to narrow the linewidth of the laser [44, 45] where the linewidth reduction was previously measured to be 125 kHz [13]. So the new linewidth is 20 times smaller than the 3 MHz free running laser linewidth and also smaller by an order of magnitude than the natural linewidth (which is 1.6 MHz) of the used He* transition ($2^3S_1 \rightarrow 2^3P_2$) [41].

4.1.2 The locking of the laser frequency

However, all these efforts are not yet enough to reduce frequency fluctuations and long term drifts of the laser frequency. For this purpose, a doppler free, Saturated Absorption Spectroscopy (SAS) signal is used to lock the laser frequency to the used atomic transition [46]. As can be seen in figure 4.2, the main part of the 21% leakage beam is sent to the 4W Fiber Amplifier. After amplifying the signal, the beam is split and the main part is sent to the inter-

action region as the optical pumping beam, while the minor part is sent back in order to produce the SAS signal that is used for further stabilization of the laser frequency. The light arrives at a thick uncoated glass plate and is partly reflected at each surface of the plate ($\sim 4\%$). This produces two weak parallel beams of which one is called the probe beam and the other one the reference beam. After that, the two beams travel through a He discharge cell and a 50/50 beamsplitter before they see two photodiodes that lead to a subtractor.

The beam that is not reflected at the thick glass plate, but passes through it, is stronger than the reflected beams and is later reflected from the 50/50 beamsplitter in order to counterpropagate against the probe beam through the cell. This beam is called the pump. The absorption signal of the reference beam is the usual Doppler broadened peak, but the probe absorption peak is diminished at resonance since the stronger pump beam, which has opposite Doppler tunings, interacts with atoms of the same velocity group and saturates the transition. Thus, the resulting signal is the Doppler-free Lamb dip.

The goal of this elegant setup is to get the Doppler-free absorption signal for laser frequency locking. This is being done, by subtracting the absorption signal of the probe from that of the reference. Then, the SAS signal is sent to a lock-in amplifier (Princeton Advanced Research model 126) that generates an error signal as a feedback to the laser. The signal is first sent to a SRS

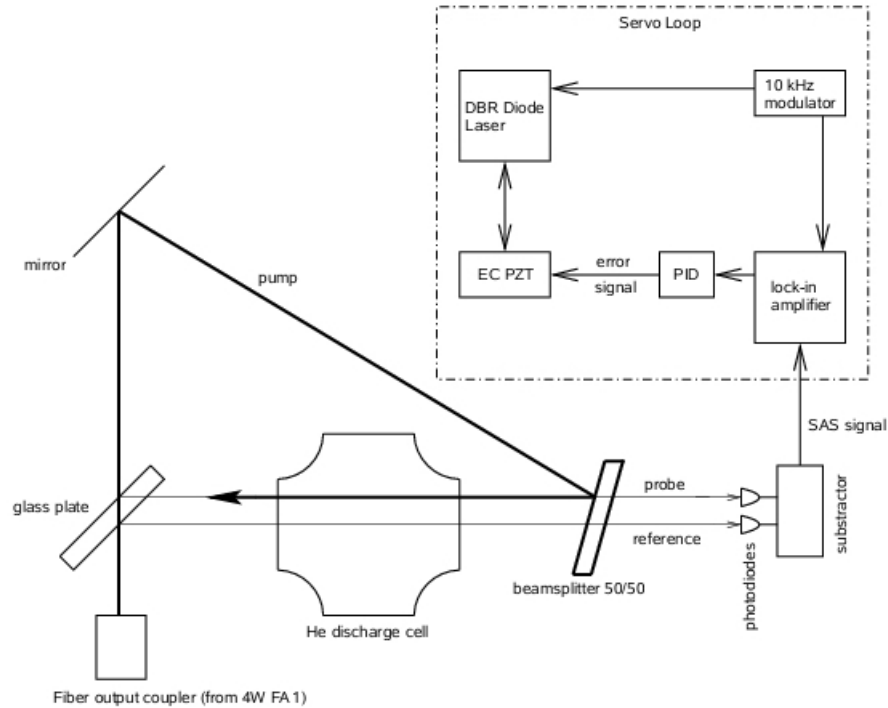


Figure 4.2 The Saturated Absorption Spectroscopy is used to lock the laser frequency reliably on the transition frequency of $2^3S_1 \rightarrow 2^3P_2$. In the lower part of the picture it is shown how the SAS-Signal is derived from the part of the Optical Pumping beam that was split behind the 4W FA. The Servo Loop in the dashed box shows how the SAS signal is used to produce electronic feedback to the laser for frequency stabilization.

PID-controller, which is used to prevent the laser from long term frequency drifts. With the PID-controller, the laser could be kept stable up to more than two hours. After that, the error signal is sent to the laser as a feedback. For the settings of the parameters of the PID-box, see table 4.1. For explanations of the PID-controller, see [38]. An oscillator that is located inside the lock-in amplifier produces a 10 kHz sinusoidal signal, which is then applied to the

Parameter	Value
P (gain)	-1.5
$I = \frac{1}{T_i}$	$80 \frac{1}{s}$
$D = T_D$	$5 \cdot 10^{-4} s$
Internal setpoint	0 V
Offset	0 V

Table 4.1 Settings of the PID-controller for the laser locking.

modulation input of the laser current controller and also used as a reference signal for the lock-in itself. This makes sense because the modulated SAS signal is mixed with the reference signal in the lock-in amplifier and this results in a derivative of the SAS peak which serves as the error signal. In the end, when the laser frequency is set at the resonance peak and the PZT scanning is turned off, the error signal is fed back to the EC PZT to compensate for any drift away from resonance.

4.2 Modulators

Two LiNbO₃-based integrated-optic modulators (Photline TechnologiesTM) are utilized for phase- (NIR-MPX-LN03) and amplitude modulation (NIR-MX-LN03) (figure 4.3). The advantage of those modulators is, that they make use of the linear electro-optic effect in a LiNbO₃ crystal, which changes the indices of refraction of the crystal proportional to the magnitude of an external applied field [47]. The NIR-LN LiNbO₃ are specially designed for near infrared

wavelength as used in the ARP-experiment. The correct description of the electro-optic effect in a crystal is rather complex since it is described by a third rank tensor [48]. But the complexity can be greatly reduced, if the E-field is applied on one of the principle axes of the crystal and if the polarization axis of the light is properly chosen with respect to the symmetry of the crystal. There are some characteristics that make LiNbO₃ really useful for the conditions in this experiment. It is an anisotropic, uniaxial crystal with good optical and electrical properties. The strongest electro-optic coefficient is r_{33} , that lies in the Z-direction. So, it is beneficial, when the applied electric field as well as the polarization of the light is aligned with the Z-axis. When light is now propagating perpendicular to the electric field, it sees a change of the index of refraction that is proportional to the applied electric field. Therefore the light gets an optical path length change and thus creates an additional phase shift along its path.

In order to produce a moderate phase shift, a large electric field has to be applied because the electro-optic coefficients are in general very small, for instance (LiNbO₃) $r_{33} = 32$ pm/V in the ARP-experiment. For big modulators, this causes some practical difficulties because there is a high drive voltage required. In a waveguide-type integrated-optic modulator however, a big electric field causes no problems and it is achievable with a much lower

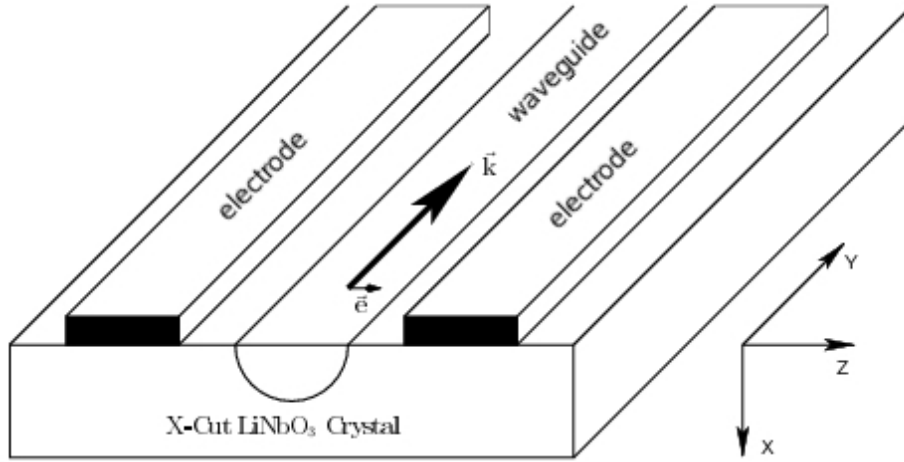


Figure 4.3 The schematic of a X-cut LiNbO_3 modulator. The light propagates in the Y-direction (\vec{k}) and the two electrodes, that are also along the Y-axis produce the electric field along the Z-axis for modulation. \vec{e} represents the polarization axis in the crystal.

drive voltage because the optical and electric field are localized in a much smaller region of the modulator. The modulators that are used in the lab (PhotlineTM NIR-LN) use crystals with X-cut, where the waveguide is along the Y-axis. This is done by manufacturing the electrodes along the Y-axis on the Y-Z-plane and fabricating the optical waveguide between the two electrodes. These two electrodes provide the electric field along the Z-axis. The light enters the waveguide from the X-Z-plane, travels along the Y-axis and is also polarized along the Z-axis. The fabrication of the waveguides in those Photline modulators is done by using proton exchange technology. So, Li^+ ions in the LiNbO_3 -crystal are exchanged with protons that are offered when

placing the patterned crystal in a proton rich acid bath. The result of this process is, that the index of refraction of the extraordinary light in the patterned region that guides the light in width (Z) and depth (X) permanently increases. When Cr-Au travelling wave electrodes are deposited over a thick dielectric buffer layer, undesirable optical absorption is minimized and also the microwave to optical phase matching condition is satisfied. In order to prevent them from environmental disturbances, the modulator chips are sealed in 100 mm \times 15 mm \times 9 mm metal boxes. These assemblies are then each arranged inside transparent plastic boxes, so that they are better protected against temperature drifts. A polarization maintaining (PM) fiber is attached to the input face of the modulator chip in order to ensure that the polarization of the input light is properly aligned with the electric field. The output fiber can be chosen to be SM (single mode) or PM. The pigtailed fibers are connected with standard FC/APC connectors with 8° angled ferrules for reducing reflection back into the fibers. A brief description of the mode of operation of the amplifiers will be given in the following sections.

4.2.1 The Phase Modulator

Now the working mechanism of the phase modulator is explained: A sinusoidal radio-frequency (RF) signal is applied to the two electrodes of the modulator.

It can be shown, that the total phase delay that is introduced to the light travelling along the waveguide with wavelength λ and polarization along the Z-axis (extraordinary light) is given by

$$\Phi(t) = \kappa M(\omega_m) V(t) = \kappa M(\omega_m) V \sin(\omega_m t), \quad (4.1)$$

where ω_m is the frequency and V the amplitude of the sinusoidal signal. Other than that, κ can be written as $\kappa = \frac{\pi}{\lambda G} n_e^3 r_{33} \eta L$. Here, G and L represent the gap and the length of the electrodes, while r_{33} denotes the electro-optic coefficient and n_e is the index of refraction for the extraordinary light. The dimensionless parameter $M(\omega_m)$ describes the frequency dependence of the phase delay, which results from RF losses and RF to optical phase mismatch. The parameter η is the overlap coefficient between the electric field and the optical field (see the Photline webpage). See figure 4.4 for the layout of the phase modulator.

The voltage that is required to produce a phase shift of π (phase modulator) is called the half-wave voltage V_π , which is also frequency dependent. At a certain frequency, the half-wave voltage is given by

$$V_\pi(\omega_m) = \frac{\lambda G}{n_e^3 r_{33} \eta L M(\omega_m)} \quad (4.2)$$

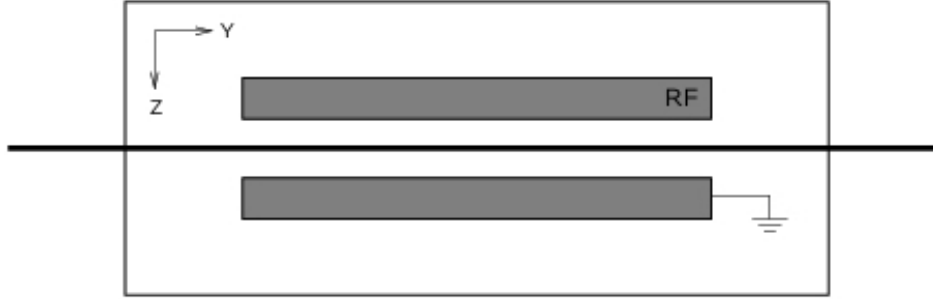


Figure 4.4 Schematic layout of a phase modulator. The principle axes of the crystal are shown in the upper left corner of the graph.

Using DC so that $M=1$, the result is

$$V_{\pi} = \frac{\lambda G}{n_e^3 r_{33} \eta L}.$$

When there is a fixed sinusoidal RF modulation signal, the phase modulated optical field can be written as

$$E(t) = E_0 \cos [\omega_1 t - \beta \sin (\omega_m t)], \quad (4.3)$$

with the amplitude of the light field E_0 and the angular frequency of the unmodulated light ω_1 . The modulation index β is defined as follows:

$$\beta = \kappa M(\omega_m) V = \frac{\pi}{\lambda G} n_e^3 r_{33} \eta L M(\omega_m) V = \frac{\pi V}{V_{\pi}(\omega_m)}. \quad (4.4)$$

Unfortunately, it is not easy to determine $V_\pi(\omega_m)$ for a phase modulator. There is one way to measure the half-wave voltage via calculating the modulation index β from the measured Fourier spectrum of the phase modulated optical field with a sinusoidal modulation voltage applied. This will be described in the next chapter.

Since phase modulation is equivalent to frequency modulation in the same sense that the instantaneous angular frequency of a light signal is the time derivative of the overall phase, the instantaneous angular frequency for a phase modulated signal can be written as

$$\omega(t) \equiv \frac{d\Phi(t)}{dt} = \omega_1 - \beta\omega_m \cos(\omega_m t) \quad (4.5)$$

It is therefore obvious that sinusoidal phase modulation results in sinusoidal frequency modulation at the same frequency ω_m , but with a phase lag of 90° .

4.2.2 The Amplitude Modulator

The amplitude modulator (AM) is constructed by patterning a Mach-Zehnder (MZ) interferometer onto a LiNbO₃ substrate [46]. It is known from chapter 4.2.1, that the phase modulator has a single light path. However, in the AM the input optical waveguide is split into two paths and then recombined at the

output end. The two waveguides are sandwiched by three parallel electrodes that are deposited on the substrate. The two side electrodes are grounded, whereas the middle electrode is divided into two sections in order to apply a DC bias and RF signal separately. The principle layout of the amplitude modulator can be viewed in figure 4.5. If there is a voltage applied to the center electrode, this results in opposite electric fields across the two paths of the interferometer and thus a change in the index of refraction in opposite directions. So the optical phase shift that is induced by that increases in one path and decreases in the other one.

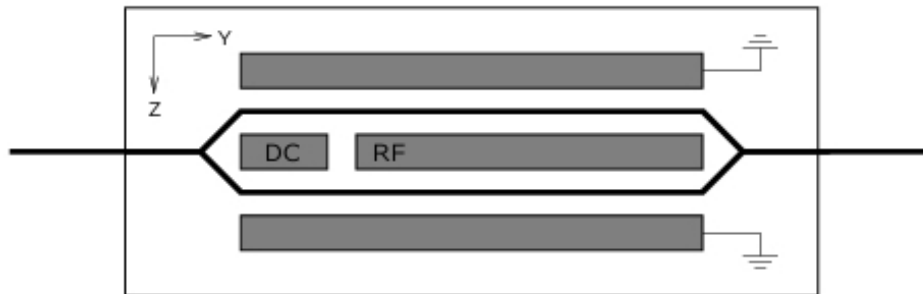


Figure 4.5 Schematic layout of an amplitude modulator. The principle axes of the crystal are shown in the upper left corner of the graph.

The light, that is going through the two parallel paths is then recombined coherently at the output. Now a $2n\pi$ net phase difference between the two paths results in constructive interference, while a $(2n + 1)\pi$ net phase differ-

ence means destructive interference. The output electric field then is

$$E(t) = \frac{E_0}{2} [\cos(\omega_1 t + \Phi(t)) + \cos(\omega_1 t - \Phi(t))] = E_0 \cos(\Phi(t)) \cos(\omega_1 t), \quad (4.6)$$

with the phase shift $\Phi(t)$ induced on one arm of the MZ-interferometer that is proportional to the applied voltage as in the phase modulator. It is important to know that the phase shift on the other arm has an opposite sign, so that the total phase difference is given by $2\Phi(t)$. In case of a DC voltage applied to the electrodes, the amplitude of the output field $E_0 \cos \Phi$ is constant because Φ is constant. But if an RF signal is applied to the electrodes, the amplitude envelope of the output field is given by $E_0 \cos(\Phi(t))$. So it is clear that the amplitude is modulated with a modulation frequency that is equal to the RF. The optical power output of the AM can be written as

$$P_{\text{out}} = \frac{P_0}{2} [1 + \cos(2\Phi(t))], \quad (4.7)$$

with the maximum power output P_0 . The Mach-Zehnder amplitude modulator is very sensitive to variations of the operating conditions, because it is an interferometric device exhibiting a sine transfer function. The DC electrodes are separated from the RF electrodes, so that it is possible to adjust the operating point of the MZ modulator independently from the high frequency

signal applied. So the desired operating point can be set by a fixed voltage applied to the DC bias electrodes.

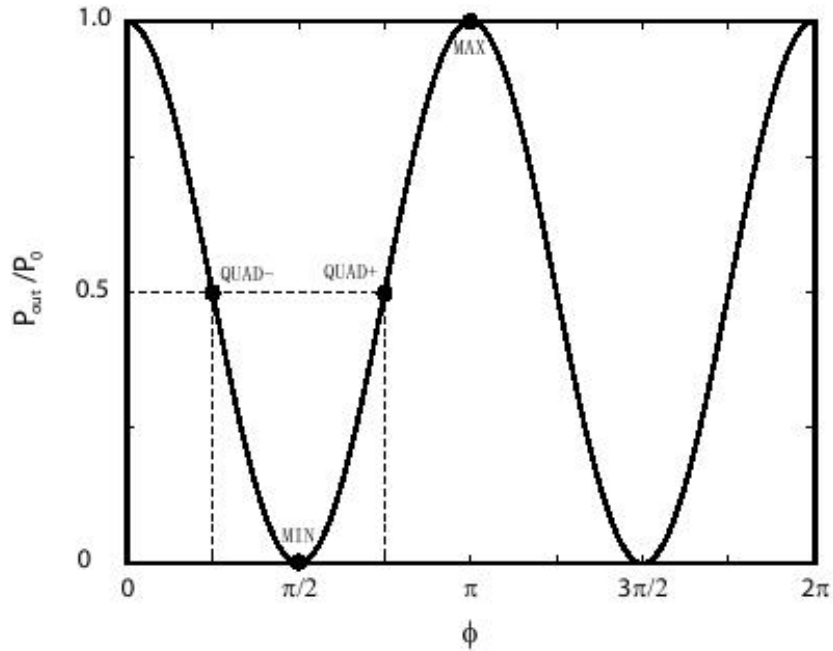


Figure 4.6 Power (vertical axis) against phase shift (horizontal axis) on one arm of the Mach-Zehnder amplitude modulator. Since the phase shift on the other arm has the same magnitude but opposite sign, the total phase shift has to be doubled. Possible operating points are also shown in the plot. In this experiment, the minimum was used as operating point [13].

The modulators are often biased at a half-power point (QUAD+ or QUAD-) of its transfer function for linear operation, e.g for applications such as analog or digital transmissions [13]. However, pulse generation is needed in the experiment, so the modulator should be biased at an extreme point of its transfer function (MIN or MAX) (figure 4.6). Since the minimum power point is more

stable it is more favorable in operation. A quarter-wave voltage is enough to bring the output optical power from minimum to maximum, the RF amplitude should be limited to half $V_\pi(\omega_m)$ at a given frequency ω_m . Here, the voltage that produces a π -phase shift on one arm of the Mach-Zehnder AM is V_π . Note, that this is different from the manufacture's value by a factor of 2 since they refer to the total phase difference of the two arms.

4.2.3 Production of Chirped Pulses

Remember that in ARP, each adiabatic rapid passage is induced by a chirped pulse, while multiple repetitions of ARP sweeps with chirped pulses from counterpropagating light beams enable the huge force that pushes the atoms. So the first step (and one of the main tasks) of the experiment is to produce periodic chirped pulses. With the phase modulator NIR-MPX-LN03 it is easy to produce periodic chirps. Note, that the optical field that is phase modulated with a sinusoidal RF signal is described by Eq. (4.3), while the instantaneous frequency is given by Eq. (4.5). In case of $\omega_l = \omega_a$, that is when the laser frequency is set to the frequency of atomic resonance, the instantaneous frequency of the modulated light chirps from $\omega_a - \beta\omega_m$ to $\omega_a + \beta\omega_m$ at each first-half period and chirps back at each second-half period, which generates the periodic frequency chirp that is needed to do the ARP-experiment properly.

The 160 MHz RF drive signal of the phase modulator is delivered by a HP8657D signal generator that is amplified by a Mini-Circuit ZHL-5W-1 high power amplifier. This amplifier has a fixed gain of 45 dB ($1 \text{ dB} \approx 0.115 \text{ Np}$) when it is powered with a 24 Volts DC from a Power Design Inc. model 6105 universal power supply. See figure 4.8 for a block-diagram of the setup. The output power level is determined by the RF input power from the HP8657D. It is important to know that the maximum power output of the amplifier ($\sim 37 \text{ dBm}$) is higher than the maximum input power of the phase modulator ($\sim 34 \text{ dBm}$), so it is absolutely necessary to be very careful when varying the power level in the HP8657D. No more than -11 dBm ($\sim 63 \text{ mV RMS}$ for a sine wave) should be generated by the HP8657D to avoid overloading the phase modulator RF termination. In order to produce periodic pulses with the NIR-MX-LN03 AM, a pulse generator is required. A Power Design Inc. model 2005 precision power supply provides the bias voltage for the amplitude modulator. The AM is driven at a trigger frequency of 80 MHz by a HP8082A pulse generator that is triggered by a HP8657A signal generator. This pulse generator operates at approximately 25% duty cycle at this frequency with its shortest pulse output $\sim 3 \text{ ns}$. Therefore, there is a dark time of 75%. When operating at the minimum pulse width, the electrical pulse has a triangular like shape. The output voltage is $\sim 4 \text{ V}$, which is about half V_π . So the RF

pulses are applied to the modulator. The complementary output of the pulse generator is used as a monitor signal. The measured amplitude envelope as well as the electronic monitor signal are displayed on and saved by a Lecroy WS434 digital osilloscope. Note that the pulse profiles, especially the optical pulse profile, exhibit some electronic noise which makes the pulse length measurement inaccurate (figure 4.7).

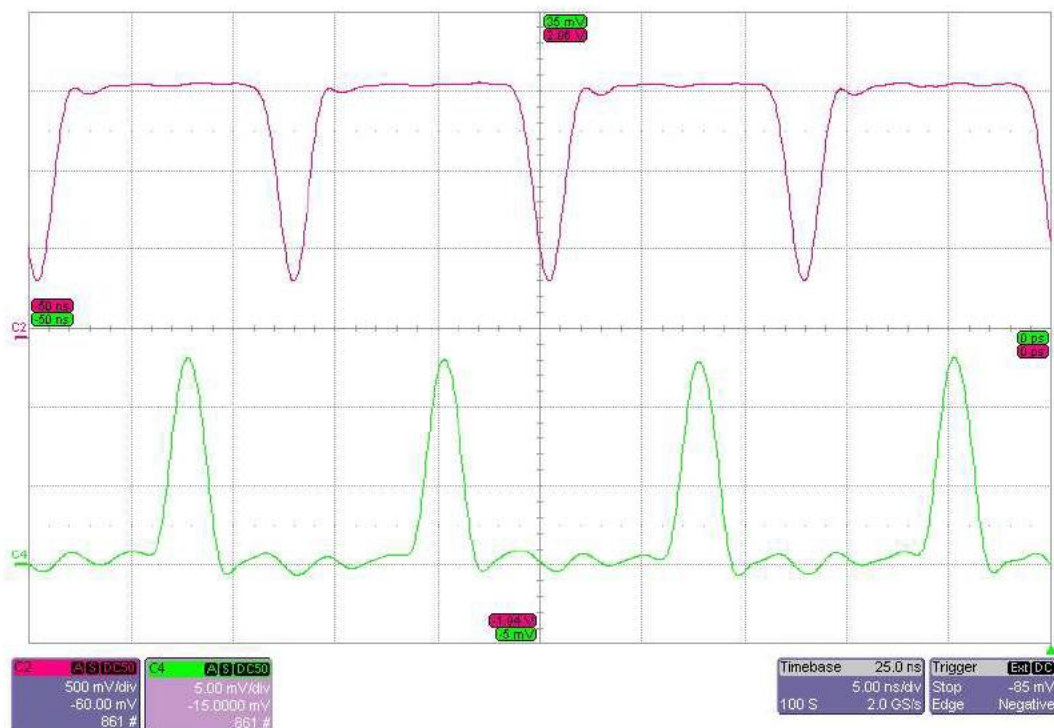


Figure 4.7 Image of the periodic optical pulse delivered by the NIR-MX-LN03 AM (lower image) and the complement of the RF drive signal (upper image). The frequency of both signals is 80 MHz and the pulse width is about 3.5 ns. Note, that the optical signal shows some ringing at the base which might be induced by the after-pulse tail of the electric signal together with some RF reflection.

It is necessary to synchronize the frequency chirping and amplitude pulsing in order to produce chirped pulses. This can be done by synchronizing the HP8657D and the HP8657A. Actually the HP8657D and the HP8657A are driven by a high precision timebase output from the HP8657D. Using the delay knob in the pulse generator the relative phase between the phase modulator drive signal and the amplitude modulator drive signal can be adjusted coarsely. The fine adjustment is being done using the phase control button of the HP8657D signal generator.

4.3 Fabry-Perot spectrometer

Until here, the monochromatic laser output was first sinusoidally phase modulated and then amplitude modulated with a periodic pulse signal, which results in a non simple field. In order to characterize this modulated light field, two Fabry-Perot (FP) spectrometers have been built by Dr. Xiyue Miao [13]. Basically, a FP spectrometer is a scanning FP interferometer [46, 50]. For this special experiment, there were a few things that needed to be taken into account when the FP was being built. First of all it is important that the FP is able to measure a strongly frequency modulated signal. Since the modulation frequency is around 100-200 MHz and the modulation index can be larger than a few π , the free spectral range (FSR) of the FP needs to be a few GHz, which

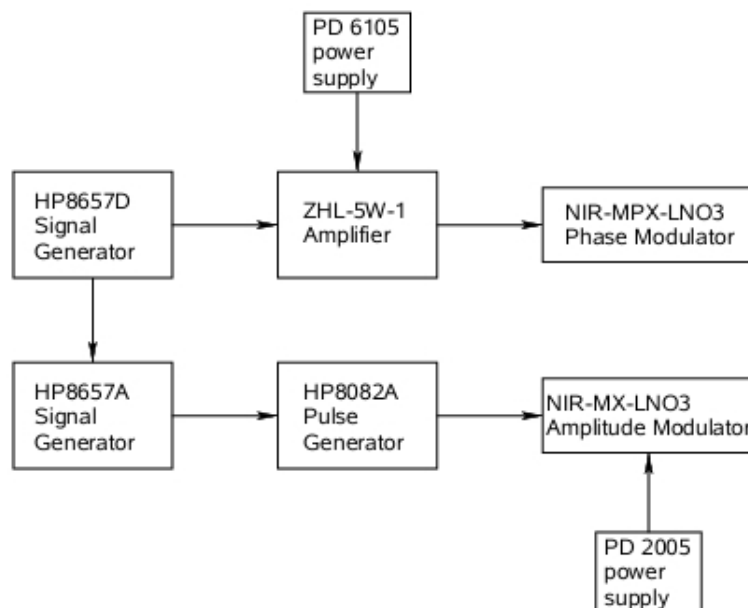


Figure 4.8 Supply of the modulators with the RF-signal. The RF-signal of the NIR-MPX-LN03 phase modulator comes from a HP8657D signal generator. The signal is amplified by a Mini-circuit ZHL-5W-1 amplifier which is powered by a PD 6105 power supply. The NIR-MX-LN03 amplitude modulator is driven by a HP8082A pulse signal generator that is triggered by a HP8657D signal generator. The required DC bias voltage of NIR-MX-LN03 (see fig. 4.5) is supplied by a PD 2005 power supply. By synchronizing the two signal generators, synchronized driving of the modulators is achieved.

means that the cavity of the FP needs to be very short. Another important point is, that it must be possible to distinguish between the neighboring peaks that are separated by the modulation frequency, so the width of the FP transmission needs to be lower than the modulation frequency. Therefore a high finesse for a FP with a large FSR is needed. The FP's that are used here have a $\text{FSR} = 3 \text{ GHz}$. For the length of the cavity l it holds $\text{FSR} = \frac{c}{4l}$ and

thus $l = 25$ mm. The mirrors of the cavity are partial reflectors from CVI laser. Their flat surface is antireflection coated for 1083 nm light and their curved surface has a reflectivity of 98.7%. The diameter of the mirrors is 1.27 cm, their thickness is 0.95 cm and their focal length is 25 mm, which is in accordance to the length of the cavity. The PZT tube is 1.27 cm O.D. \times 1.12 cm I.D. \times 1.27 cm length (figure 4.9).

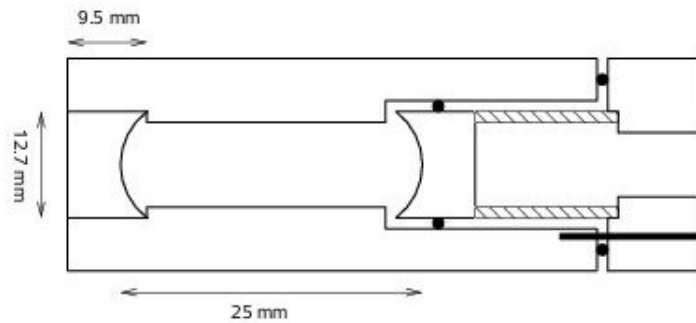


Figure 4.9 Schematic of the Fabry-Perot spectrometer. The length of the cavity is 25 mm, the mirror diameter is 12.7 mm, their focal length is also 25 mm and the thickness 9.5 mm.

Invar has been used for the body of the FP, due to its low thermal expansion coefficient. It consists of a tube and a cap. There is a mirror epoxied on one side of the tube and a PZT and a mirror are epoxied on the cap. The whole piece was then inserted in the other side of the tube. By applying a voltage on the PZT with a homemade PZT controller, the cavity length and thus the resonance frequency of the FP interferometer is tunable. Behind the FP there is a photo detector (Thorlabs 110) with which the transmitted optical power

can be measured. In this way, the scanning Fabry-Perot interferometer acts as an optical spectrum analyzer. When the voltage of the PZT is ramped, a frequency spectrum of the input signal is produced. With careful alignment and a $f = 500$ mm lens for mode matching, a Finesse of 60 can be obtained for both FP-spectrometers, that are used in the ARP-experiment. A more detailed description of the Fabry-Perot-spectrometers can be found in [13].

4.4 Fiber Optic Amplifiers

Under normal outputting conditions, the EC diode laser has a linearly polarized output of around 20 mW in the main beam. Each modulator has about 4 dB insertion loss, which amounts to about 60% loss for each modulator. Since the amplitude modulator has a 25% duty cycle pulse operation, there is at least an expected optical power loss of another 75%. Considering the fiber coupling loss of the free space laser output to the modulator and fiber to fiber coupling loss, the optical power easily drops to less than 0.1 mW. Since a high peak Rabi Frequency ($\Omega \gg \omega_m$) is required for the atomic state to adiabatically follow the optical field in an ARP process and since it is necessary to scan along the axis of Rabi Frequency in order to map the ARP force in parameter space, a lot more power is required in the experiment. For this purpose, two optical fiber amplifiers are utilized. In this experiment, light with a wavelength

of 1083 nm is produced and therefore Ytterbium(Yb)-doped fibers are used as the gain medium. These Yb-doped fiber amplifiers (YDFA) are manufactured by KeopsysTM. Yb-ions doped in the fiber core result in a broad absorption spectrum that is peaked at 977 nm, where high-power, broadstrip diode lasers are commercially available. The input signal that has a wavelength of 1083 nm is amplified by stimulated emission, when there is a population inversion in the fiber, which can be achieved by pumping at 977 nm. The Yb-doped fiber has a double cladding: The pump light is injected from a V-groove mechanically formed in the outer cladding and propagates in the inner cladding to provide amplification along the input light path in the fiber core. Both fibers, the one for the input and the one for the output of the YDFA, are Single Mode (SM) for 1083 nm and are connected with FC/APC connectors. In order to couple the fiber modulators to the fiber amplifiers directly, FC/APC to FC/APC mating sleeves are used. This results in a coupling efficiency of $\sim 80\%$.

Because of its broadband, long tail emission spectrum from 1060 nm to 1200 nm [51], YDFA is suitable for ultrashort pulse amplification. In order to boost the power of the chirped pulse to the required level for the experiment, a model KPS-BT2-YFA YDFA was used, which has two gain stages with an optical isolator in front of each amplification stage to prevent any high power optical feedback. The first stage is a saturated amplification stage that

provides a constant output of ~ 190 mW, while the second stage is pumped by two diode lasers whose current can be turned on successively. The gain of the amplifier is proportional to the injection current of the laser diodes with a slope of ~ 590 mW/A. When the first diode current is set to its maximum, that is at 5A, the output power is about 3 W. By adding current to the second laser diode, further amplification can be obtained and the maximum power output of the FA is 4.3 W [40]. Apart from that, the power level is the same for CW operation and pulse operation. Another YDFA of the same model was used to amplify the optical pumping signal. The production of the chirped pulses is shown in figure 4.10.

In order to operate properly, the YDFA needs a certain minimum input signal power. If this condition is not satisfied, the signal is too low to deplete the population inversion of the doped Yb-ions. Then, Amplified Spontaneous Emission (ASE) and self lasing can occur which can lead to the breakdown of the internal isolator of the YDFA and possible damage of other optical elements in the optical train. It is necessary to be aware of this fact and never disrupt the beamline, while the FA is running. For the KPS-BT2-YFA a minimum power input of 0.5 mW is therefore required. But the optical power level after two modulation steps is too low to fulfill this condition. For this reason, another FA (1 W YDFA, model OIYb30) was inserted between

the phase modulator and the amplitude modulator as a preamplifier. This FA has no internal isolator and therefore ASE and self lasing can be problems when running the experiment. In order to protect the diode laser from possible damage because of ASE, an OFR model IO-3-1083-HP Faraday isolator, which allows $\sim 90\%$ transmission in the forward direction and provides an isolation of ~ 40 dB in the reverse direction, was placed after the DBR laser, which is very pleasant for the laser. The free space light that passes through the isolator was then coupled into the input fiber of the NIR-MPX-LN03 phase modulator by an OFR PAF-X-7-1083 fiber coupler. A $\lambda/2$ -plate is required to get the correct linear polarization at the input, because the input fiber of the phase modulator is a polarization maintaining fiber. The output of the phase modulator is then coupled to the input fiber of the 1 W YDFA by a standard FC/APC to FC/APC mating sleeve. Since this FA had been used in other experiments for several years, some parts of it are damaged and ASE and self lasing occurred. Therefore a short SM patch cord is inserted between the phase modulator and the 1 W YDFA, which serves as a fuse. Luckily, a low current setting of $I < 0.8$ A, with an input power of 76 mW, is sufficient in this experiment, when there is acceptable fiber coupling in the later stages of the optical system.

Behind the output of the 1 W YDFA, the beam is collimated by a ThorLabs

F220FC-C fiber coupler and is sent through a Polarization Beamsplitting Cube (PBC) in order to split off a small fraction for analysis. The polarization of the input signal is changed when it is propagating through a SM fiber, since physical stresses can cause birefringence in an optical fiber. Because of that, the input and the output fibers are coiled, bent and secured to maximize the wanted polarization component going to the next step of the experiment. To couple the light into the NIR-MX-LNO3 amplitude modulator, another $\lambda/2$ -plate and a OFR PAF-X-7-1083 fiber coupler are used. Behind that, a 90/10 fiber splitter for a wavelength of 1083 nm was connected with the 90% output coupled to the input of the 4 W YDFA, while the 10% output is used for analysis. In the end, the amplified output of the 4 W YDFA is again collimated and split by a PBC to direct the main laser beam towards the atomic beam and the split beam for analysis. Again, the fibers are coiled, bent and secured in order to set the polarization of the output light as wanted. For the fine-tuning of the polarization, there is a built-in polarization control element in the 4 W YDFA, with which one can precisely squeeze and twist a small section of the output fiber.

4.5 Interaction Region

The main laser pulses that were amplified and chirped before and that are intended for the experiment are further collimated and expanded with a spherical and a cylindrical telescope in order to get an elongated spatial profile, so that a flat spatial intensity profile is produced in the interaction region. Between these two telescopes another $\lambda/2$ -plate and a PBC are inserted in order to vary the light intensity of the light that will interact with the atoms. The ARP-beam has a Gaussian profile with waists of $\omega_{\text{long}} = 7.0$ mm and $\omega_{\text{short}} = 2.1$ mm, where ω is the $1/e^2$ radius of the Gaussian intensity fit. For further illustrations of the setup see figures [4.11](#) and [4.13](#).

The major axis of the light is oriented to be along the propagation direction of the atomic beam. In order to cut off the wings of the beam, a vertical slit is inserted in the laser beam. This slit was designed and built so that both beams (ARP and Optical Pumping) have a proper distance. Behind this slit there is a $\lambda/4$ -plate to produce circularly polarized light out of the linearly polarized light of the original beam. The circularly polarized light is demanded by the $2^3\text{S}_1 \rightarrow 2^3\text{P}_2$, $\Delta m_j = +1$ He* transition.

The ARP-beamline already existed, since there have been done measurements before by Dr. Xiyue Miao. Another task of the work for this thesis is to realize the Optical Pumping beamline and to split a small fraction off the

optical pumping light as the SAS-feedback. The main part of the 21%-beam is therefore directed to the other 4W YDFA (figure 4.12). Behind this amplifier, there is a PBC in order to split a small fraction off the beam and direct it to the SAS-setup for providing a lock signal for the laser (see section 4.1.2). The other part of the beam is used for optical pumping. In the same way as the ARP beam, it is also collimated and expanded with a spherical and cylindrical telescope. This is also necessary since a widened pumping beam (8 mm) is needed. Calculations show, that the pumping time from the lowest sublevel of the ground state ($m_j = -1$) to the sublevel with $m_j = 1$ is about $5.6 \mu\text{s}$. With a longitudinal velocity of the atomic beam of $1000 \frac{\text{m}}{\text{s}}$ the interaction length should be at least $\sim 5.6 \text{ mm}$. So 8 mm as it is used in this experiment should be sufficient. The output power of the YDFA was a bit too high so a filter was included, so that the power is low enough so that the Doppler push caused by the optical pumping beam is negligible. The $\frac{\lambda}{2}$ -plate associated with the big $\frac{\lambda}{4}$ -plate (that is used for both beams) then produces the desired circularly polarized light for the optical pumping process. This circularly polarization is cleverly chosen to be the same as the one of the ARP-beam (otherwise it would be obviously counterproductive).

Behind the $\frac{\lambda}{4}$ -plate, the ARP-light arrives in the interaction region. It is sent across the atomic beam and then retroreflected with a high reflection

mirror to cross with the atomic beam again on its way back. The wavelength of the amplitude modulated pulse train is called λ_m and the distance between the crossing point and mirror is chosen to be $\frac{\lambda_m}{8} = \frac{15}{32}$ m. This acrobatic exercise has the purpose to produce a $\frac{\pi}{2}$ phase delay to the retroreflected light. The atomic beam is then pushed by the periodic chirped pulse pairs, while the $\frac{3T}{4}$ dark time in between the pulse pairs on average serves to prepare the He* atom in the ground state by spontaneous emission as discussed in section 2.5. In the ARP-experiment, a periodic pulse train is used rather than the multiple reflection of a single pulse in a cavity as proposed in [23] because the pulse amplitude does not decay in time, so that the force is stronger and more stable. In the very end, the deflection of the atomic beam was imaged by a MCP/PS with a CCD camera about 32.65 cm downstream in the lithography chamber. The deflection distance is now measured from the image and so the force that is produced by the periodic chirped pulses can be calculated.

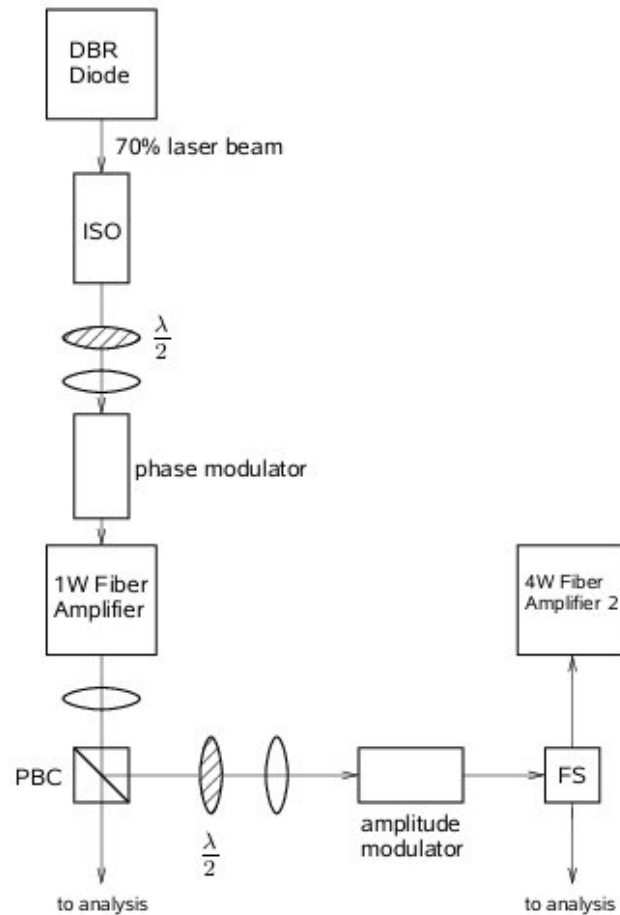


Figure 4.10 After the 70% beam of the DBR laser went through an isolator it is brought into the phase modulator. The output of the phase modulator is preamplified by a 1 W YDFA and then lead into the amplitude modulator. The result is a chirped pulse and is sent through a fiber splitter to the 4 W YDFA in order to rise the power to a useful level for the experiment. The light that is split after the fiber splitter and the 1 W and the 4 W YDFA is used for spectrum analysis.

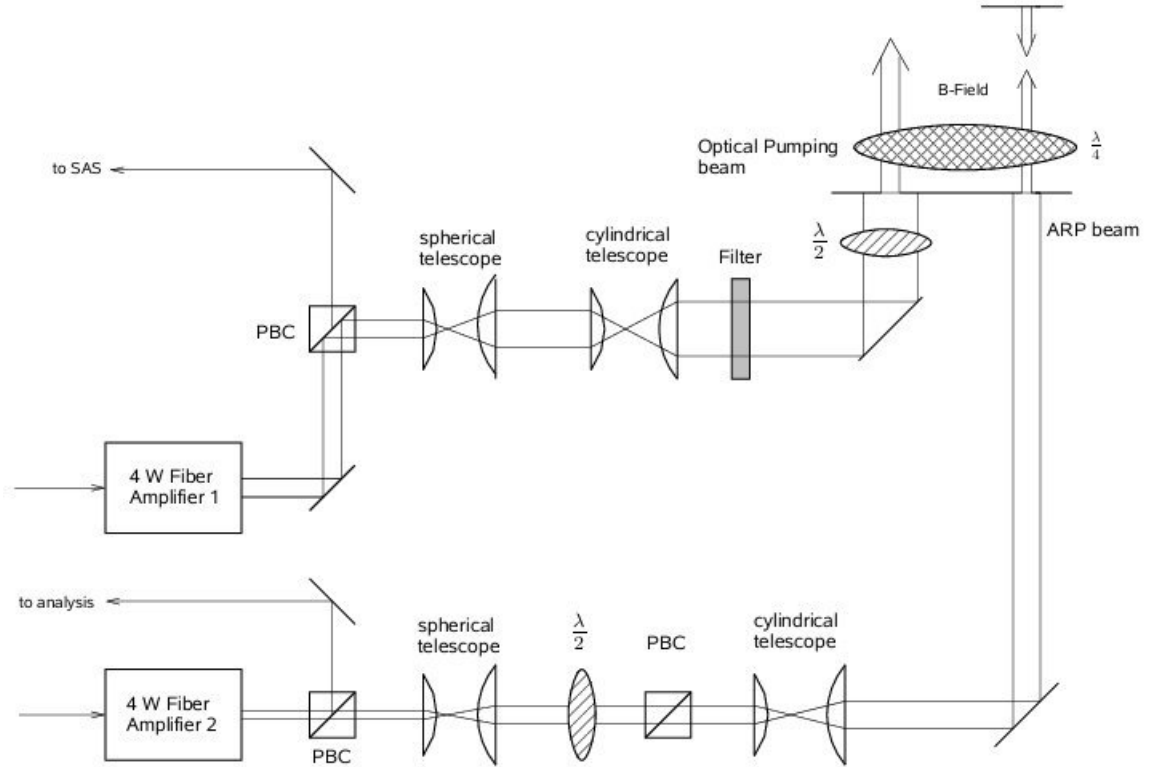


Figure 4.11 The schematic of the optical setup. The laser output of the 4 W YDFA 1 is split and one part is sent back to provide the SAS feedback for the laser, while the other part serves as the optical pumping beam for the experiment. This optical pumping beam is collimated and expanded by a spherical and a cylindrical telescope in order to get the right size of the beam. The filter is put into the beam in order to reduce its intensity. The $\lambda/2$ - and the big $\lambda/4$ -plate are used to produce circularly polarized light. The laser output of the second YDFA is also split by a PBC. One part is used for analysis and the main part is used as the ARP beam in this experiment. This beam is also collimated and expanded with a spherical and a cylindrical telescope and sent through the $\lambda/4$ -plate that is used for both beams. The $\lambda/2$ and the PBC serve as an intensity control. The major axis that was aligned with the atomic beam was further defined with a vertical slit to produce a rather flat intensity in the interaction region. The size of the optical pumping beam was also defined by a vertical slit.

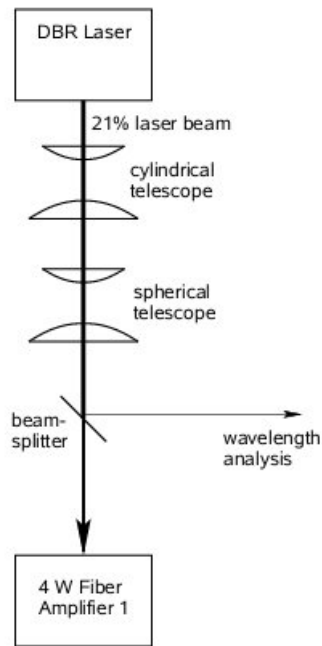


Figure 4.12 The origin of the Optical Pumping beam. The 21% laser beam is brought to a useful shape by a cylindrical and a spherical telescope. After that it is split, where one part is used for wavelength analysis and the other part is sent to a 4 W YDFA to provide the optical pumping beam and the SAS feedback.

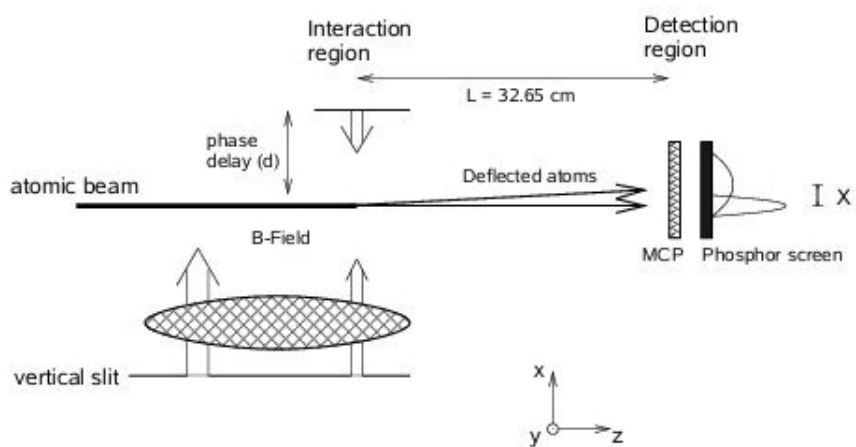


Figure 4.13 A enlarged illustration of the interaction region. The Optical pumping beam (OP) is sent across the atomic beam which fly through the magnetic field, in order to pump the atoms in the $2^3S_1, m = 1$ ground state. The ARP-beam (ARP) is also sent across the atomic beam but retroreflected with a high reflectivity mirror for another intersection with the atomic beam. The delay path was set to provide the necessary $\frac{\pi}{2}$ phase delay to the retroreflected light for the production of the unidirectional force. The measurement of the deflected atoms is accomplished with a MCP/PS detector 32.65 cm downstream.

Chapter 5

Making and probing chirped pulses

In principle a Fabry-Perot spectrometer performs a Fourier transform of the input light field. The problem is, that the phase information of each frequency component is lost and only the amplitude information is captured by the photo detector. This means that only $I^F(\omega) = |A^F(\omega)|^2$ can be caught. Here, $I^F(\omega)$ is the intensity and $A^F(\omega)$ the amplitude of the Fourier component at frequency ω . But even though the phase information of each Fourier component is lost, the phase information of the light field is still partially captured by the FP-spectrometer.

5.1 Spectrum of Periodically Modulated Light

It is known that mathematically there are three equivalent representations of Fourier expansions of a periodic real function in time. At a fixed position of a

monochromatic field, that is modulated with periodic signals, the generic form of this field is given by

$$E(t) = A(t) \cos(\omega_1 t + \Phi_p(t)), \quad (5.1)$$

with the carrier frequency of the light ω_1 and the modulated amplitude $A(t)$ and phase $\Phi_p(t)$. The frequencies of the amplitude modulation and the phase modulation may not necessarily be the same. When the common frequency of these two frequencies is written as ω_c , e.g. the common period is $\frac{2\pi}{\omega_c}$, then the field of the form of Eq. 5.1 has Fourier components at frequencies $\omega_1 \pm n\omega_c$ with an integer n . The three equivalent forms of the Fourier-Spectrum can in general be written as:

$$E(t) = \sum_{n=-\infty}^{\infty} [a_n \cos(\omega_1 + n\omega_c)t + b_n \sin(\omega_1 + n\omega_c)t] \quad (5.2)$$

$$= \sum_{n=-\infty}^{\infty} A_n^F \cos[(\omega_1 + n\omega_c)t - \Phi_n] \quad (5.3)$$

$$= \sum_{n=-\infty}^{\infty} [c_n e^{i(\omega_1 + n\omega_c)t} + c_n^* e^{-i(\omega_1 + n\omega_c)t}]. \quad (5.4)$$

In Eq. (5.2), the Fourier expansion coefficients are determined by

$$a_n = \frac{2}{T} \int_0^T dt E(t) \cos(\omega_1 + n\omega_c)t, \quad (5.5)$$

and

$$b_n = \frac{2}{T} \int_0^T dt E(t) \sin(\omega_1 + n\omega_c)t, \quad (5.6)$$

where $T = \frac{2\pi}{\omega_c}$.

In Eq. (5.4), the Fourier expansion coefficients are given by

$$c_n = \frac{1}{T} \int_0^T dt E(t) e^{-i(\omega_1 + n\omega_c)t}. \quad (5.7)$$

By comparing equations (5.2) and (5.3) it can be found that

$$A_n^F = \sqrt{a_n^2 + b_n^2}, \quad (5.8)$$

and

$$\Phi_n = \arctan \frac{b_n}{a_n}. \quad (5.9)$$

By comparing equations (5.2) and (5.4), it results that

$$c_n = \frac{1}{2}(a_n - ib_n). \quad (5.10)$$

Here it can be seen that $A_n^F = |2c_n|$ and therefore the spectrum of the output of the Fabry-Perot spectrometer is

$$I_n^F = (A_n^F)^2 = |2c_n|^2. \quad (5.11)$$

It is convenient to calculate the spectrum with Eq. (5.7), since the expansion Eq. (5.4) has the simplest coefficients given by Eq. (5.7), especially for modulated light that has a complicated form. So the result is:

$$\begin{aligned} I_n^F &= |2c_n|^2 = \left| \frac{2}{T} \int_0^T dt E(t) e^{-i(\omega_1 + n\omega_c)t} \right|^2 \\ &= \left| \frac{2}{T} \int_0^T dt A(t) \cos(\omega_1 t + \Phi_p(t)) e^{-i(\omega_1 + n\omega_c)t} \right|^2 \\ &= \left| \frac{1}{T} \int_0^T dt A(t) [e^{i(\omega_1 t + \Phi_p(t))} + e^{-i(\omega_1 t + \Phi_p(t))}] e^{-i(\omega_1 + n\omega_c)t} \right|^2 \\ &= \left| \frac{1}{T} \int_0^T dt A(t) e^{i(\Phi_p(t) - n\omega_c t)} \right|^2 \end{aligned} \quad (5.12)$$

The second term of the integral which is the high frequency oscillatory term averages to zero.

5.2 The Phase Modulated Spectrum

The phase modulated light field in the experiment is described by Eq. (4.3), which is given by:

$$E(t) = E_0 \cos [\omega_1 t - \beta \sin (\omega_{pm} t)], \quad (5.13)$$

with the phase modulation frequency ω_{pm} and the modulation index β . Comparison with Eq. (5.1) gives us

$$A(t) = E_0 \quad (5.14)$$

and

$$\Phi_p(t) = -\beta \sin (\omega_{pm} t). \quad (5.15)$$

The Fourier spectrum of the phase modulated light field can be derived by using the Jacobi-Anger Expansion. It can be written as

$$E(t) = E_0 \cos [\omega_1 t - \beta \sin (\omega_{pm} t)] \equiv E_0 \sum_{n=-\infty}^{\infty} J_n(\beta) \cos((\omega_1 - n\omega_{pm})t), \quad (5.16)$$

where $J_n(\beta)$ is the n'th order Bessel function of the first kind (figure 5.1).

Bessel functions have many characteristics. Here, only those properties will

be looked at, that will be used later.

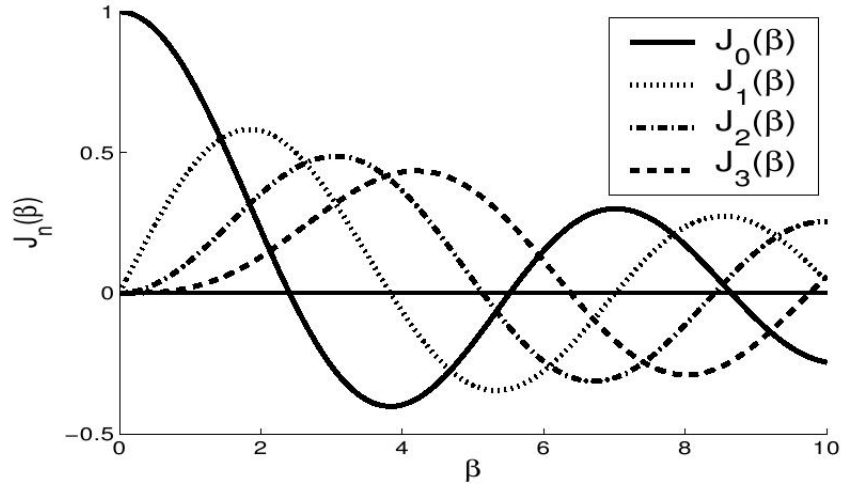


Figure 5.1 The Bessel functions J_0 , J_1 , J_2 , J_3 as functions of β [13].

1. The symmetry relation:

$$J_{-n}(\beta) = (-1)^n J_n(\beta). \quad (5.17)$$

By comparing equations (5.3) and (5.16) and with using Eq. (5.11) it yields:

$$I_n^F = E_0^2 J_n^2(\beta). \quad (5.18)$$

So it is obvious that the phase modulated field has a symmetric Fabry-Perot spectrum.

2. The recurrence relation:

$$J_{n-1}(\beta) + J_{n+1}(\beta) = \frac{2n}{\beta} J_n(\beta). \quad (5.19)$$

Therefore the value of β is obtained by using the recurrence relation from three neighboring components in the spectrum.

5.2.1 Determination of V_π for the phase modulator

The modulated light spectrum signal has been measured by a Thorlabs 110 photo detector, that is situated behind the FP interferometer [13]. The signal then was displayed and captured by a digital oscilloscope. In this oscilloscope, the associated data for each spectrum could be stored as well. A signal generator delivers the RF signal, which is amplified and then used to drive the phase modulator. Equation (5.18) says that the intensity of each frequency component in the spectrum of the sinusoidally modulated light is proportional to $J_n^2(\beta)$. When therefore the square root of the peak intensity of each spectrum data is taken, the relative value of $J_n(\beta)$ is obtained. It is also important to be careful by determining the sign of the square root, since $J_n(\beta)$ is not always positive. In order to get the sign of $J_{-n}(\beta)$, Eq. (5.17) can be used. Having obtained $J_n(\beta)$'s, β can be calculated using Eq. (5.19) with various

n. For each spectrum, β was averaged over the values obtained with different n's. After plotting the modulation index β against the output of the signal generator V_{SG} and making a linear fit, gives us

$$\boxed{\beta = 0.116 V_{SG}}, \quad (5.20)$$

where V_{SG} is given in units of mV. This is illustrated in figure 5.2(a). When β is plotted against the RF input of the phase modulator V_m , which is the amplified RF signal from the Mini-circuits amplifier, it is found by making a linear fit that $V_\pi = 4.38$ V for $\omega_{pm} = 160$ MHz. This was done in 5.2(b).

5.3 The Amplitude modulated spectrum

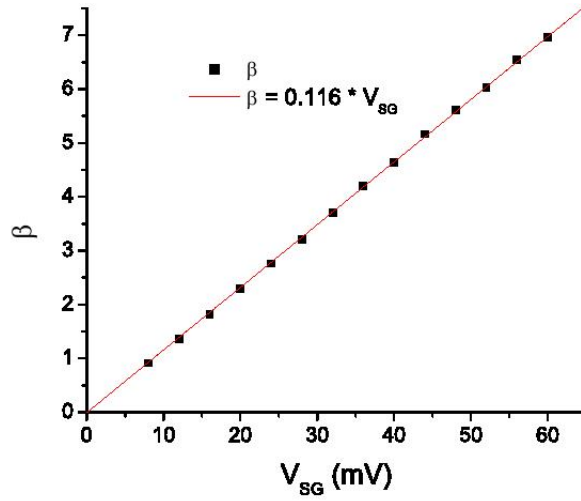
The output of the amplitude modulator can be described by Eq. (4.6), which says

$$E(t) = E_0 \cos(\Phi_a(t)) \cos(\omega_1 t), \quad (5.21)$$

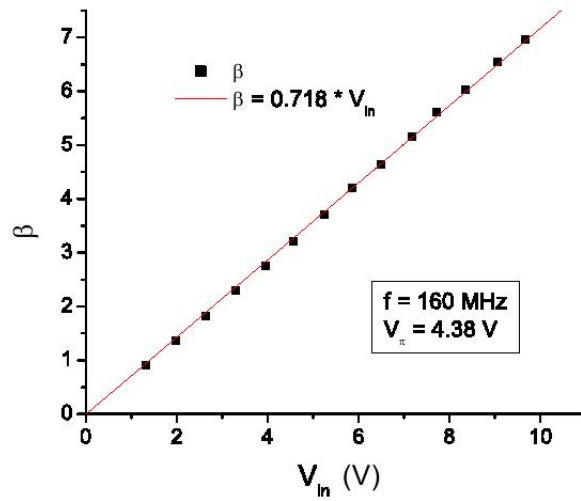
with Φ_a proportional to the applied voltage. The relation is given by

$$\Phi_a(t) = \frac{\pi V(t)}{V_\pi}. \quad (5.22)$$

With the amplitude modulation frequency ω_{am} , the Fabry-Perot spectrum

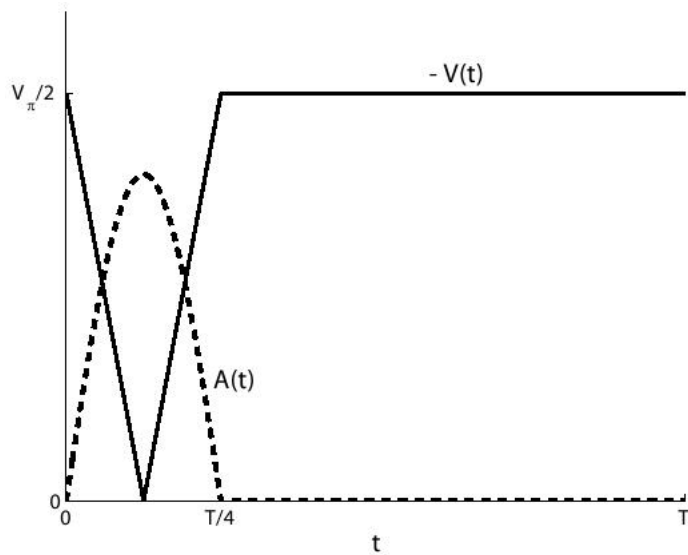


(a)

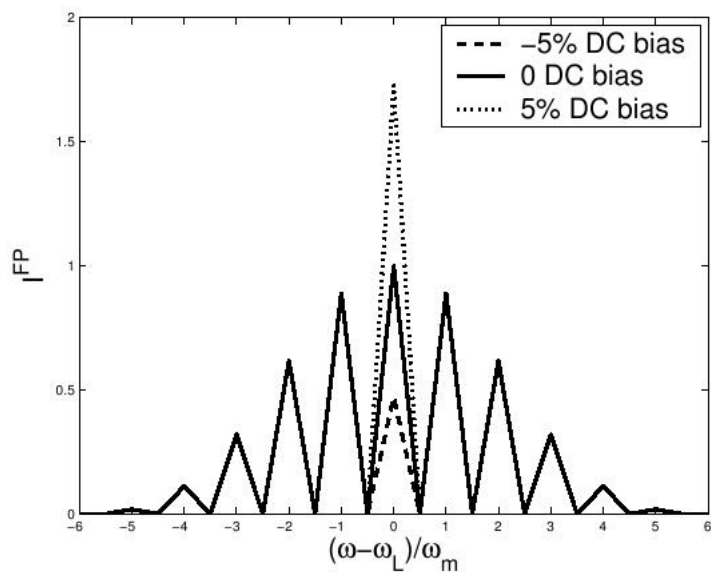


(b)

Figure 5.2 (a) The calibration curve of the phase modulation index β vs. the signal generator voltage V_{SG} . (b) The calibration curve of β vs. the input power of the phase modulator V_{in} . V_{π} was measured to be 4.38 V for the modulation frequency $\omega_{pm} = 160$ MHz [13].



(a) modulating voltage and light amplitude



(b) Fabry-Perot spectrum of the light field

Figure 5.3 The idealized amplitude modulation scheme. (a) The voltage $V(t)$ applied on the amplitude modulator is a triangular pulse and the resulting light is a sinusoidal pulse of amplitude $A(t)$, (b) amplitude modulated FP-spectrum [13].

of the light is

$$I^{\text{FP}}(\omega_l + n\omega_{\text{am}}) = \left| \frac{1}{T} \int_0^T dt E_0 \cos(\Phi_a(t)) e^{-in\omega_{\text{am}}t} \right|^2. \quad (5.23)$$

Unfortunately, the spectrum does not have an analytical formula, except for some special classes of $V(t)$. For instance in the ideal case of a syncopated (25% duty cycle) triangle-shaped electric pulse on the amplitude modulator, it yields:

$$V(t) = -\frac{V_\pi(\omega_{\text{am}})}{2} + \frac{V_\pi(\omega_{\text{am}})}{2} \begin{cases} \frac{8t}{T} & 0 < t < \frac{T}{8} \\ \frac{8}{T}(\frac{T}{4} - t) & \frac{T}{8} < t < \frac{T}{4} \\ 0 & \frac{T}{4} < t < T \end{cases}, \quad (5.24)$$

with a period of the amplitude modulation $T = \frac{2\pi}{\omega_m}$. For this kind of electric pulse, the amplitude is

$$A(t) = \begin{cases} E_0 \sin(2\omega_{\text{am}}t) & 0 < t < \frac{T}{4} \\ 0 & \frac{T}{4} < t < T \end{cases}. \quad (5.25)$$

In this case, the amplitude modulated spectrum is

$$I^{\text{FP}}(\omega_1 + n\omega_{\text{am}}) = \left(\frac{4}{4 - n^2} \right)^2 \cos^2 \left(\frac{n\pi}{4} \right). \quad (5.26)$$

The complement of the electric pulse and the corresponding optical pulse are sketched in figure 5.3(a) and the amplitude modulated spectrum is shown in figure 5.3(b).

In practice, the optical pulse can never be ideally sinusoidal, due to the fact, that the shape of the driving pulse is not exactly triangular, its amplitude is not exactly $\frac{V_\pi}{2}$, its width is not exactly $\frac{T}{4}$ and it also has some afterpulse ringing. However, the FP-spectrum of the amplitude modulated light is not too far from the ideal spectrum. The ARP-process could be ruined by a small level of CW light that is induced by DC offset of the electric pulse and would cause the overlapping of the counterpropagating light pulses. This can be minimized through the adjustment of the DC bias of the driving pulse. The FP interferometer is very handy for monitoring that since the peak at ω_1 in the light spectrum is sensitive to the CW light level while other peaks are insensitive.

5.4 Phase and Amplitude Modulated Spectrum

The experimental values in this experiment are $\omega_{\text{pm}} = \omega_{\text{m}} = 160$ MHz for the phase modulation and $\omega_{\text{am}} = \frac{\omega_{\text{m}}}{2} = 80$ MHz for the amplitude modulation frequency. Thus, the common modulation frequency is $\omega_{\text{c}} = 80$ MHz. The modulated light field then is

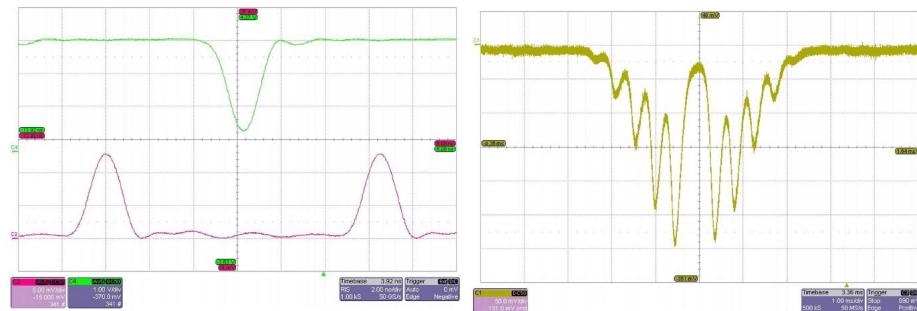
$$E = E_0 \cos(\Phi_{\text{a}}(t)) \cos[\omega_{\text{l}}t - \beta \sin(\omega_{\text{m}}t + \delta\Phi)], \quad (5.27)$$

and the FP-spectrum then is

$$I^{\text{FP}}(\omega_{\text{l}} + n\omega_{\text{c}}) = \left| \frac{1}{T} \int_0^T dt E_0 \cos(\Phi_{\text{a}}(t)) e^{-i(\beta \sin(\omega_{\text{m}}t + \delta\Phi) + n\omega_{\text{c}}t)} \right|^2, \quad (5.28)$$

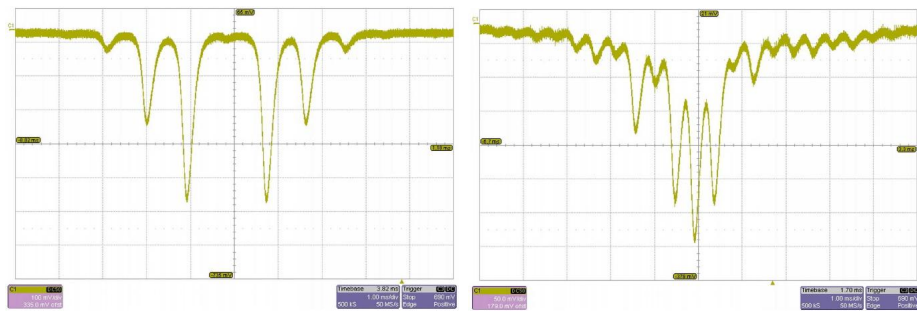
where the relative phase between the phase modulation and the amplitude modulation is given by $\delta\Phi$. For symmetric pulses with pulse width being $\frac{T}{4}$, ARP requires $\delta\Phi = \pm\frac{\pi}{2}$, so that the frequency sweeps through resonance at the maximum pulse amplitude. In this case, the light field that is given by Eq. (5.27) is symmetric within the pulse and the average frequency is ω_{l} . However, if $\delta\Phi \neq \pm\frac{\pi}{2}$, the average frequency is blue or red shifted, since the pulse sweeps through resonance before or after the maximum amplitude.

In figure 5.4 some FP spectra of amplitude or modulated light are shown.



(a) Pulse shape of AM voltage and light

(b) FP spectrum of AM light



(c) FP spectrum of PM light

(d) FP spectrum of AM and PM light

Figure 5.4 The Fabry Perot spectra of the modulated light pulses. Settings: $V_{SG} = 20$ mV (phase modulator), $-\frac{V_a}{8}$ DC bias of the AM voltage, where V_a is the voltage on the amplitude modulator [13].

The voltage that is applied to the amplitude modulator has about $-\frac{V_a}{8}$ bias, where V_a is the amplitude of the RF voltage (figure 5.4(a)). Therefore the FP spectrum of the amplitude modulated light is small at the center (figure 5.4(b)). The voltage on the phase modulator is $V_{SG} = 20\text{mV}$, which means that $\beta \times V_{SG} = 2.32$. In figure 5.4(c) the FP spectrum of the phase modulated light is shown and finally in 5.4(d) the phase and amplitude modulated spectrum can be seen. The numerically calculated spectra are illustrated in figure 5.5. Comparison of the theoretical prediction and the measurement shows, that for $\delta\Phi = \frac{\pi}{2}$ the calculated spectrum agrees very well with the measured one. This means: The Production of chirped pulses works!

However, the light has to pass through the 4W YDFA and this fiber amplifier induces some asymmetry in the amplitude modulated spectrum. Thus, the combined spectrum for the chirped pulse is not exactly symmetric, even not for $\delta\Phi = \frac{\pi}{2}$. The only way is to adjust the phase delay in a way to get the spectrum as symmetric as possible. The final spectrum of the combination of amplitude and phase modulated light is shown in figure 5.6.

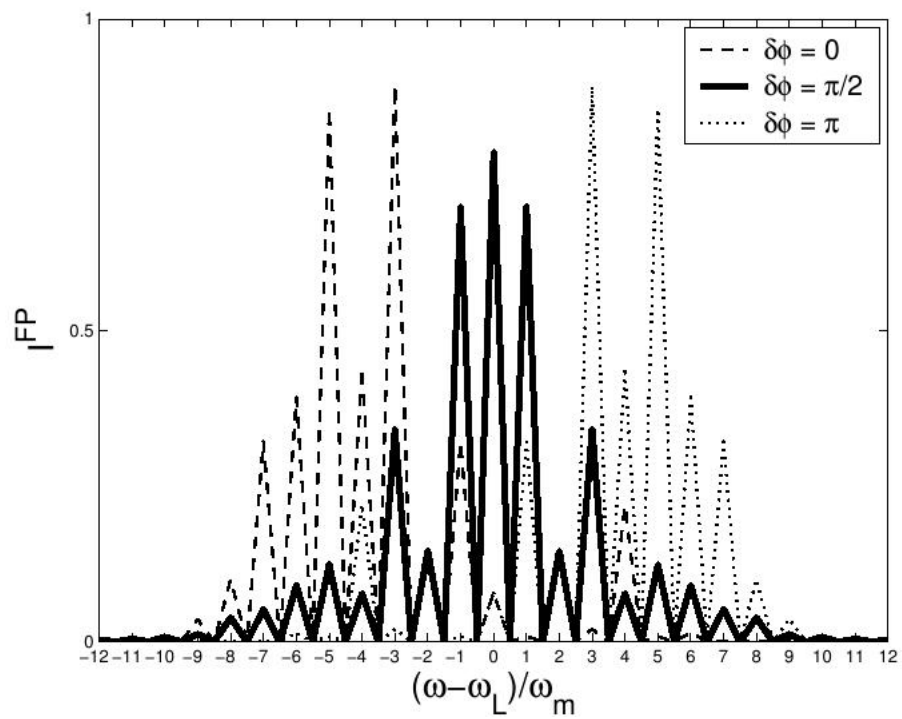
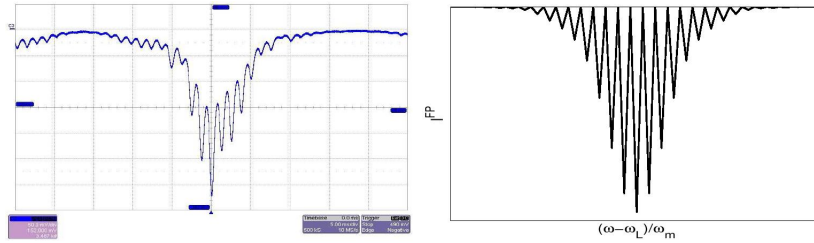
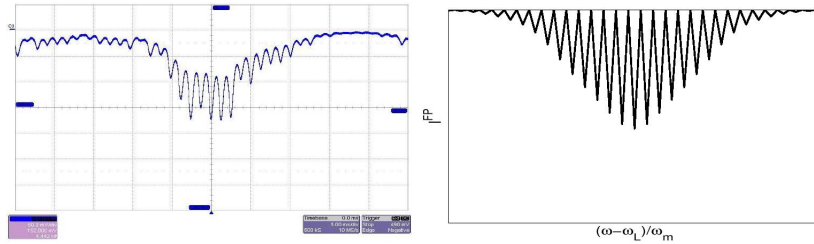


Figure 5.5 Numerical calculation of the FP-spectra of the light pulses in figure 5.4(d) using equation 5.28. The settings are the same as in figure 5.4 [13].



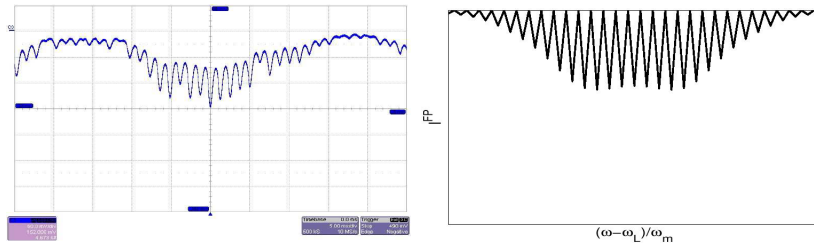
(a) Measured spectrum,
 $V_{SG} = 20 \text{ mV}$

(b) Calculated spectrum,
 $V_{SG} = 20 \text{ mV}$



(c) Measured spectrum,
 $V_{SG} = 36 \text{ mV}$

(d) Calculated spectrum,
 $V_{SG} = 36 \text{ mV}$



(e) Measured spectrum,
 $V_{SG} = 48 \text{ mV}$

(f) Calculated spectrum,
 $V_{SG} = 48 \text{ mV}$

Figure 5.6 Measured (left) and calculated (right) FP spectra of the modulated light after the 4W YDFA. The calculations have been done with equation 5.28. The DC bias voltage on the amplitude modulator is nearly zero [13].

Chapter 6

Measurement of Optical Forces

6.1 Experimental Process

In this experiment optical forces that are associated with adiabatic rapid passage pulses on metastable He-atoms (He^*), which are optically pumped and therefore form a two-level system are examined. This is done, by measuring the deflection of the atomic beam due to the ARP sequences. Assuming that the final transverse velocity is much smaller than the velocity capture range of the optical force (constant acceleration assumption), the final transverse velocity of the atoms is found to be

$$v_t = \frac{F}{m} t_{\text{int}} = \frac{F}{m} \frac{L_{\text{int}}}{v_l}. \quad (6.1)$$

Here, F is the optical force on the He^* atoms, t_{int} is the interaction time, $L_{\text{int}} = 4 \text{ mm}$ the interaction length, $m = 6.646 \cdot 10^{-27} \text{ kg}$ the atomic mass of He^* [38] and v_1 is the longitudinal velocity of the atoms. The relation between the deflection X and the optical force can be written as

$$X = v_t t_{\text{flight}} = \frac{F}{m} \frac{L_{\text{int}}}{v_1} \frac{L_{\text{flight}}}{v_1}, \quad (6.2)$$

where the time for the flight (t_{flight}) is determined by the flight distance ($L_{\text{flight}} = 32.65 \text{ cm}$) to the MCP/PS and the longitudinal velocity v_1 . Therefore the force is given by

$$F_{\text{ARP}} = \frac{mv_1^2 X}{L_{\text{int}} L_{\text{flight}}} \quad (6.3)$$

Under the constant acceleration assumption, F is uniform, so $X \propto \frac{1}{v_1^2}$. Note, that X has a wide spreading because v_1 has a wide distribution. This means, that for a characteristic X that is measured from the images of deflected atoms, a characteristic v_1 must be obtained so that Eq. (6.2) can be used.

As shown in figure 6.1, two characteristic values for X can be utilized. One is the peak value X_p and the other one is the average value X_a . Because of the fact that $X \propto \frac{1}{v_1^2}$ it is obvious that X_p and X_a correspond to the peak and average value of $\frac{1}{v_1^2}$ respectively instead of v_1 . As it is shown in figure 6.1, the peak of the $\frac{1}{v_1^2}$ -distribution is at $v_p = 1080 \frac{\text{m}}{\text{s}}$, while its average value

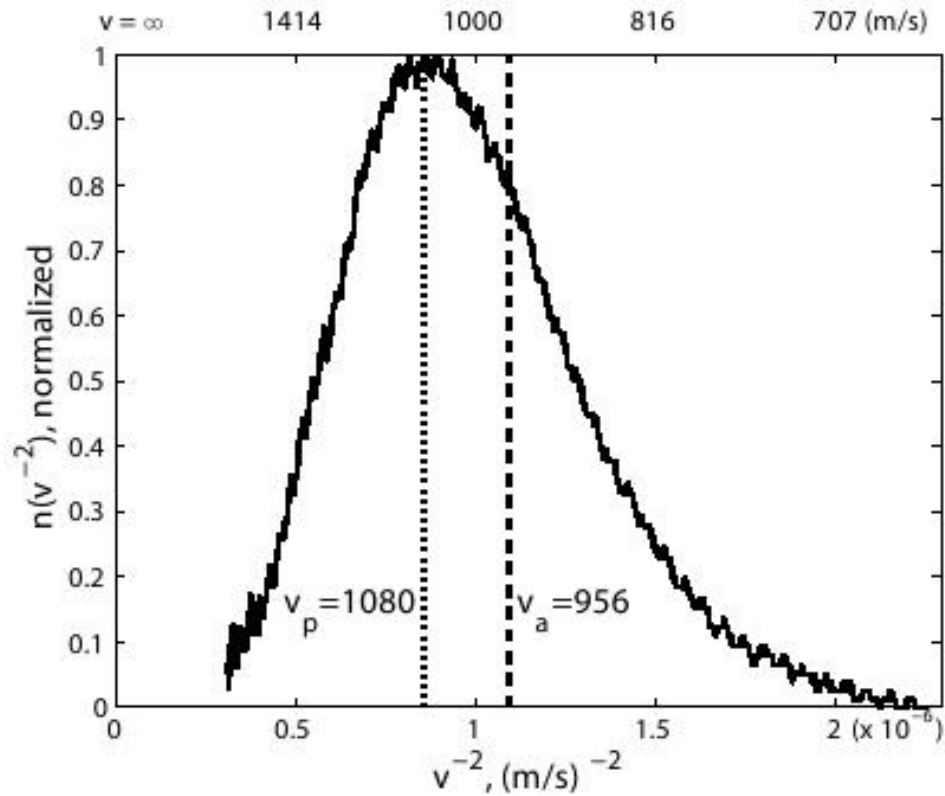


Figure 6.1 The distribution of the inverse square of the longitudinal velocity of the He^* -beam [13]. The distribution is converted from the longitudinal velocity plotted in figure 3.3. For further information see the text.

is at $v_a = 956 \frac{\text{m}}{\text{s}}$ (this is the inverse root of the mean square velocity). It is important to have that in mind when doing the analysis and do not mix up the two different velocities. Since the analysis using v_a is more accurate [13], it will only be referred to this kind of velocity in this thesis (the peak velocity has only be used to get a rough approximation of the force during the experiment). It is worth pointing out that those characteristic velocities are not the peak and average velocity of v_1 with respect to its own distribution,

instead v_p and v_a represent the v_l that correspond to X_p and X_a respectively.

6.2 The ARP Force

The optical forces that are associated with the ARP sequences have been measured with an interaction length of $L_{\text{int}} = 4$ mm, where the size of the laser beam was set by a cylindrical telescope to be $\omega_y = 2.1$ mm in the vertical direction and $\omega_z = 7$ mm in the longitudinal direction. The Gaussian distribution of the light is described by

$$I = I_0 \exp\left(-\frac{2y^2}{\omega_y^2} - \frac{2z^2}{\omega_z^2}\right). \quad (6.4)$$

In order to cut off the wings of this Gaussian beam along the horizontal axis and to set the interaction length, a vertical slit was placed into the beam, with a width of 4 mm.

During the experiment, the chirping frequency was 160 MHz, while the pulsing frequency was set to 80 MHz. The laser was pulsed at ~ 25 % duty cycle. The average power of the laser was $\bar{P} = 0.96$ W and the output voltage of the phase modulator driver was set to $V_{\text{SG}} = 37$ mV. Since the relation between the phase modulation index β and V_{SG} is known to be $\beta = 0.116 \times V_{\text{SG}}$ which results in $\beta = 4.29$ it holds: $\delta_0 = 4.29 \omega_m = 2 \cdot \pi \cdot 686.4$ MHz.

In order to get an expression for the relationship between Rabi-frequency and optical power, the intensity of the laser light has to be looked at. It is known that the relation between the light intensity I_0 and the Rabi frequency Ω is given by

$$\frac{I_0}{I_s} = 2 \left(\frac{\Omega}{\gamma} \right)^2, \quad (6.5)$$

with the saturation intensity $I_s = 0.167 \text{ mW/cm}^2$ and the natural linewidth $\gamma = 2\pi \times 1.62 \text{ MHz}$ for the transition of He^* that was used in the experiment (table 3.1). The average power for periodically pulsed light in one direction is

$$\begin{aligned} \bar{P} &= \frac{1}{T} \int_0^T dt \int dy \int dz I_0(t) \exp\left(-\frac{2y^2}{\omega_y^2} - \frac{2z^2}{\omega_z^2}\right) \\ &= \frac{\pi}{2} \omega_y \omega_z \frac{1}{T} \int_0^T dt I_0(t) \\ &= \pi \omega_y \omega_z I_s \frac{1}{T} \int_0^T dt \left(\frac{\Omega(t)}{\gamma} \right)^2. \end{aligned} \quad (6.6)$$

With the pulse shape function $f(t)$ and under the assumption that $\Omega(t) = \Omega_0 f(t)$, the average power is

$$\bar{P} = \pi \omega_y \omega_z I_s \left(\frac{\Omega_0}{\gamma} \right)^2 \frac{1}{T} \int_0^{T_p} dt f^2(t). \quad (6.7)$$

When there is a sinusoidal pulse shape (Eq. (5.25) and figure 5.3(a)), then

it is found that $f(t) = \sin(\omega_m t)$, and $T_p = \frac{\pi}{\omega_m}$, $T = 4T_p$. With this in mind it yields

$$\frac{1}{T} \int_0^{T_p} dt f^2(t) = \frac{1}{8},$$

and finally

$$\boxed{\bar{P} = \frac{\pi}{8} \omega_y \omega_z I_s \left(\frac{\Omega_0}{\gamma} \right)^2} \quad (6.8)$$

With an average power of $\bar{P} = 0.96$ W in this experiment a Rabi frequency of $\Omega_0 = 316 \gamma = 3.21 \omega_m$ is obtained. Considering $\delta_0 = 4.29 \omega_m$, a predicted nonadiabatic transition probability of ~ 0.025 is gotten from figure 2.3 which corresponds to a predicted force of $16 F_{\text{rad}}$ (figures 2.7 and 2.8).

The MCP/PS detector that is described in chapter 3.1.4 serves for imaging the atoms of the atomic beam. Those images have been caught using a CCD camera that was sitting outside the vacuum system.

In figure 6.2 the image of the slit without any optical forces can be seen. The view is from the phosphor screen towards the slit that defines the atomic beam. The image 6.3(a) shows the same arrangement, but this time with the light field unblocked. The atoms are pushed into one direction because of the periodic ARP-sequences. In figure 6.3(b) the same setting is shown, but with background subtracted from the slit. For the force calculation a narrow region of the image was chosen and the force was averaged over this region. In this

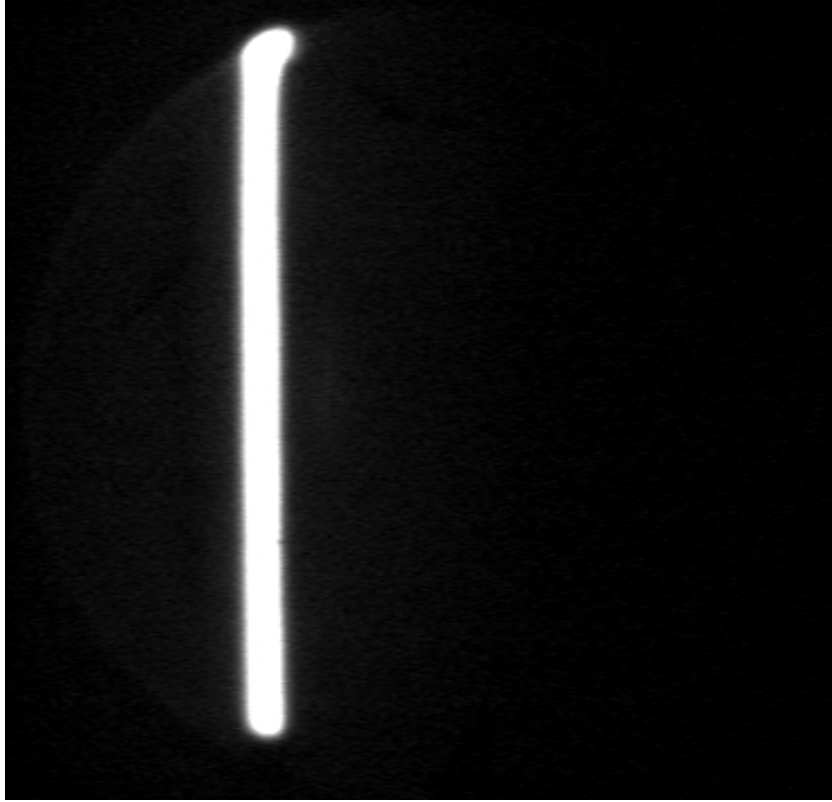
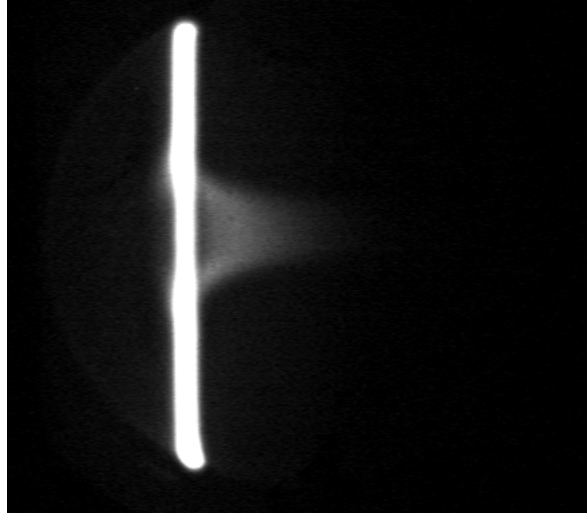


Figure 6.2 Undeflected atomic beam. The view is towards the source and the slit that geometrically defines the atomic beam is imaged on the screen.

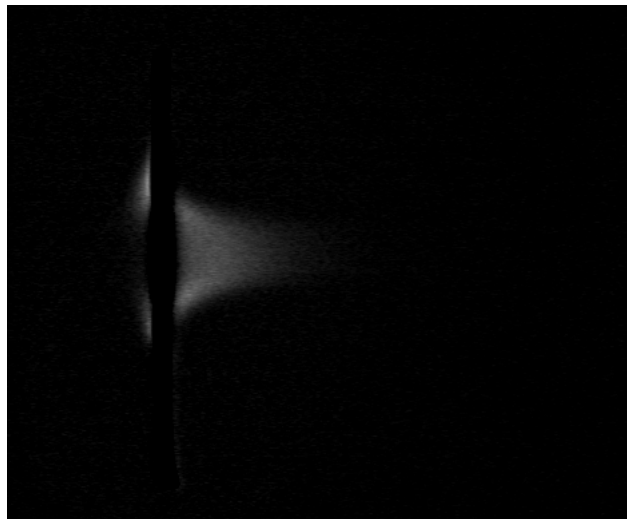
case the force resulting from ARP has a value of

$$\boxed{F_{\text{ARP}} = 6.04 \pm 0.62 F_{\text{rad}}}. \quad (6.9)$$

This is within the error bars the same as the result in [13], which was about $F_{\text{ARP}} = 6.2 F_{\text{rad}}$. This is about 37.5% of the theoretical prediction of $16 F_{\text{rad}}$. The error in the force calculation is due to the error in the measurement of the distances L_{flight} and L_{int} . However, the main reason for the error is the uncer-



(a)



(b)

Figure 6.3 Image of deflected atoms on the phosphor screen (a) with and (b) without background. The undeflected atoms in figure 6.2 are pushed towards the end of the MCP/PS arrangement. The settings were: $V_{SG} = 37$ mV, $\bar{P} = 0.96$ W and an interaction length of 4 mm.

tainty in the calculation of the deflection distance X on the phosphor screen, since the response of the phosphor screen is nonlinear and nonuniform (6.4). Quantitative measurements with the MCP/PS arrangement in this experiment are also very difficult as mentioned in chapter 3.1.4.

Now, the same measurement has been done including the magnetic field, which has a value of about $B \sim (7 \pm 0.5) \times 10^{-4} \text{T}$. The errors mainly result from the uncertainty of the field inside the vacuum system, with the system closed and the pumps running, since it was only possible to measure the field when the pumps were turned off and the system was open. The optical pumping beam was not used any more after a while, because the beam itself does not make such a big difference. Although a small difference was observed, this could also be due to a Doppler push, therefore it was blocked for the later measurements. The reason why the observed effect was mainly due to the magnetic field is because the ARP-light itself is circularly polarized, which causes optical pumping (see section 1.5).

As it is shown in figure 6.5, the force increased with the presence of the magnetic field. Calculations show that now a force with a magnitude of about

$$\boxed{F_{\text{ARP}} = 8.57 \pm 0.70 F_{\text{rad}}} \quad (6.10)$$

is reached. Figure 6.5(c) shows that the deflection on the phosphor screen

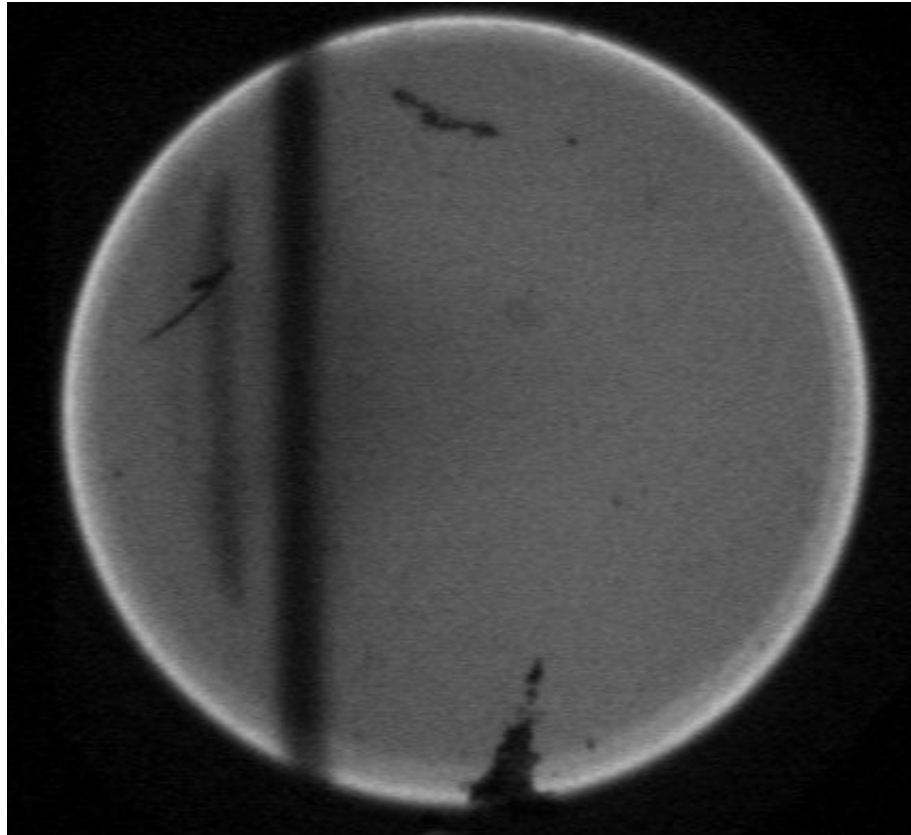
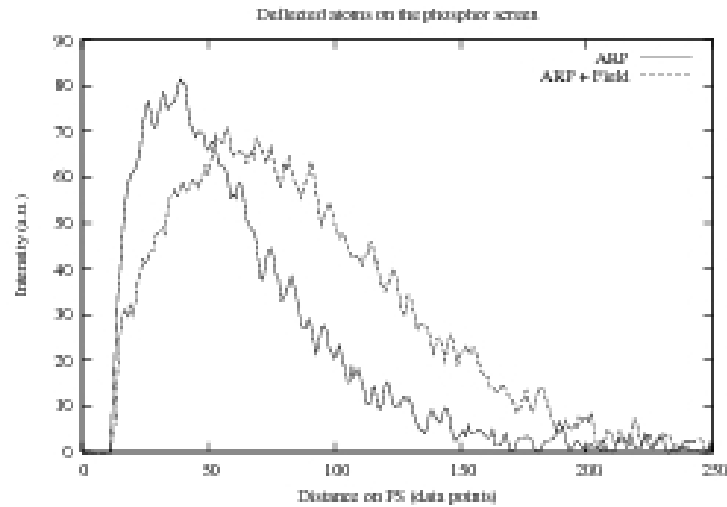


Figure 6.4 The phosphor screen under uniform illumination. The big black stripe is the burnt region from the slit image on the screen, that caused some problems in the lithography experiment and is the reason, why the block was built (chapter 3.1.4). The lighter stripe on the left is the result from some previous measurements and the other black spots (e.g. one at the bottom and one near the top) are damages on the phosphor screen. Since this screen was used many times during the experiment, it has a highly non-uniform shape, which causes some errors for the force-calculation.



(a)

(b)



(c)

Figure 6.5 The deflected atoms on the phosphor screen, but this time including the magnetic field for optical pumping and again (a) with and (b) without background. The settings are the same as in figure 6.3 and the field has a magnitude of approximately $B \sim (7 \pm 0.5) \times 10^{-4}$ T. (c) Image of the deflected atoms on the phosphor screen. The settings are $V_{SG} = 37$ mV, $\bar{P} = 0.96$ W and an interaction length of 4 mm. Each data point on the x-axis represents a deflection of 0.067 mm on the phosphor screen. The solid curve is the ARP-signal without field (from figure 6.3) and the dashed curve is the ARP-signal including magnetic field

increases with applied magnetic field.

This is about 42 % higher than the force without field, but it is still far away from the theoretical prediction. The first suspicion was, that the magnetic field is still too low, but measurements and rough considerations showed that the magnetic field is not the reason for this relatively small force.

6.2.1 Measurements with the laser taken off lock

After doing some measurements with these settings, the settings were changed and the amplitude of the frequency sweep was now $\delta_0 = 5.68\omega_m$ ($V_{SG} = 49\text{mV}$) for a maximum force. The laser power stayed the same during the following measurements. Thus, the resulting force including magnetic field now is

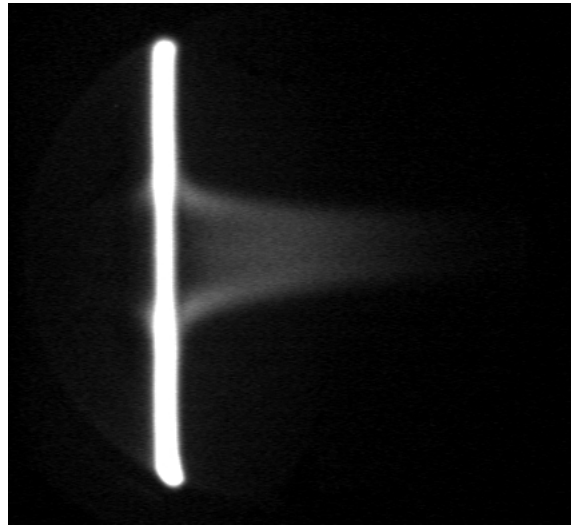
$$\boxed{F_{\text{ARP}} = 9.75 \pm 0.78 F_{\text{rad}}}. \quad (6.11)$$

However, when the laser was detuned from resonance (the magnetic field was still $B \sim (7 \pm 0.5) \times 10^{-4} \text{T}$), a much higher force was observed which was not expected before (figure 6.6).

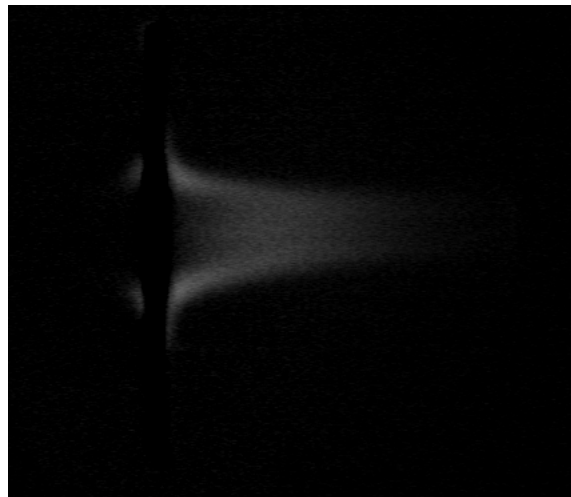
This observation happened accidentally during the run of the experiment and was then subject to a more careful observation. The maximum force that was reached in this way so far is

$$\boxed{F_{\text{ARP}} = 10.8 \pm 0.79 F_{\text{rad}}}, \quad (6.12)$$

which is about 67.5 % of the predicted value and about 10 % more than the force, when the laser was locked (equation 6.11). This was obtained for a blue detuned light field of $\sim 112 \pm 8$ MHz (reading value from the screen of the oscilloscope). Note, that the value for the frequency detuning has such large error bars, since it was not possible to lock the laser off resonance and it was changing its frequency relatively quickly. Apart from that, a bigger force also appeared for a red detuned light field but it was not as strong as when the laser was detuned to the blue side. This kind of measurement has been done several times and it turned out that the result is repeatable. The overall comparison of the traditional ARP-force and the maximum deflection that was gained during the measurements including the magnetic field and the laser taken off lock is shown in 6.7. The first idea was to explain this with the fact that the laser is locked using saturated absorption spectroscopy. Here, the Helium-cell is arranged outside a magnetic field (except for the relatively weak field of the earth), while the atoms that interact with the light field are going through the magnetic field that is caused by the Helmholtz-coils. This results in an energy shift and therefore the laser is not tuned to resonance any more.



(a)



(b)

Figure 6.6 Image of the deflected atoms including magnetic field ($B \sim (7 \pm 0.5) \times 10^{-4}$ T) (a) with and (b) without background. The laser frequency is detuned away from resonance with about 112 ± 8 MHz.

Taking a closer look at this it turned out that this would only explain a shift of ~ 10 MHz, but not such a large shift. Another problem was, that it was not possible to make proper off-resonance measurements, since there was no way to lock the laser off resonance with the equipment that was used in the experiment. One possible explanation for this significantly higher force are multi-photon processes that can be induced when the delay time between the counterpropagating pulses and also the peak amplitudes are chosen in a certain way. The topology of multiphoton adiabatic passage is described in [49]. Maybe this happened accidentally when the laser was taken off lock, but for security and especially for a quantitative description systematic off lock measurements have to be done. Recently, a AOM was bought for the experiment, so systematic off-lock measurements are possible, which will probably give a much clearer picture of the participating effects. This is an important task since right now only a few images exist with many error sources as described above.

One of the assumptions for the theoretical force calculation in this experiment was, that the pulses do not overlap in time (chapter 2). A calculation for temporally coexisting light fields is much more complicated, but maybe has to be done in the future to examine this interesting observation. Apart from that, the spectrum of the light has to be examined in order to describe the

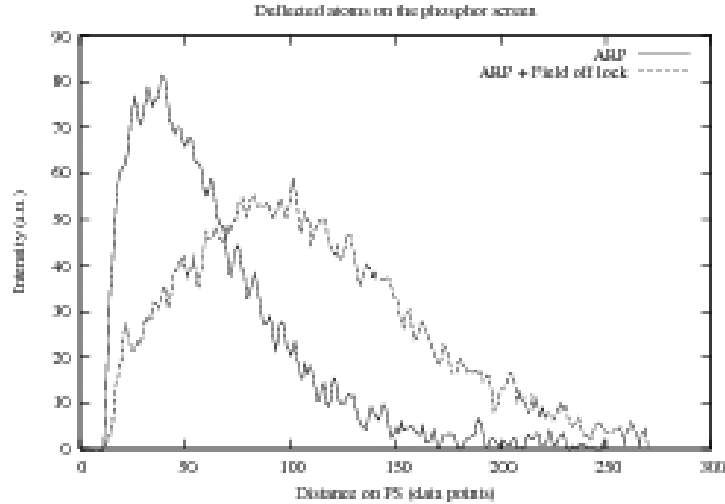


Figure 6.7 Image of the deflected atoms on the phosphor screen. The settings for the solid curve are $V_{SG} = 37$ mV, $\bar{P} = 0.96$ W. It shows the deflection due to the traditional ARP-Force without magnetic field (from figure 6.3). The dashed curve has a phase modulation voltage of $V_{SG} = 49$ mV and shows the maximum deflection of the atoms including magnetic field ($B \sim (7 \pm 0.5) \times 10^{-4}$ T) from figure 6.6 and with the laser taken off lock by about 112 ± 8 MHz. Each data point on the x-axis represents a deflection of 0.067 mm on the phosphor screen.

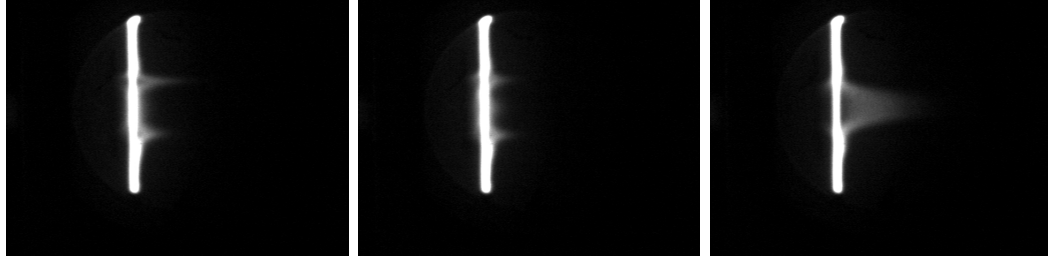
(possible) overlapping of the ARP-pulses.

In figure 6.7 (right edge of the dashed curve) it can also be seen, that some of the atoms are already pushed off the phosphor screen and therefore not all of them are detected. This problem can be easily solved when the interaction length L_{int} is reduced.

6.3 Force Mapping

In order to examine the theory of adiabatic rapid passage it was interesting to look at the force that results from this process for different values of Ω_0 and δ_0 . So the obvious thing to do was a force mapping of the ARP-force including the magnetic field. The goal of this is to systematically study the dependence of F_{ARP} on the chirping amplitude δ_0 and the pulsing amplitude Ω_0 and thus image the force in a two dimensional pulse parameter space. During those measurements, the phase modulator driving voltage V_{SG} varied from 1 mV to 57 mV in steps of 4 mV. The current of the fiber amplifier pumping diode was 4000 mA during the whole measurement. The intensity of the ARP-beam was adjusted, using a $\frac{\lambda}{2}$ -plate with angles from 8° to 52° with a step size of 4° . For each parameter set a picture was taken. For each image, the atom intensity was averaged over the same region for a better comparability and the ARP-Force was calculated. Also the power for each angle of the $\frac{\lambda}{2}$ plate was measured in order to get the corresponding Rabi-frequency with equation 6.8. So 176 pictures have been taken and analysed for this purpose. In figure 6.8 a small fraction of the whole set of pictures is shown.

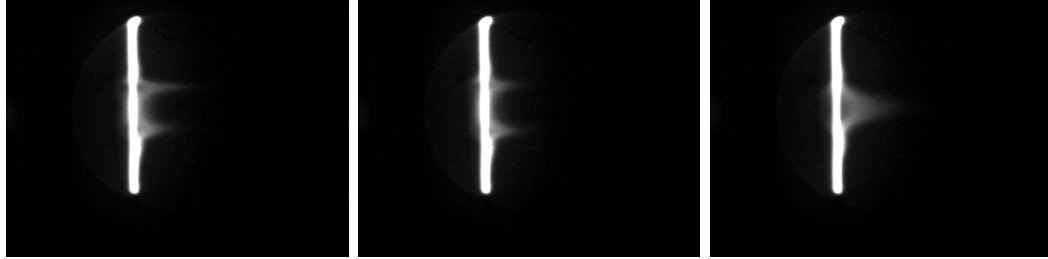
In the first column, the output voltage of the phase modulator driver is very low, so that the laser pulses are hardly chirped (it was not possible to go down to 0 mV with the driver, so the lowest one that could be accomplished



(a) (1 mV, 52°) \rightarrow (0.12, 3.21)

(b) (21 mV, 52°) \rightarrow (2.44, 3.21)

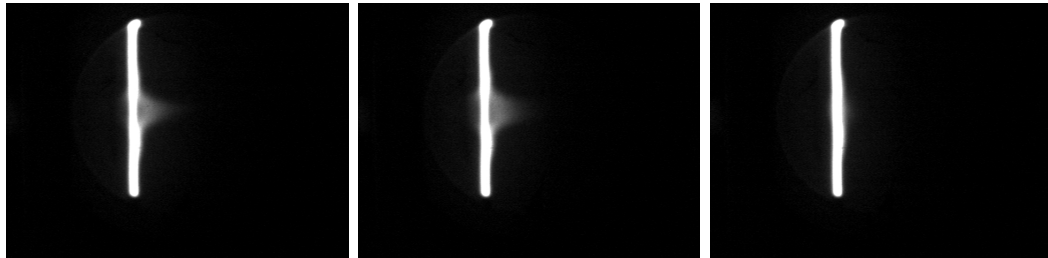
(c) (41 mV, 52°) \rightarrow (4.76, 3.21)



(d) (1 mV, 32°) \rightarrow (0.12, 2.47)

(e) (21 mV, 32°) \rightarrow (2.44, 2.47)

(f) (41 mV, 32°) \rightarrow (4.76, 2.47)



(g) (1 mV, 20°) \rightarrow (0.12, 1.54)

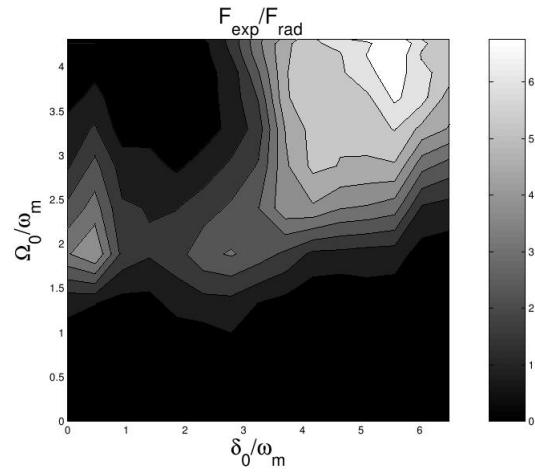
(h) (21 mV, 20°) \rightarrow (2.44, 1.54)

(i) (41 mV, 20°) \rightarrow (4.76, 1.54)

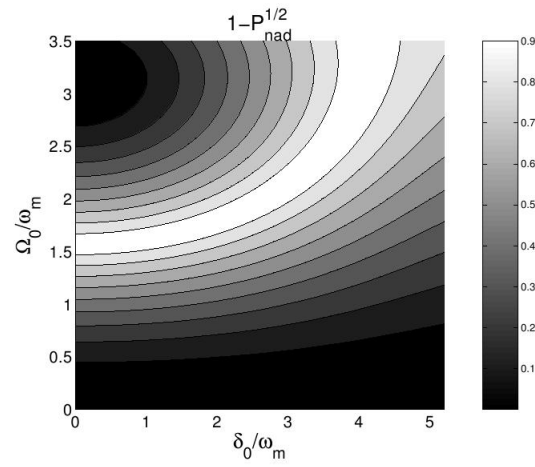
Figure 6.8 A fraction of the images that have been taken for the Force-Mapping. The Parameters are indicated below each image: $(V_{SG}, \theta_{\frac{\lambda}{2}}) \rightarrow (\frac{\delta_0}{\omega_m}, \frac{\Omega_0}{\omega_m})$. Again, the magnetic field has a value of $B \sim (7 \pm 0.5) \times 10^{-4}$ T.

was 1 mV). The two upper pictures in the third column show the huge deflection of the atoms, while for the lowest picture in this column the power (Rabi-frequency) is not high enough to satisfy the π -pulse condition. The column in the middle shows the deflection for parameters in the middle between the extremes. The laser beam has a Gaussian beam profile and so the light intensity (\rightarrow Rabi frequency) decreases from the center to the edges of the image, which should result in a vertically symmetric deflection image. The bottom picture in the first column has a maximum deflection in the center of the image, where also the light intensity has its maximum. This means, that the π -pulse condition is satisfied here for Ω_0 which results in a high force. When Ω_0 is now increased, this condition is not satisfied any more. But it is satisfied somewhere on the wings, since the intensity decreases from the middle of the picture to its edges. This results in two side peaks that are shown in the middle and in the top picture of the first column, while in the top picture the side peaks are even further apart, since Ω_0 is bigger there. The two lowest images in the second column show a similar behavior as the pictures in the first column. However, in the top picture a third peak arises in the middle of the deflection image. This indicates, that Ω_0 satisfies the 3π -pulse condition. This is justified in figures [2.3](#), [2.7](#) and [2.8](#).

In the third column it can be seen, that the ARP-force does not vary very



(a) Force map experiment



(b) Contour of $1 - \sqrt{P_{\text{nad}}}$ (theory)

Figure 6.9 (a) The Force resulting from ARP-sequences measured in [13] and (b) the contours of $1 - \sqrt{P_{\text{nad}}}$ both in the space of $(\delta_0/\omega_m, \Omega_0/\omega_m)$. Note, that the two plots are scaled differently.

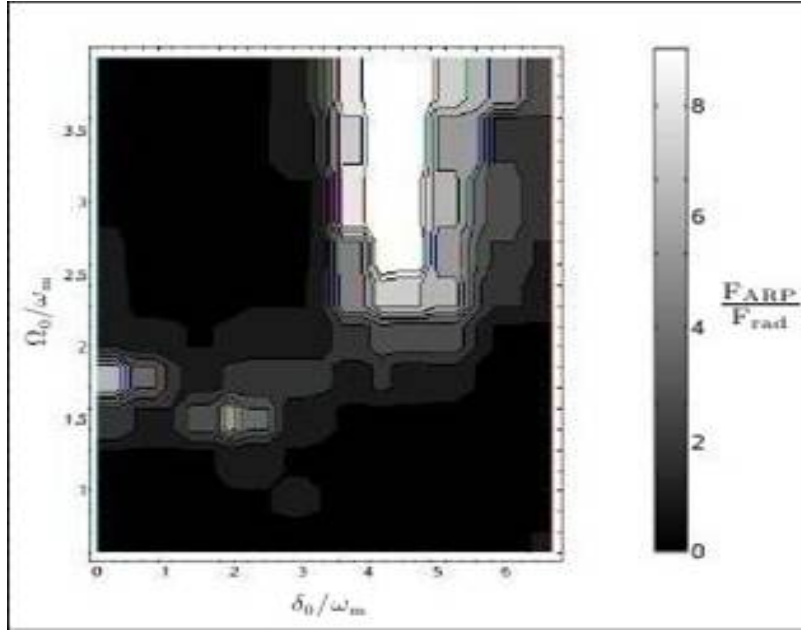


Figure 6.10 The same measurement as in figure 6.9 (a), but this time including the magnetic field. The result is much clearer than in figure 6.9(a).

much, once the intensity is above a certain threshold, which again indicates the expected robustness of the force.

In order to analyse the data, a C++ Code was written. For each set of parameters, the optical force was calculated, that results in a two-dimensional force map, which is shown in figure 6.10. The map without magnetic field [13] can be seen in figure 6.9 as well as the contours of $1 - \sqrt{P_{\text{nad}}}$, that is the non-adiabatic transition probability for a single sinusoidally chirped sinusoidal pulse (the ARP-Force is also proportional to $1 - \sqrt{P_{\text{nad}}}$, see equation 2.17). It is obvious, that the result with magnetic field matches much better with the

predicted distribution as the one with just the ARP-force. This is no surprise since the goal was to produce a proper two-level atom and the numerical calculations have also been made for a two-level system.

6.4 Conclusion

The force that results from Adiabatic Rapid Passage sequences could be improved from $F_{\text{ARP}} = 6.2 F_{\text{rad}}$ in [13] to a maximum of $F_{\text{ARP}} = 10.8 F_{\text{rad}}$, which is an about 74% higher value than before. Apart from that, the results of the force mapping in [13] were improved and the qualitative agreement with the theoretical prediction is now a lot clearer than before, which is another proof of the robustness of the force and also of the correctness of the theory. This means that including the magnetic field for optical pumping was a success because with the two-level atom, that is produced in this way, a significant improvement is gained. However, the force is still smaller than the predicted force of $F_{\text{theo}} = 16 F_{\text{rad}}$. There are several reasons for that: First of all, this may be due to errors in power measurement and to systematic errors from the nonlinear and nonuniform response of the phosphor screen. Probably the most important reason for this relatively small force is the non-ideal pulse shape (figure 5.4)(a), which was not an ideal sinusoidal shape as in the theoretical derivation. The tails of the laser pulses extended longer than 3.125

ns required for 25% duty cycle pulsing, which results in an overlapping of the counterpropagating light pulses. Apart from that, the 4 W YDFA induced degradation of the chirped pulse as can be seen in figure 5.6. Another question is, why the force gets significantly higher, when the laser is taken off lock. This is possibly due to the temporally overlapping of the counterpropagating ARP-pulses and will be subject to future research. But despite all those error sources, the results of [13] have been confirmed and even improved.

Bibliography

- [1] T. Hänsch and A. Schawlow. Cooling of gases by laser radiation. *Opt. Commun.* 13(1):68-71, (1975).
- [2] D. Wineland and W. Itano. Laser cooling of atoms. *Phys. Rev. A.* 20(4):1521-1540, (1979).
- [3] I. I. Rabi. Space Quantization in a Gyating Magnetic Field. *Phys. Rev.* 51, 652, (1937).
- [4] C. Cohen-Tannoudji, B. Diu and F. Laloë. *Quantum Mechanics.* Wiley and Sons, New York, (1983).
- [5] N. F. Ramsey. *Molecular Beams.* Clarendon Press, Oxford (1956).
- [6] M. O. Scully and M. S. Zubairy. *Quantum Optics.* Cambridge University Press, Cambridge, (1997).
- [7] H. J. Metcalf and P. van der Straten. Laser cooling and Trapping. Springer, New York, (1999).

- [8] Karl Kerényi. *Die Mythologie der Griechen*. dtv, München, (1992).
- [9] R. Feynman, F. Vernon and R. Hellwarth. Geometrical representation of the Schrödinger equation for solving maser problems. *J. Appl. Phys.* 28(1):49-52, (1957).
- [10] G. E. Pake. *Paramagnetic Resonance*. Benjamin, New York (1962).
- [11] H. Haken and H. C. Wolf. Atom- und Quantenphysik. 8. Auflage, Springer, Berlin, (2004).
- [12] C. Cohen-Tannoudji and W. D. Phillips. *Physics Today*. 43:33-40, (1990).
- [13] X. Miao. Optical Forces on Atoms with Periodic Adiabatic Rapid Passage Sequences. PhD thesis, Stony Brook University, (2006).
- [14] R. Grimm, J. Söding and Y. B. Ovchinnikov. Coherent beam splitter for atoms based on a bichromatic standing light-wave. *Opt. Lett.* 19(9):658-660, (1994).
- [15] H. Metcalf. Laser Cooling Without Spontaneous Emission (Proposal). *Stony Brook University*, New York, (2007).
- [16] L. Yatsenko and H. Metcalf. A dressed atom description of the bichromatic force. *Phys. Rev. A.* 70:063402, (2004).

- [17] V. S. Voitsekhovich, M. V. Danileiko, A. M. Negriiko et al. 'general discussions of bichro'. *Zh. Eksp. Teor. Fiz.* 99(2):393-410, (1991). [Sov. Phys. JETP 72, 219-227, (1992)].
- [18] J. Söding, R. Grimm, Y. B. Ovchinnikov, P. Bouyer and C. Salomon. Short distance atomic-beam deceleration with a stimulated light force. *Phys. Rev. Lett.* 78(8):1420-1423, (1997).
- [19] V. S. Voitsekhovich, M. V. Danileiko, A. M. Negriiko, V. I. Romanenko and L. P. Yatsenko. Light pressure an atoms in counterpropagating amplitude modulated waves. *Zh. Tekh. Fiz.* 58(6):1174-1176, (1988). [Sov. Phys. Tech. Phys. 33, 690-691, (1988)].
- [20] A. Abragam. *Principles of Nuclear Magnetism*. Oxford University Press, Oxford, (2002).
- [21] E. B. Treasy. Adiabatic inversion with light pulses. *Phys. Lett. A.* 27:421, (1968).
- [22] M. M. T. Loy. Observation of population inversion by optical adiabatic rapid passage. *Phys. Rev. Lett.* 32:814, (1974).
- [23] I. Nebenzahl and A. Szoke. Deflection of atomic beams by resonance radiation using stimulated emission. *Appl. Phys. Lett.* 25:327-329, (1974).

- [24] T. Lu, X. Miao and H. Metcalf. Bloch theorem on the Bloch sphere. *Phys. Rev. A.* 71:061405, (2005).
- [25] M. L. Harris. *Design and construction of an improved Zeeman slower.* Thesis for a distinction in physics. Trinity College, Duke University, (2003).
- [26] L. P. Yatsenko, S. Guerin and H. R. Jauslin. Topology of adiabatic passage. *Phys. Rev. A.* 65:043407, (2002).
- [27] L. Allen and J. H. Eberly. *Optical Resonance and Two-Level Atoms.*, Dover, New York, (1987).
- [28] E. Riis, G. L. Oppo, S. M. Barnett and M. Wilkinson. *Quantum Dynamics of Simple Systems.* Institute of Physics, (1996).
- [29] A. Shapere and F. Wilczek. *Geometric Phases in Physics.* World Scientific, (1989).
- [30] E. E. Nikitin. *Theory of Elementary Atomic and Molecular Processes in Gases.* Clarendon Press, Oxford, (1974).
- [31] D. Sawicki und J. H. Eberly. Perfect following in the adiabatic limit. *Optics Express.* 4:217, (1999).
- [32] L. Landau. *Phys. Z. Sowjet.* 2:46, (1932).

- [33] J. R. Rubbmark, M. M. Kash, M. G. Littmann and D. Kleppner. Dynamical effects at avoided level crossings: A study of the Landau-Zener effect using Rydberg atoms. *Phys. Rev. A.* 23:3107, (1981).
- [34] Y. N. Demkov and M. Kunike. *Vestn. Leningr. Univ. Fis. Khim.* 16:39, (1969).
- [35] K. A. Suominen and B. M. Garraway. Population transfer in a level-crossing model with two time scales. *Phys. Rev. A.* 45:374, (1992).
- [36] J. Kawanaka, M. Hagiuda, K. Shimizu, F. Shimizu and H. Takuma. Generation of an intense low-velocity metastable-neon atomic beam. *App. Phys. B.* 56(1):21-24, (1993).
- [37] G. Lach and K. Pachucki. Forbidden Transitions in the Helium Atom. *Phys. Rev. A.* 12:2455, (1975).
- [38] M. C. Keller. Optical Manipulation of Helium Atoms with Application to Neutral Atom Lithography. Master's thesis, Stony Brook University, (2006).
- [39] W. Lu, M. D. Hoogerland, D. Milic, K. G. H. Baldwin and S. J. Buckman. A bright metastable atom source at 80 K. *Rev. Sci. Instrum.* 72:2558-61, (2001).

- [40] M. Partlow. *Bichromatic Collimation to Make an Intense Helium Beam*. PhD thesis, Stony Brook University, (2004).
- [41] M. Cashen. *Optical Forces on Atoms in Polychromatic Light Fields*. PhD thesis, Stony Brook University, (2002).
- [42] A. Dalgarno, K. L. Bell and A. E. Kingston. Penning ionization by metastable Helium atoms. *J. Phys. B.* 1:18, (1968).
- [43] C. Avila. *Spectral control of a 1083 nm diode laser*. Master's thesis, Stony Brook University, (1998).
- [44] C. E. Wieman and L. Hollberg. Using diode lasers for atomic physics. *Rev. Sci. Instr.* 62:1-20, (1991).
- [45] M. Prevedelli, P. Cancio, G. Giusfredi, F. S. Pavone and M. Inguscio. Frequency control of dbr diode lasers at 1.08 micrometer and precision spectroscopy of Helium. *Opt. Commun.* 125:231-236, (1996).
- [46] W. Demtröder. *Laser Spectroscopy - Basic Concepts and Instrumentation - 3rd Edition*. Springer Verlag, Berlin, (2003).
- [47] A. Yariv. *Optical Electronics in Modern Communications*. Oxford University Press, New York, (1997).

- [48] G. L. Li and P. K. L. Yu. Optical Intensity modulators for digital and analog application. *J. Lightwave Tech.* 21:2010, (2003).
- [49] S. Guerin, L. P. Yatsenko and H. R. Jauslin. Dynamical resonances and the topology of the multiphoton adiabatic passage. *Physical Review A.* 63:031403(R), (2001).
- [50] P. W. Milonni and J. H. Eberly. *Lasers*. Wiley, New York, (1988).
- [51] D. T. Walton, J. Nees and G. Mourou. Broad-bandwidth pulse amplification to the $10^{-\mu\text{j}}$ level in an ytterbium-doped germanosilicate fiber. *Opt. Lett.* 21:1061, (1996).